Spatially Resolved Equivalence Ratio Measurements Using Tomographic Reconstruction of OH*/CH* Chemiluminescence

Thomas Joseph Giroux III

Thesis submitted to the faculty of the Virginia Polytechnic Institute and State University in partial fulfillment of the requirements for the degree of

Master of Science
In
Mechanical Engineering

Joseph Meadows
Todd Lowe
Wing Ng

July 10th, 2020
Blacksburg, VA

Keywords: Tomography, Chemiluminescence, Thermoacoustic Instability, Camera Calibration

Spatially Resolved Equivalence Ratio Measurements Using Tomographic Reconstruction of OH*/CH* Chemiluminescence

Thomas Joseph Giroux III

ABSTRACT

Thermoacoustic instabilities in gas turbine operation arise due to unsteady fluctuations in heat release coupled with acoustic oscillations, often caused by varying equivalence ratio perturbations within the flame field. These instabilities can cause irreparable damage to critical turbine components, requiring an understanding of the spatial/temporal variations in equivalence ratio values to predict flame response. The technique of computed tomography for flame chemiluminescence emissions allows for 3D spatially resolved flame measurements to be acquired using a series of integral projections (camera images). High resolution tomography reconstructions require a selection of projection angles around the flame, while captured chemiluminescence of radical species intensity fields can be used to determine local fuel-air ratios.

In this work, a tomographic reconstruction algorithm program was developed and utilized to reconstruct the intensity fields of CH* and OH*, and these reconstructions were used to quantify local equivalence ratios in an acoustically forced flame. A known phantom function was used to verify and validate the tomography algorithm, while convergence was determined by subsequent monitoring of selected iterative criteria. A documented method of camera calibration was also reproduced and presented here, with suggestions provided for future calibration improvement. Results are shown to highlight fluctuating equivalence ratio trends while illustrating the effectiveness of the developed tomography technique, providing a firm foundation for future study regarding heat release phenomena.

Spatially Resolved Equivalence Ratio Measurements Using Tomographic Reconstruction of OH*/CH* Chemiluminescence

Thomas Joseph Giroux III

GENERAL AUDIENCE ABSTRACT

Acoustic sound amplification occurs in the combustion chamber of a gas turbine due to the machine ramping up in operation. These loud sound oscillations continue to grow larger and can damage the turbine machinery and even threaten the safety of the operator. Because of this, many researchers have attempted to understand and predict this behavior in hopes of ending them altogether. One method of studying these sound amplifications is looking at behaviors in the turbine combustion flame so as to potentially shed light on how these large disturbances form and accumulate. Both heat release rate (the steady release of energy in the form of heat from a combustion flame) and equivalence ratio (the mass ratio of fuel to air burned in a combustion process) have proven viable in illustrating oscillatory flame behavior, and can be visualized using chemiluminescence imaging paired with computed tomography.

Chemiluminescence imaging is used to obtain intensity fields of species from high resolution camera imaging, while computed tomography techniques are capable of reconstructing these images into a three-dimensional volume to represent and visualize the combustion flame. These techniques have been shown to function effectively in previous literature and were further implemented in this work. A known calibration technique from previous work was carried out along with reconstructing a defined phantom function to show the functionality of the developed tomography algorithm. Results illustrate the effectiveness of the tomographic reconstruction technique and highlight the amplified acoustic behavior of a combustion flame in a high noise environment.

Acknowledgements

This work would not have been possible without the help and encouragement of a select group of people who I wish to acknowledge for their contributions to my success. First, I would like to thank my family for their undying commitment and support throughout this process; I owe my successes, my triumphs, and my life to them, and for this I am forever grateful.

To my fellow lab mates who helped me through solving problems in both research and classes, especially Mr. Cody Dowd for his aid in collecting and analyzing data, I am most indebted. I also would like to thank the staff of the Advanced Propulsion and Power Lab, specifically Mr. Randall Monk, for his time and contributions in helping provide the necessary lab equipment modifications for this study.

My efforts in graduate school would not have been possible without the funding from the New Horizon Graduate Scholars Program, and I especially would like to thank Mrs. Renee Cloyd, who's positive energy always put a smile on my face. To my committee advisors Dr. Todd Lowe and Dr. Wing Ng, for their support both inside and outside the classroom and for their feedback to make this work the best that it could be. And finally, I would like to thank my research advisor Dr. Joseph Meadows, for his continuous support and for challenging me and pushing me farther than I ever thought I could go.

Dedication

To my parents, thank you for everything.

Table of contents

List of Figures

List of Tables

Chapter 1: Introduction

The presence of thermoacoustic instabilities in combustion engines has been a major issue of importance for much of the past century [1]. In gas turbine engines, these instabilities consist of successive flow perturbation from pressure oscillations coupled with increased flame heat release, proving capable of significant acoustic growth within the combustion system. These fluctuations of pressure exponentially increase until saturation at which point they reach a limit cycle due to non-linearities within the system. The oscillations have devastating effects, particularly on overall engine performance and efficiency, and have prompted numerous investigations into developing methods for studying and monitoring thermo-acoustic stability [2-4]. This work aims to develop a methodology for measuring phase-averaged, spatially resolved equivalence ratios using a developed 3D tomography technique with application to thermoacoustic investigations. Correlations between equivalence ratio and pressure fluctuations originating from the forced acoustic excitation are explored to demonstrate the effectiveness of this method for investigating thermo-acoustic oscillatory behavior. Further discussion is provided in following chapters regarding development and utilization of the data reconstruction method used in this work.

1.1 Thermoacoustic Instabilities Overview

The study of vibrational effects due to turbulent flame interactions can be traced back to the work of Lord Rayleigh [5]. He noticed that upon introducing an open Bunsen burner flame to the end of a long vertical tube, an oscillatory resonance was produced. This was due to the continued unsteady heat release of the flame, causing a periodic pressure fluctuation along the air column at a sustained natural frequency. When the pressure oscillation amplitude matched in

phase with that of the heat release oscillation amplitude, a combustion instability was produced. This would later be outlined as the Rayleigh Criterion, which states that a thermoacoustic combustion instability will occur if the energy added to the system due to the in phase relationship of heat-release and acoustic pressure fluctuations is greater than the energy due to acoustic dissipation [6]. The initial study conducted by Rayleigh primarily focused on the system resonant frequency and tube length, rather than the characteristics of the flame. In his work, Rayleigh determined there to be a time lag between heat release of the flame and the acoustic pressure observed, leading to the conclusion that the greatest chance for this phenomena to occur is at the moment of greatest compression located upstream of the flame front [3].

Traditionally, unstable thermo-acoustic phenomena occur in reacting fluid flow involving a combustion flame and can cause pressure fluctuations resulting in undesirable flame perturbations. These perturbations grow increasingly in size with time and pose significant operational and safety risk for mechanical systems, particularly in the use of gas turbines. Today, modern gas turbines are given strict design parameters to operate under lean-premixed combustion conditions, set on reaching high turbine inlet temperatures while releasing the least amount of nitric oxide emissions. These conditions can allow for significant sound amplification, resulting in amplified resonant frequencies that generate thermoacoustic instabilities. Significant damage to turbine components and machinery can occur, along with flame blow off which can prove detrimental for operational costs and even life-threatening for pilots operating turbine-powered aircraft [7]. Such risk has prompted extensive research into the causes and behavior of thermoacoustic instabilities in turbine engines and has inspired research to seek methods of decreasing oscillation occurrences and to one day eliminate them all together. The research of instantaneous heat release rate and equivalence ratio within pressure oscillations in particular has

seen a number of studies conducted showing effective use of spatially integrated chemiluminescence measurements [8-13]. Fuel-air ratio oscillations are driven by pressure and velocity fluctuations in lean premixed combustors, while spatio-temporal fluctuations in equivalence ratio directly perturb heat release via fluctuations in reactant density, flame speed, heat of reaction, and flame surface area [14]. Due to this direct correlation, chemiluminescence studies can investigate heat release rate using the collection of time-resolved velocity measurements simultaneous to chemiluminescence intensity measurement [15]. The spatial and temporal nature of fuel-air mixture ratios allows for detection and capture of intensities for chemiluminescence and was implemented in this study using tomographic reconstruction for equivalence ratio measurements, with the goal of utilizing temporal velocity measurements to detect heat release in future studies. This integrated technique provides ample means to resolve 3D spatial intensity data for varying excited species, and has historically proven effective coupled with chemiluminescence imaging analysis as highlighted in previous studies [9, 16-18].

1.2 Tomographic Reconstruction Overview

The method of tomographic reconstruction is an attempt to reconstruct an estimated representation of a system based off of an input finite number of projections. With the primary mathematical foundation being set by the work of Johann Radon in 1917, the technique has been outfitted for use in a number of different fields. Most notably in the field of medicine, X-Ray Computed Tomography (CT) has been developed as a non-invasive method of imaging the human body. While there are a number of methods used as derivations of reconstructed tomography, the general concept of developing three-dimensional object reconstructions from provided projections remains constant throughout all reconstruction algorithms. These algorithms are primarily developed from the work and knowledge provided by Radon, as well as

the geometric data of the object and statistical information of the data acquisition. This work will primarily focus on the development of a Multiplicative Algebraic Reconstruction Algorithm for use when reconstructing an acoustically forced flame.

The Algebraic Reconstructive Technique (ART) spawned from the work of Polish mathematician Stefan Kaczmarz, who introduced the Kaczmarz method. This algorithm effectively introduced a method of iteratively solving systems of linear equations of the form $A\,x = b$. Many years later, this work was later built upon by Richard Gordon and colleagues [19] as Gordon developed a reconstruction algorithm that harnessed the mathematical prowess of the Kaczmarz method to produce computed tomographic reconstructions. The technique maintains the same linear format as the Kaczmarz method: A is a sparse $m\ x\ n$ matrix containing the relative contribution of each pixel to the different points on the projections; x is the output image represented in pixels, and b represents the angular projections all in vector notation. The Algebraic Reconstruction Technique is iterative, allowing for images at a series of angular projections to be reconstructed. Additionally, it can be configured so as to include a relaxation parameter of range $0 < \beta \leq 1$ for use to change the speed and stability of convergence for the equation system. This relaxation factor effectively is able to improve the amount of noise present in the output, however at the cost of increased computation time.

1.3 Chemiluminescence Imaging Overview

Validated methods of chemiluminescence imaging have previously been utilized for heat release determination as well as equivalence ratio consideration [8, 20]. When excited radical chemical species are present, they emit photons within a narrow wavelength band. These photons can be measured using advanced imaging equipment and narrow band optical filters through a process known as chemiluminescence imaging. Spatially integrated chemiluminescence

measurements, specifically the ratio of OH*/CH* fields [12], can be comparatively analyzed to examine local equivalence ratio in combustion flames. In this work, a phase-averaged image reconstruction for both CH* and OH* radical species is conducted utilizing Computed Tomography of Chemiluminescence (CTC), and the ratios of OH*/CH* are used to determine phase-averaged, spatially varying equivalence ratios.

Chapter 2: Literature Review

Thermally induced acoustic phenomena have presented widespread challenges for gas turbine operators ever since the machinery's inception. The rapid succession of growing pressure oscillations within the combustion chamber can prove detrimental to turbine operation efficiency as well as overall emission levels and integrity of machine components [1, 4]. In order to further investigate this reoccurring phenomenon, researchers have developed methods of camera projection-based visualization to analyze spatial properties of the combustion flame [9, 17, 18]. The use of computer-aided tomography and chemiluminescence imaging have seen prior use and development in the reconstruction and imaging of turbulent combustion flames for capturing and studying flame behaviors [16, 21, 22]. The technique allows for visualization of flame activity within the combustion zone, and can relate radical species intensity field ratios to spatial equivalence ratio behavior [12]. Recent studies have looked into calculating thermoacoustic energy transfer fields of the Rayleigh Index using chemiluminescence tomography [16, 22], with others focusing on the ability to acquire equivalence ratios from intensity measurements in technically premixed systems [12]. The application of tomographic reconstruction can be traced to its mathematical inception in the developments of Gordon, Bender, and Herman [19] who first published on the method of multi-purpose 3D reconstruction.

2.1 Algebraic Reconstruction Technique

In 1970, Richard Gordon and colleagues proposed a mathematical technique to directly reconstruct three-dimensional objects using two dimensional projections of the objects. The goal and target audience of the paper was focused on the biological field with emphasis on cell and micro-organism structure analysis. Previous work by DeRosier & Klug [23] provided

early attempts at electron micrograph reconstruction, though this method proved unreliable for non-symmetric bodies. Gordon et al. proposed the so-called Algebraic Reconstruction Technique (ART), which was revolutionary in allowing reconstruction of asymmetric objects and requiring significantly less computation time than its predecessors at the time. The technique consists of a stage upon which the object is rotated, a theoretical voxel square encompassing the object, with projections (views of the object) taken at discrete angle θ locations around the object. Each plane perpendicular to the axis projects a line defined as ray, with some of that ray intersecting with the object. The optical density at each voxel point within the square determines the contribution of each pixel, and the number of rays and number of projections dictate the system of algebraic linear equations to acquire the solution. This technique was instrumental in introducing the method of inversion of a discrete number of integral measurements at different angles through the object field, or in other words, the reconstruction of an object from its 2D projections. This opened the door for numerous scientists to build upon the method and adapt the reconstruction technique to prove nimbler and less computationally costly. Such techniques as the Multiplicative Algebraic Reconstruction Technique (MART) have improved upon the foundational building blocks of ART and have been altered for more streamlined computation. Adapted versions of different algorithms have been presented by Verhoeven and compared with chosen simulated conditions of typical tomography application environments [24]. In his studies, Verhoeven found that the Multiplicative Algebraic Reconstruction Technique resulted in the best output out of all the tested algorithms, noting particular strength when dealing with smooth objects or particularly noisy data. He also states that among the algorithms tested, MART was the significantly preferred technique for objects with steep gradients, and its robust nature allowed it to practically reconstruct data from almost any geometry. Verhoeven concluded that of

the algorithms tested MART created the best visual reconstructions while minimizing error, and had the fastest run time with significantly less computational load [24].

MART has seen continued significant modification and improvement in recent decades, with particular emphasis on iteration entropy and noise reduction [25]. As given from its name, the technique utilizes multiplication to apply the corrective iteration instead of the common additive property, and has been found to return the maximum entropy solution as opposed to the normal entropy solution found with the additive technique [24] (entropy in this context is in reference to information theory, not the common use in thermodynamics). Because of its multiplicative nature, MART is found to be rather adaptable in scope. Work by Mishra et al. has shown adaptability in MART for use with interferometric projections [26], while others have developed methods involving different basis functions. Several studies have included specializations in efforts to better improve reconstruction results, such as the Karhunen-Loeve Basis (TRKB) [27], blobs [28], and cubic splines [29], all of which act as basis functions for the reconstruction algorithm. Not all basis functions are best suited for chemiluminescence measurements, however, as CTC geometries often result in steep gradients in various configurations. For this work, the MART algorithm was used for the tomographic reconstruction of the flame images, utilizing the most common pixel/voxel basis for reconstruction due to its ease of use and broad applicability to multiple measurement approaches.

Other algorithms have indeed been developed with varying advantages and drawbacks compared to ART depending on the situation. The Simultaneous Iterative Reconstruction Technique (SIRT) is commonly used as an alternative to overcome issues that arise with ART, specifically problems with inversion. This technique approximates the solution using a simultaneous least squares estimation and is used to cut down drastically the computational

requirements for large data sets inherent for extremely precise instruments such as a megapixel camera. Many online open-source toolboxes allow streamlined computations using SIRT, the most popular being the ASTRA tomography toolbox developed at the University of Antwerp [30]; the ASTRA toolbox however was not chosen for this work due to its structured design around electron tomography for use in biological imaging applications, and was found rather difficult to adapt for chemiluminescence imaging.

2.2 Camera Calibration

An important measure of collecting imaging data involves calibrating digital and imaging systems for accurate use and output. In this work, the discussion of camera calibration refers to the relation of datum coordinate systems from the camera sensor to the three-dimensional world environment and involves the orientation and translation of coordinates between multiple coordinate systems. Today, there are a number of calibration techniques for imaging systems ranging from off the shelf consumer cameras to high speed advanced cameras. In 1987, Roger Tsai introduced a new method for calibrating cameras for machine vision metrology [31]. In his work, Tsai discusses a two-step technique that focuses on obtaining lens and camera location parameters, as well as camera orientation and radial lens distortion. The method proved particularly effective and versatile for a multitude of camera types and layouts, and continued advancement of this technique has taken place as other researchers have found Tsai's work to be a solid foundation for all-purpose camera calibration. Zhengyou Zhang [32] proposed a new calibration technique that proved versatile in being able to orient the camera based on two or more varying orientations to calibrate. The method used a planar grid pattern (a checkerboard) similar to most calibration techniques, however the new technique allowed either the camera or calibration model plane to be moved and it would still prove effective. Upon taking images of

the model plane, a closed-form solution was implemented using a non-linear optimization technique based on a maximum-likelihood criterion, with radial distortion later taken into account as well. The method proved most effective for alternative model plane angle calibration and was successful in calibrating when either the camera, planar pattern, or both were moved. The work by Zhang proved insightful and led to further studies developing methods of calibration involving camera movement. Work by Remondino and Fraser [33] aimed to bridge the gap between camera calibration and the implemented computer algorithms for close-range photogrammetry, while also touching on concerns regarding radial distortion still present in calibration of consumer-grade digital cameras. Floyd [17] studied the effects of ray tracing on the effects of depth of field, and conducted an optical analysis to determine a projection geometry that takes these effects into consideration. While results of his study are worth noting, his work on camera calibration was ultimately not applied here due to computational cost and complexity. Work done by Lin Ma and colleagues focused on the use of point spread functions as a way to interpret the optical density analysis of the reconstruction data, and utilized the Monte Carlo method for means of calculating the function [34, 35]. While this work proved insightful as well, the Monte Carlo method was not used for the 3D reconstruction process attempted in this study due to its computational complexity. The work of Wang et al [36], however, proved the most efficient in application for this particular study, as it proposed a robust method of calibration for a similar camera system setup involving 12 cameras that were rotated about the object of interest. A set of calibration images were taken for each position, and a minimum of 6 non-coplanar points were addressed so as to obtain a fully determined system of equations to solve for each unknown parameter. This method proved most effective allowing for the intrinsic camera parameters and the exact spatial locations to be determined through the lens

imaging theory, accounting for out of focus effects while following the pinhole camera model. This method also included common variables and nomenclature to allow for seamless integration with known reconstruction techniques, specifically MART, proving most efficient when reconstructing the images.

2.3 Thermoacoustic Instabilities

Investigations of thermoacoustic instabilities in engines did not take shape until the beginning of World War II with investigations by Lettau [7]. A number of researchers followed suit and began working extensively on sources of acoustic vibrations and oscillatory behavior in aircraft and rocket engines. Most notably in 1956 Crocco and Cheng [1] published a holistic and extensive investigation on combustion instabilities in rocket motors, considered by many to be the first and foremost resource on nonlinear thermoacoustic behavior in rocket motors. Not long afterwards, Mitchell and Sirignano [4] built upon the sensitive time lag model previously proposed by Crocco, going into mathematical and descriptive detail discussing analysis and possible treatment methods for gas dynamic problems that may arise in motor operation. He focused particularly on the employed expansion techniques, discussing shock wave longitudinal oscillation characteristics and later discussing axial mode instabilities with and without the time lag model, respectively. Mugridge [3] focused primarily on the analysis of both the acoustic impedance on both sides of the combustion zone as well as a flame transfer function that models the flame response to sound wave disturbances. The transfer function was modelled using plane wave theory, with Mugridge deriving both the energy flow and flame transfer function equations in considerable depth. Significant attention and emphasis were placed on the flame transfer function, with the value of the function depending on the fuel used, the resulting flame shape, and the method of dynamic stabilization. An increased interest in theories investigating acoustic

oscillations in flow cavities emerged, and further work by Keller [7, 37-39] developed a scientific understanding of forced and self-excited thermoacoustic oscillations within cavities. Forced excitation applies when the pressure oscillation is imposed by some external mechanism independent of the system, while self-excitation involves acoustic radiation and dissipation that becomes proportional to the amplitude and thus oscillates at the resonant frequency of the oscillatory system. Keller was able to develop and demonstrate wave equations that governed nonlinear, resonant acoustic wavefields in rectangular cavities, proving capable of being applied to both self-excited and forced oscillations for practically any arbitrary boundary conditions [38]. He also went on to investigate and develop second order wave equations for covered cavities excited by a wall-bounded jet, finding that upon strong disturbance along the free edge of the jet there was a significant reduction in oscillation amplitudes within the cavity [37].

Up until this point the majority of research conducted had been centered around thermoacoustic oscillations in rocket motors; in 1995, Keller introduced one of the first investigations on thermoacoustic oscillations in gas turbine combustion research [7]. Combustor designs allowed a significant portion of air to enter the turbine through the burners, resulting in surprisingly powerful sound amplification downstream of the combustion zone [7]. This coupled with low-NO_x combustor characteristics resulted in flow instabilities that produced reaction rate fluctuations, causing acoustic oscillations. Keller's work served as an in-depth general overview of forced and self-excited oscillations in gas turbine combustion chambers, focusing on stability and amplitude limitation. Future work would go on to investigate this topic in more detail and depth, introducing numerical models for predicting oscillations [2] and even providing operational range stability charts for turbine performance in the presence of thermoacoustic instabilities [40]. One review written by O'Connor and colleagues [41] delved into the effects of

transverse acoustic instabilities, describing in particular detail the direct and indirect effect of transverse wave motions. Concluding remarks discuss how the boundary conditions of the system have a significant impact on the resulting transverse acoustic modes, and while the transverse modes control the frequency and modal structure of the disturbance field, axial acoustic disturbances in the nozzle often control the flame response. The spatially integrated heat release of the flame is nearly unaffected by direct transverse flow disturbances, however comparatively axial disturbances and axisymmetric hydrodynamic disturbances have quite an effect on the heat release of the flame.

A dynamic feedback loop created by the interaction of heat release and the acoustic characteristics of a combustion system are the driving factors in creating thermo-acoustic instabilities. These interactions are often random and can be difficult to predict, proving challenging for researchers when trying to model instability oscillatory behavior. Considerable efforts have been made towards methods of numerical modeling to predict limit cycle amplitudes and frequencies [42], while the coupling between unsteady heat release rates and equivalence ratio fluctuations has been found to play a key role in driving thermo-acoustic oscillations [43]. Hoeijmakers et al. [44] and Emmert et al. [45] were central in studying the Intrinsic Thermoacoustic (ITA) feedback loop, consisting of an upstream velocity disturbance that induces variations in the heat release rate, generating an upstream acoustic wave traveling and impeding on the acoustic velocity thereby closing the loop. Velocity fluctuations are measured to describe the responsive heat release of the flame [43], with spatial location measurements required to determine the fluctuations present throughout the flame domain. The need for spatially temporal measurements has motivated instability research towards developing methods

of reconstructive tomography to study everything from heat release rate, flame surface density, to even transient phenomena [18].

Looking at the work of Geraedts and colleagues [16], a notable attempt to tomographically reconstruct thermoacoustic instabilities came as an investigation to analyze swirl-stabilized flames using OH* chemiluminescence. The study utilized the Rayleigh Index Criteria to calculate the energy transfer fields and tested an assortment of perfectly premixed methane-air flames, each containing a helical velocity disturbance coupled with a precessing vortex core (PVC). The tomographic method involved phase-averaging the mean chemiluminescence fields of OH* from a single camera location and proved effective in determining regions of interest within the combustor where thermoacoustic oscillations were prone to occur. The angle position of the PVC and the helical disturbance relative to the camera viewing angle were modeled by tracking the chemiluminescence centroid position [16], contrary to the method in this work utilizing multiple camera angles. These reconstructed 3D tomography models allowed researchers to chart changes in the heat release rate over the thermoacoustic cycle, and ultimately showed the total energy transfer increased with the acoustic pressure oscillation amplitude. The technique provided by Geraedts et al. proved most efficient in supplying accurate energy measurements and served as an effective alternative to more expensive laser-based diagnostic methods.

A goal of this work was to prepare methods of collecting equivalence ratio measurements for the eventual use in monitoring instantaneous three-dimensional flame heat release rate. Work done by Hardalupas [12, 13] and Shreekrishna [14] provided foundational groundwork in understanding the need for spatially resolved equivalence ratios for future use in collecting heat release measurements. Combustion instabilities are known to be caused by unsteady heat release

processes in the system coupled with one or more acoustic modes, causing pressure and flow oscillations ultimately resulting in a feedback loop. Given that fuel-air ratio oscillations are driven by pressure and velocity fluctuations in lean premixed combustors especially near the fuel injection, a number of studies have explored the important relationship between equivalence ratio and heat release measurements in chemiluminescence [12, 14, 15, 42, 43, 46]. At a fixed equivalence ratio, the quasi-steady chemiluminescence emission intensity from the flame exhibits a linear dependence on the reactant flow rate [14, 20], confirming the effectiveness of chemiluminescence for unsteady heat release measurements for flames responding to low frequency flow velocity oscillations [14]. With this understanding, further work will seek to build upon equivalence ratio measurements by simultaneously analyzing time-resolved velocity measurements to explore the perturbations in heat release rate.

2.4 Chemiluminescence Imaging

By definition, chemiluminescence is the emission of light as a result of a chemical reaction process taking place. When applied to flame measurement diagnostics, chemiluminescence can be used to isolate particular radical species in the flame reaction zone and in conjunction with computed tomography produce a reconstruction of the flame structure. The intensity of the species-filtered images can be used to measure a number of flame phenomena, for example acquiring equivalence ratio from the ratio of OH*/CH* fields [12], allowing for in depth analysis and study of flame characteristics. The application of computed tomography was first introduced to chemiluminescence emission measurements by Hertz and Faris [47]. Further investigations like the work of Bohm et al. [48] helped develop methods of incorporating CMOS camera imaging with Computed Tomography of Chemiluminescence, allowing for 3D time resolved spatial information measurements and concentrated profiles of

excited state species. This method of chemiluminescence served as an excellent supplement to known laser-based diagnostics and opened the door for further advancement in the field of high-speed camera chemiluminescence imaging. Further chemiluminescence work helped develop studies into collecting local equivalence ratios from various excited species [10-13, 49, 50] as well as collecting heat release rates for premixed flames [12, 46]. Detecting flame flashback [48] and auto-ignition within the combustion zone [51] have also proven substantial points of analysis for chemiluminescence testing, with investigators taking interest in modelling different reaction mechanisms [13, 20, 46, 52] to better understand excited species behavior. While various other line-of-sight measurements exist for computed tomography, such as Schlieren Photography [53], chemiluminescence imaging is considerably more simplistic and efficient as it naturally occurs in the flame, requiring no need for external light sources in the setup. For this reason, the use of Chemiluminescence Imaging coupled with Computed Tomography was decided upon for this study for its relatively simplistic approach and historical accuracy. Future work will build upon the chemiluminescence imaging outlined here and will eventually include simultaneous velocity measurements, with the goal of obtaining quantitative heat release measurements for further analysis and study (discussed further in Conclusions chapter).

Chapter 3: Mathematical Background

3.1 The Radon Transform

While it was Cormack and Hounsfield who introduced the first Computer Assisted Tomography device for medical imaging in 1979, the initial mathematical work that served as the foundation for Computed Tomography was first introduced in 1917 by Johann Radon, an Austrian mathematician who made several lasting contributions in the area of integral geometry. In his work, the Radon Transform is defined as a series of line integrals that pass through a particular function f at different projection angles in two-dimensional space.

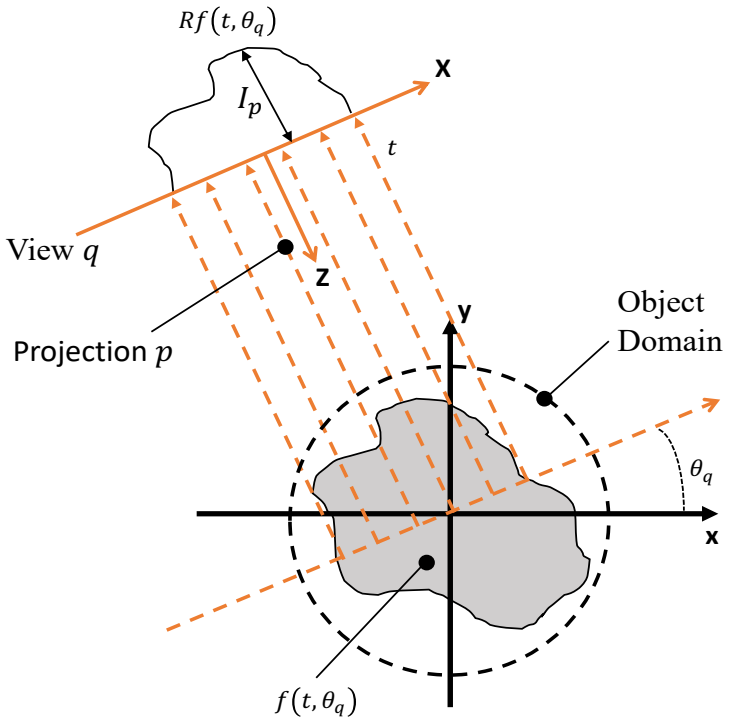

Figure 1. Example Radon Transform for projections based on line integrals.

The Radon Transform is mathematically defined as,

$$Rf(t,\theta) = \int_{-\infty}^{\infty} f\big(x(s), y(s)\big)ds \tag{1}$$

for a function $f(t,\theta)$ for all space on $\mathbb{R}^2$ with $t \in \mathbb{R}$ and $\theta \in (0, 2\pi)$, able to be defined for any straight line within n-dimensional Euclidean Space R^n. In three dimensions, the function f can be defined as an object density, with the Radon Transform representing the 2D projection data, or sinogram, for the object around specified angles. The Radon Transform allows one to determine the total density of a certain function along any specified line l by means of the angle θ and distance t from the origin. A more versatile version of the transform can be rewritten using a delta function in terms of x and y,

$$Rf(t,\theta) = \int_{-\infty}^{\infty} f\big(x(s), y(s)\big)ds = \int_{-\infty}^{\infty}\int_{-\infty}^{\infty} f(x,y)\delta\big(x\,cos\theta_{pq} + y\,sin\theta_{pq} - X_{pq}\big)dxdy \tag{2}$$

with p representing the projection or line integrals, and q representing the angle or view of the object. The Radon transform above is then utilized in finding the inverse Radon Transform of the measured function, the definitive crux of the mathematical backing in computed tomography.

3.2 The Fourier Transform

By using the Fourier Transform Method, the inverse of the Radon Transform can be calculated and ultimately used to reconstruct the original defined density function, serving as a fundamental building block for later developed tomographic reconstruction methods. For any given absolutely integrable function f on Euclidean space $\mathbb{R}$, the Fourier Transform of f in terms of angular frequency ω is defined as

$$\mathcal{F}f(\omega) = \int_{-\infty}^{\infty} f(x)e^{-ix\omega}dx, \tag{3}$$

applying to all infinitely differentiable functions in what is known as the Schwartz Space, denoted as $\mathcal{S}(\mathbb{R}^n)$. The Schwartz Space maintains several beneficial properties for the process of transform inversion, including the existence of a bijective relationship between the Fourier

Transform of a function and its inverse. This relationship allows that for any location in Schwartz Space ($f \in \mathcal{S}$), the Fourier Transform of a Schwartz function remains a Schwartz function and allows one to change the order of integration. It can then be seen that, for an absolutely integrable function f, the inverse Fourier Transform can be defined as,

$$\mathcal{F}^{-1}f(x) = \frac{1}{2\pi}\int_{-\infty}^{\infty} f(\omega)e^{i\omega x}d\omega, \tag{4}$$

Which leads to the determination that for $f \in \mathcal{S}$, the Fourier Inversion Theorem for all x is

$$\mathcal{F}^{-1}(\mathcal{F}f)(x) = f(x). \tag{5}$$

Applying this theorem to two dimensions yields

$$\mathcal{F}_2^{-1}g(x,y) = \frac{1}{4\pi^2}\int_{-\infty}^{\infty}\int_{-\infty}^{\infty} g(X,Y)e^{i(xX+yY)}dxdy, \tag{6}$$

and can be further applied to higher dimensions following the same formulation.

3.3 The Central Slice Theorem

The central slice theorem, also known as the Fourier slice theorem, is able to successfully relate the one-dimensional Fourier transform of the Radon transform with the two-dimensional Fourier transform of a projected function. The theorem definition states that the Radon transform is given by the values along the slice of the two-dimensional Fourier transform of the original image, with the line going through the origin parallel to the line the function was originally projected on. More simply put, a slice of the solved 2D Fourier transform of an object $G(\omega)$ is proven to be equal to the 1D Fourier transform of any infinite number of views at any angle θ within 180^o. As illustrated in Figure 2 [54], the 1D Fourier Transformation of the original object projection, denoted by $p_\theta(v)$, is identical to the sliced cross-section of the 2D Fourier Transformation of the object perpendicular to the direction of the projection, denoted by $F(v_x, v_y)$.

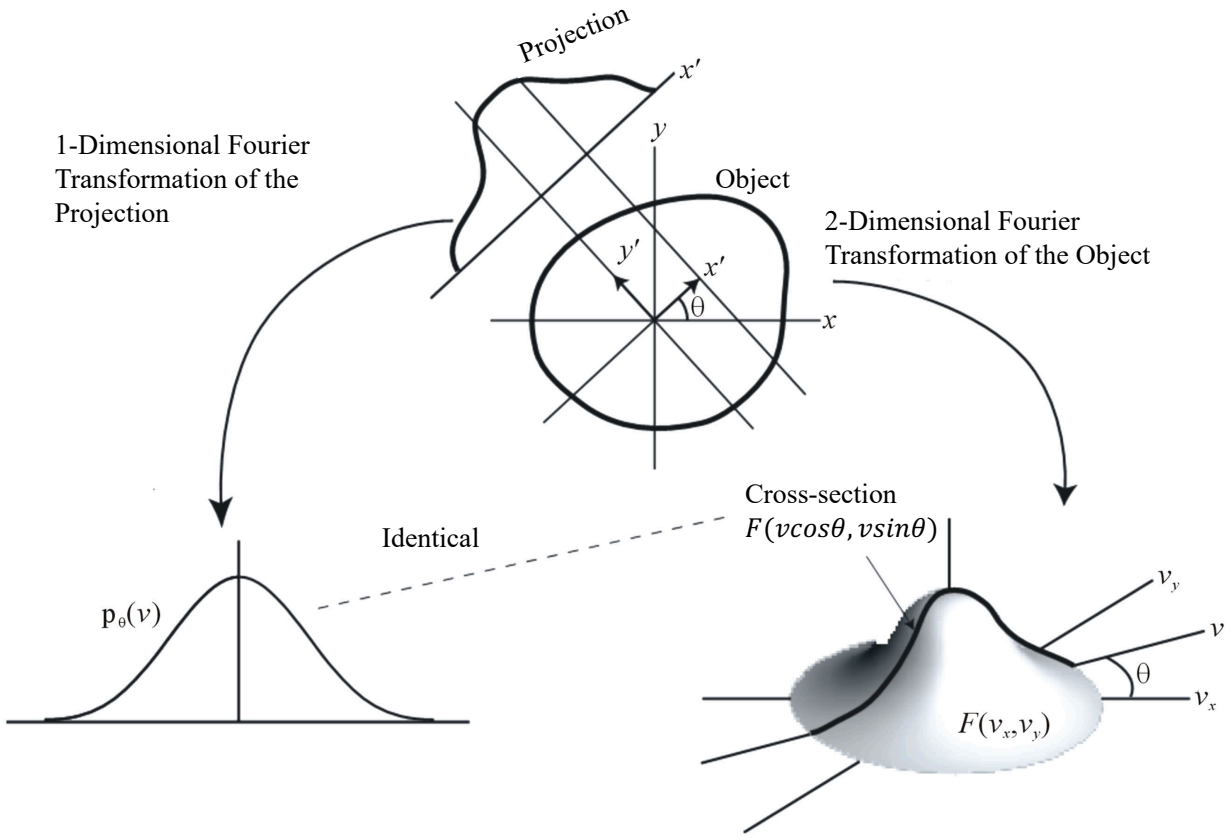

Figure 2. Illustration of the Central Slice Theorem [54].

The central slice theorem serves as a mathematical building block for many fundamental tomographic reonstructive algorithms due to its ability to extract 2D cross-section data from the line integral path of the 1D Fourier transform [55].

3.4 Reconstruction Algorithms

When dealing with projection measurement, there exist two methods of measurement through either emission or absorption. Absorption involves the measurement of an external source with a known location and emission spectra, with the absorption of the emitted source being quantified and measured by a detector. Common examples of this method include electron tomography and laser beam diagnostics, often found employed in medical imaging. Emission

obtains the intensity from an internal source (typically naturally occurring though possible to be artificial as in Positron Emission Tomography) and is often collected via camera imaging techniques and practices. In this work, the use of chemiluminescence as a method of emission will be the major topic of analysis.

Algorithms are classified into two distinct types: analytical and iterative algorithms. Analytical algorithms are typically faster and more computationally lenient, while iterative algorithms maintain a more robust approach to noise presence. Most analytical algorithms are based on the concept of back projection, in which the line integrals of each measured view are successively "smeared" back onto the discrete domain. In essence, the projections are redistributed to their previous locations based on the spatial information of the original object field. By default, this method of back projection has an inherent weakness to noise; to best combat this, the method of back projection is captured in the functionality of the Filtered Back Projection (FBP) Algorithm. During the algorithm's reconstruction process, each view is filtered before every back-projection step, aiding in the overall attenuation and filtering of excessive noise. The FBP algorithm is derived from the previously discussed central slice theorem by taking the inverse Fourier transform previously solved for in equation 6 and converting into polar coordinates and altering the limits of integration.

While analytical algorithms such as the Filtered Back Projection technique are used primarily in medical fields for enhanced, non-invasive imaging, iterative algorithm techniques have seen primary use in the field of physical sciences for their robustness and computational durability. These iterative algorithms are primarily centered around the introduction of a system of linear equations in modelling the reconstruction problem of interest. The system of equations is introduced by forming a discretization of the projection line integral case and dividing the

object domain into a set numbered of voxels. The general case of the projection operator is defined as

$$I_{pq} = \sum_{v=1}^{N_v} w_{vpq} f_v \tag{7}$$

representing the vth voxel, the pth projection, and the qth view, all under the total number of voxels of N_v. In this work, a voxel is defined as a uniform element of three-dimensional space that represents a single entity of an equally divided three-dimensional object volume (it is worth noting, the general terminology for view and projection in this section will eventually be replaced with camera location and pixel, respectively, for ease of understanding in following chapters on methods of algorithm development). The w_{pqv} term represents the contribution of each voxel to the overall object reconstruction, specifically utilizing strip integrals as the intersection area (or volume in 3D) of the strip with voxel v (see Figure 3 below).

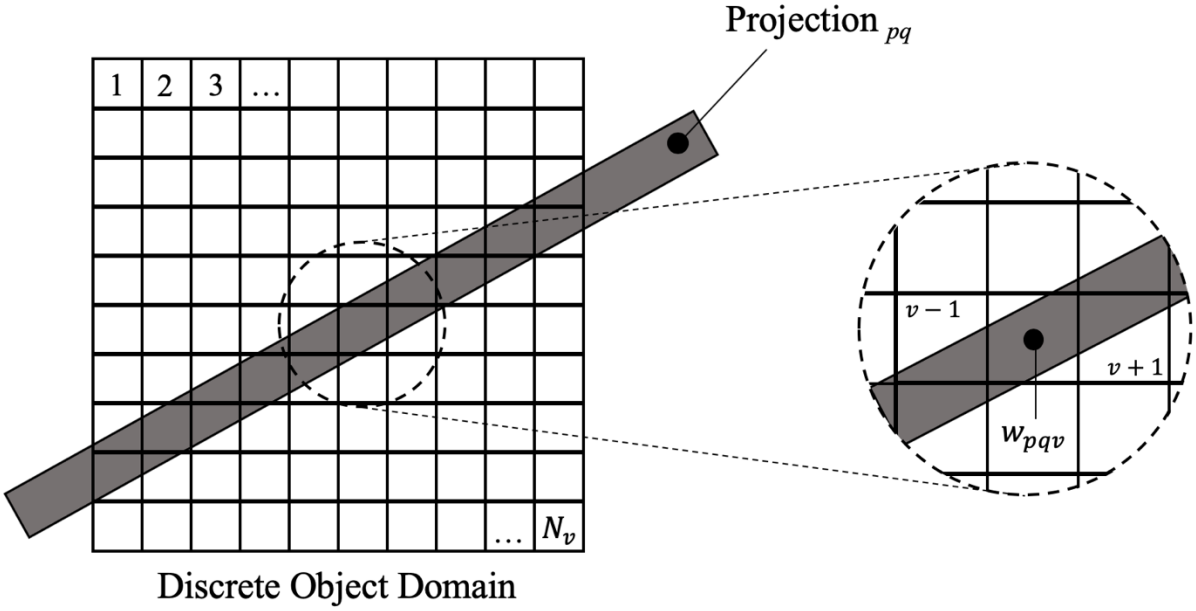

Figure 3. Discrete object domain depicting optical contribution of weight factors across each voxel [17].

This attributes the "weighted" density of the object for each discrete voxel location, allowing for the distributed allocation of the object density to be quantified. With a firm understanding of mathematical rules and manipulation, it can be determined that the system shown in equation 7 can be similarly modelled as a system of linear equations in matrix form,

$$\boldsymbol{I} = W\boldsymbol{f}. \tag{8}$$

The projection matrix W maintains the dimensions of $N_v \times N_p \times N_q$ for all voxels, projections, and views, while $\boldsymbol{f}$ represents the object function valued at each individual voxel. While the variable projection matrix can seemingly grow rather large relatively quickly, it is found that the majority of values inside the matrix are in fact sparse, proving most useful in large computation situations. While the above matrix form implies that the vector $\boldsymbol{f}$ can be determined by the inverse W^{-1}, this is often found to not be feasible as limited number of views and projection noise limit the size of the matrix to be non-square disallowing direct inversion. With limited number of views, the system of equations is found to be under-determined with the number of voxels exceeding the number of projection values. From this, a multitude of iterative algorithms have been introduced and implemented to optimally solve the set system of equations.

The process for almost all of the iterative algorithms is conceptually similar, following a specific process to best converge to the closest possible approximation. Most iterative algorithms start with an initial guess value f^0, which is then passed through the algorithm and a current estimate f^h is compared with the measured projections I to produce an error value associated with that iteration h. The error value is then used to correct the current estimate to the next iteration estimate f^{h+1}, effectively guiding the algorithm to a converged solution until a defined criterion of convergence is reached. Most iterative algorithms differ in their application of this corrective technique, applying corrective measures in various arrangements for varying degrees

of effects. The most common algorithm is the Algebraic Reconstruction Technique (ART); first introduced by Gordon et al. in 1970 [19], the ART paved the way for the development of a family of modified iterative algorithms. The Additive Reconstruction Technique [24] applies the iteration correction through means of adding the step-adjusted value to the current guess value f^h,

$$\boldsymbol{f^{h+1} = f^h + \beta w_{pq} \frac{\left(I_{pq} - w_{pq} \cdot f^h\right)}{w_{pq} \cdot w_{pq}}} \tag{9}$$

While suitable for most applications in reconstruction, a more robust and smoother technique can be found in the Multiplicative Algebraic Reconstruction Technique (MART) which applies its correction multiplicatively. This allows for better reconstructions of objects with higher gradients, providing favorable performance in configurations with a limited number of views. It also allows for any object value that must converge to zero, once the value reaches zero it will remain so due to the multiplicative nature of the algorithm. This, however, requires that the initial guess estimate f^0 cannot be assumed zero, and a mean value must be derived from the projections. The MART algorithm used in this work is taken from the work of Verhoeven [24],

$$\boldsymbol{f^{h+1} = f^h \times \frac{\beta w_{pq}}{w_{pq} \cdot w_{pq}} \left(1 - \frac{I_{pq}}{w_{pq} \cdot f^h}\right)} \tag{10}$$

and incorporates an added relaxation factor $\boldsymbol{\beta}$ to reduce reconstruction noise during iterations. Further discussion on the choice of relaxation parameters and the application of the algorithm can be found in the methods section of this work.

As is the case for any iterative mechanism, a criterion of convergence was needed to encapsulate the iterative scheme and to determine the stopping point of the function. While previous literature has defined various types of convergence [24, 26, 56], most take a similar shape of the difference between criteria from one iteration to the next being less than some

convergence value Δc (in mathematical terms, $X^{h+1} - X^h < \Delta c$). In the work of Mishra et al., criteria takes the form of a maximum absolute difference between consecutive iterations, while Gordon et al. [19, 57] can be seen utilizing the nonuniformity or variance of the measurements, a common and more useful convergence parameter for strictly ART algorithms [24]. In this work, three different errors [26] and one convergence criterion [58] were considered for monitoring iterative performance.

$$E_1 = \max \mid f^{h+1} - f^h \mid \tag{11}$$

$$E_2 = \left[\frac{\sum_N (f^{h+1} - f^h)^2}{N} \right]^{1/2} \tag{12}$$

$$E_3 = \frac{E_2}{\max (f^{h+1}) - \min (f^{h+1})} * 100 \tag{13}$$

A continuation of the convergence criteria presented by Mishra [58] was ultimately chosen for reconstructing the phantom flame images due to its historical accuracy of demonstrating convergence [26, 36, 58].

$$\left| \frac{f^{h+1} - f^h}{f^{h+1}} \right| * 100 \leq c \tag{14}$$

Chapter 4: Theory & Methods

To understand the direction of developing a reconstructive algorithm for computed tomography, a firm understanding of the theory was first required to develop the program. First off, the procedure of reconstructing chemiluminescence fields in the spatial domain requires conversion between different sets of coordinates, and to do so requires a firm grasp on linear algebra as well as in depth calculus and algebra manipulation techniques. The spatial domain of interest where the object for desired reconstruction resides, in this case a combustion flame, is known as the world coordinate system (x_w, y_w, z_w). This space is represented in three dimensions with an origin at the base center of the dump plane. Following this is a three dimension coordinate system with an origin at the center of the camera lens, defined as the lens coordinate system (x, y, z), followed by an image coordinate system centered at the origin of the CCD imaging sensor (x', y').

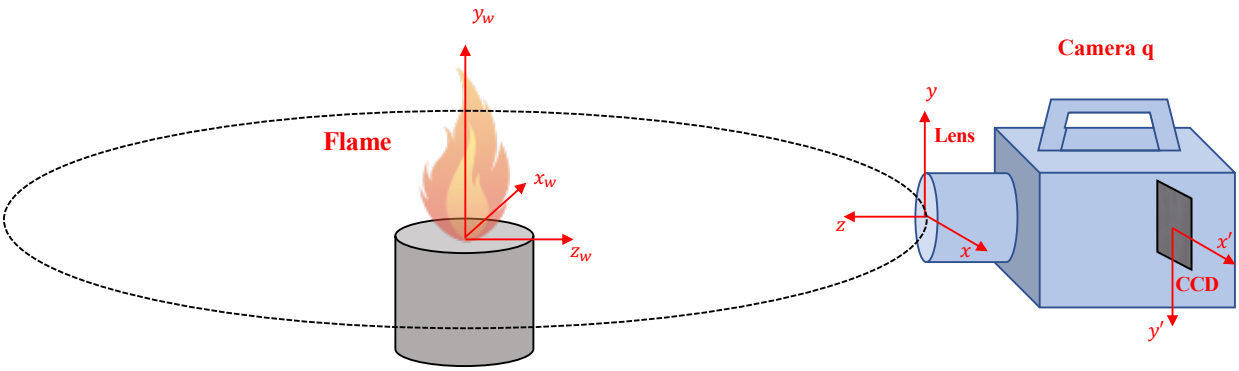

Figure 4. Coordinate domain for world, lens, and image coordinate systems.

The fundamental objective behind Computed Tomography of Chemiluminescence (CTC) is the conversion of an object in world coordinates to an image on the sensor in image coordinates. To accomplish this, the position and orientation of any camera can be uniquely defined by a set of

rotation Euler angles (ψ, θ, ϕ) that determine the "pitch", "yaw", and "roll" of each coordinate vector, and a translation vector containing translations in each of the x, y, and z directions.

$$\begin{bmatrix} x \\ y \\ z \end{bmatrix} = \begin{bmatrix} r_1 & r_2 & r_3 \\ r_4 & r_5 & r_6 \\ r_7 & r_8 & r_9 \end{bmatrix} \begin{bmatrix} x_w \\ y_w \\ z_w \end{bmatrix} + \begin{bmatrix} T_x \\ T_y \\ T_z \end{bmatrix} \tag{15}$$

The Euler angles are defined by Euler's Rotation Theorem, in which any rotation about a certain axis in 3D space can be described by three distinct angles. These angles are then used to determine the rotation coefficients about each axis, and when combined in the order of axis rotation via matrix multiplication (in equation 19, the order of rotation is the z, y, and then x axis) depict the generalized rotation matrix used to rotate any object in 3D space.

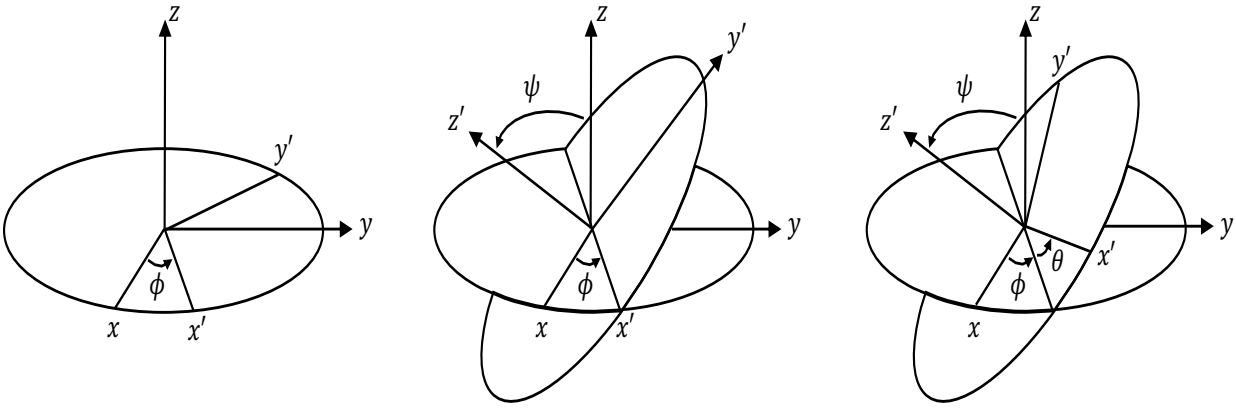

Figure 5. Euler angle rotation around the z, x, and y axes respectively [59].

$$R_x(\psi) = \begin{bmatrix} 1 & 0 & 0 \\ 0 & cos\,\psi & -sin\,\psi \\ 0 & sin\,\psi & cos\,\psi \end{bmatrix} \tag{16}$$

$$R_y(\theta) = \begin{bmatrix} cos\,\theta & 0 & sin\,\theta \\ 0 & 1 & 0 \\ -sin\,\theta & 0 & cos\,\theta \end{bmatrix} \tag{17}$$

$$R_z(\phi) = \begin{bmatrix} cos\,\phi & -sin\,\phi & 0 \\ sin\,\phi & cos\,\phi & 0 \\ 0 & 0 & 1 \end{bmatrix} \tag{18}$$

$$R = R_z * R_y * R_x \tag{19}$$

$$= \begin{bmatrix} cos\ \theta\ cos\ \phi & \sin\psi \sin\theta\ cos\ \phi - \cos\psi \sin\phi & \cos\psi \sin\theta \cos\phi + \sin\psi \sin\phi \\ cos\ \theta\ sin\ \phi & \sin\psi \sin\theta\ sin\ \phi + \cos\psi \cos\phi & \cos\psi \sin\theta \sin\phi - \sin\psi \cos\phi \\ -\sin\theta & sin\ \psi \cos\theta & cos\ \psi \cos\theta \end{bmatrix} \tag{20}$$

$$= \begin{bmatrix} r_1 & r_2 & r_3 \\ r_4 & r_5 & r_6 \\ r_7 & r_8 & r_9 \end{bmatrix} \tag{21}$$

After acquiring lens coordinates, the coordinates are then converted to the image coordinate system using simple geometric proportionality,

$$x' = Z_0 \frac{x}{z} \qquad y' = Z_0 \frac{y}{z}, \tag{22}$$

With $\boldsymbol{Z_0}$ representing the distance between the object and image plane (image distance) when the camera is in focus. This model neglects lens distortion with each object point and its corresponding image coordinates satisfying the pinhole camera model, even when the lens is out of focus.

4.1 Camera Calibration Method

Once an underlying understanding of the system was developed, the camera system could then be calibrated using the method outlined in Wang et al. [36] so as to determine the rotation and translation parameters for each known camera location. Building from knowledge of known matrix manipulation, a system of equations can be obtained based on equations 15 and 22 using the matrix form

$$B_{2N\times 11}\, y_{11\times 1} = b_{2N\times 1}$$

where substituting and rearranging equations 15 and 22 gets

$$\begin{aligned} Z_0(r_1 x_w + r_2 y_w + r_3 z_w + T_x) &= x'(r_7 x_w + r_8 y_w + r_9 z_w + T_z) \\ Z_0\big(r_4 x_w + r_5 y_w + r_6 z_w + T_y\big) &= y'(r_7 x_w + r_8 y_w + r_9 z_w + T_z) \end{aligned} \tag{23}$$

Rearranging these equations to obtain known values separated from the unknown values,

$$\frac{Z_0 r_1}{T_z} x_w + \frac{Z_0 r_2}{T_z} y_w + \frac{Z_0 r_3}{T_z} z_w + \frac{Z_0 T_x}{T_z} - \frac{r_7}{T_z} x' x_w - \frac{r_8}{T_z} x' y_w - \frac{r_9}{T_z} x' z_w = x'$$
$$\frac{Z_0 r_4}{T_z} x_w + \frac{Z_0 r_5}{T_z} y_w + \frac{Z_0 r_6}{T_z} z_w + \frac{Z_0 T_y}{T_z} - \frac{r_7}{T_z} y' x_w - \frac{r_8}{T_z} y' y_w - \frac{r_9}{T_z} y' z_w = y' \quad (24)$$

These equations can then be modelled as a linear set of equations in matrix form:

$$B = \begin{bmatrix} x_{w1} & y_{w1} & z_{w1} & 1 & 0 & 0 & 0 & 0 & -x_1' x_{w1} & -x_1' y_{w1} & -x_1' z_{w1} \\ 0 & 0 & 0 & 0 & x_{w1} & y_{w1} & z_{w1} & 1 & -y_1' x_{w1} & -y_1' y_{w1} & -y_1' z_{w1} \\ & & & & & \vdots & & & & & \\ & & & & & \vdots & & & & & \\ x_{wN} & y_{wN} & z_{wN} & 1 & 0 & 0 & 0 & 0 & -x_N' x_{wN} & -x_N' y_{wN} & -x_N' z_{wN} \\ 0 & 0 & 0 & 0 & x_{wN} & y_{wN} & z_{wN} & 1 & -y_N' x_{wN} & -y_N' y_{wN} & -y_N' z_{wN} \end{bmatrix} \quad (25)$$

$$y = \begin{bmatrix} \frac{Z_0 r_1}{T_z} & \frac{Z_0 r_2}{T_z} & \frac{Z_0 r_3}{T_z} & \frac{Z_0 T_x}{T_z} & \frac{Z_0 r_4}{T_z} & \frac{Z_0 r_5}{T_z} & \frac{Z_0 r_6}{T_z} & \frac{Z_0 T_y}{T_z} & \frac{r_7}{T_z} & \frac{r_8}{T_z} & \frac{r_9}{T_z} \end{bmatrix}^T \quad (26)$$

$$b = [x_1' \quad y_1' \quad \cdots \quad \cdots \quad x_N' \quad y_N']^T \quad (27)$$

where the entirety of y is unknown. In order to form an adequate numbered system of equations, there must be at least $N = 6$ noncoplanar feature points included to obtain a fully determined system. To reduce errors in the system, a total of more than 6 points are taken to form an over-determined system of equations, which is then solved using a least squares method to best fit the solution. The greater the number of feature points available for use, the greater the accuracy of the least squares solution.

Once a solution for y is established, each individual variable is found using isolated systems of equations aided by select relation equations that serve to allow fully determined systems. The next step takes a newly defined variable $a = \frac{T_z}{Z_0}$, and using the known solutions for $y(1), y(2), y(5)$, and $y(6)$, alongside the rotation matrix parameters satisfying

$$\sqrt{(r_1 + r_5)^2 + (r_2 - r_4)^2} + \sqrt{(r_1 - r_5)^2 + (r_2 + r_4)^2} = 2 \quad (28)$$

The coefficient a can be computed:

$$a = \frac{T_z}{Z_0} = \frac{2}{\sqrt{[y(1)+y(6)]^2+[y(2)-y(5)]^2}+\sqrt{[y(1)-y(6)]^2+[y(2)+y(5)]^2}}. \quad (29)$$

From this parameters $r_1 - r_6, T_x, T_y$ can be computed and using the known orthonormal and right handed properties of the rotation matrix, $r_7 - r_9$ can be determined,

$$r_7 = r_2 r_6 - r_3 r_5\,, \qquad r_8 = r_3 r_4 - r_1 r_6\,, \qquad r_9 = r_1 r_5 - r_2 r_4. \quad (30)$$

The remaining parameters can be systematically solved utilizing geometric optics concepts in the Gaussian lens equation and geometric proportionality,

$$\frac{1}{z} + \frac{1}{z_{img}} = \frac{1}{f_{lens}}\,, \qquad \frac{x_{img}}{x} = \frac{y_{img}}{y} = \frac{z_{img}}{z} \quad (31)$$

where the image position $(x_{img}, y_{img}, z_{img})$ is any position considered out of focus. These relations can then be substituted with values of a chosen focus point (x_f, y_f, z_f) to allow ample equations to converge on a determined solution,

$$\frac{1}{z_f} + \frac{1}{Z_0} = \frac{1}{f_{lens}}\,, \qquad \frac{x_f{}'}{x_f} = \frac{y_f{}'}{y_f} = \frac{Z_0}{z_f}. \quad (32)$$

Calibration for each camera location incorporated the discussed solution method above and was conducted utilizing a unique cylindrical calibration piece (Figure 6).

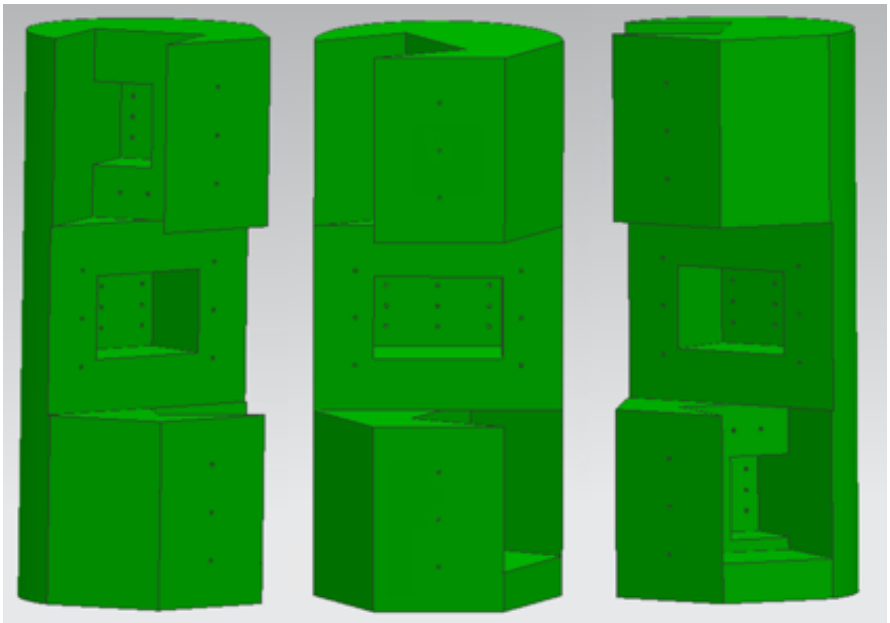

Figure 6. Calibration cylinder used to depict 39 non-coplanar points in flame spatial domain.

The calibration cylinder consisted of 39 individual feature points spread across separate three-dimensional planes at different orientations. All point locations in the world coordinate system were known, while calibration images were taken at each of the 11 camera locations so as to obtain image pixel coordinates for the viewed feature points. The maximum number of points viewable at each location were taken from the images and using the developed calibration code (Appendix C), the camera rotation and translation parameters were acquired for all 11 camera locations. The results of the camera calibration are given in Table 1,

Camera #	1	2	3	4	5	6	7	8	9	10	11
Yaw (deg)	-73.84	-61.85	-47.21	-33.07	-16.15	-2.64	12.20	31.47	44.96	65.80	71.30
Pitch (deg)	2.04	-1.10	-0.06	-0.20	0.28	0.41	0.03	0.89	1.12	5.21	9.73
Roll (deg)	2.78	-0.81	-0.36	-1.03	-0.53	-0.94	-0.40	0.07	0.38	-3.51	-8.68
T_x **(mm)**	10.44	6.76	10.28	9.90	10.60	4.04	8.62	8.37	13.75	11.53	12.17
T_y **(mm)**	-111.36	-106.07	-106.71	-105.89	-105.42	-105.10	-106.44	-110.87	-110.92	-107.86	-109.32
T_z **(mm)**	1126.37	1117.65	1117.48	1108.36	1107.08	1114.35	1105.05	1109.99	1107.69	1107.05	1107.12
Z_0 **(mm)**	115.78	115.89	115.88	115.99	115.99	115.91	116.02	115.95	115.98	115.97	115.95

Table 1. Calibration results.

It is worth noting that both the pitch and roll angles are near zero, which agrees with the fact that the cameras are perpendicular to the horizontal plane, and the yaw angles are roughly 15° separated apart illustrating each evenly spaced camera view. These preliminary calibration results prove the accuracy of the camera calibration technique, providing evidence that the rotation and translation parameters for each location were correctly calibrated.

4.2 Iterative Algorithm Development & Phantom Case

In order to determine the functionality and sufficiency of an iterative algorithmic solver for chemiluminescence fields, a phantom image study was conducted first as an attempt to reconstruct a known function. The phantom function used in this study was obtained from Geraedts et al. [22],

$$f(r,\theta,z) = \begin{cases} P(r,\psi,z) = \sin(2\pi r)\ \cdot \cos(\psi + z \cdot 2\pi) \cdot (\sin(z \cdot \pi))^2 & r \le R \\ 0 & r \ge R \end{cases} \quad (33)$$

modeled as a single helical mode structure to best represent a flame. Due to the phantom function inherently containing both negative and positive values in its solution, the reconstruction phantom was artificially shifted by a constant value. This was done to prevent the erratic convergence issues brought on by negative phantom function values due to the

multiplicative nature of the reconstruction algorithm. The end reconstruction was then shifted back to its original location once convergence was ultimately reached. The phantom flame data was modeled over a 100 mm^3 voxel cube space for reconstruction across $N_v = 64^3$ number of voxels and is represented in a single row vector $f(x_{wn}, y_{wn}, z_{wn})$. The image intensity for each pixel at each projection view can be formulated as,

$$I(p,q) = \sum_{n=1}^{N_v} f(x_{wn}, y_{wn}, z_{wn}) \cdot w(x_{wn}, y_{wn}, z_{wn}; p, q) \tag{34}$$

corresponding to the previously discussed projection operator in chapter 3 (equation 7). In this equation, p denotes the index of the pixel, while q represents the index of the camera location. The weight ratio values are denoted by $w(x_{wn}, y_{wn}, z_{wn}; p, q)$ and represent the optical density contribution for the nth voxel located at (x_{wn}, y_{wn}, z_{wn}) for the pixel p and camera location q. When conducting Flame Chemiluminescence Tomography, the image intensities are directly captured by the camera imaging system; this means that in order to successfully reconstruct the object f, the weight factors w must first be determined.

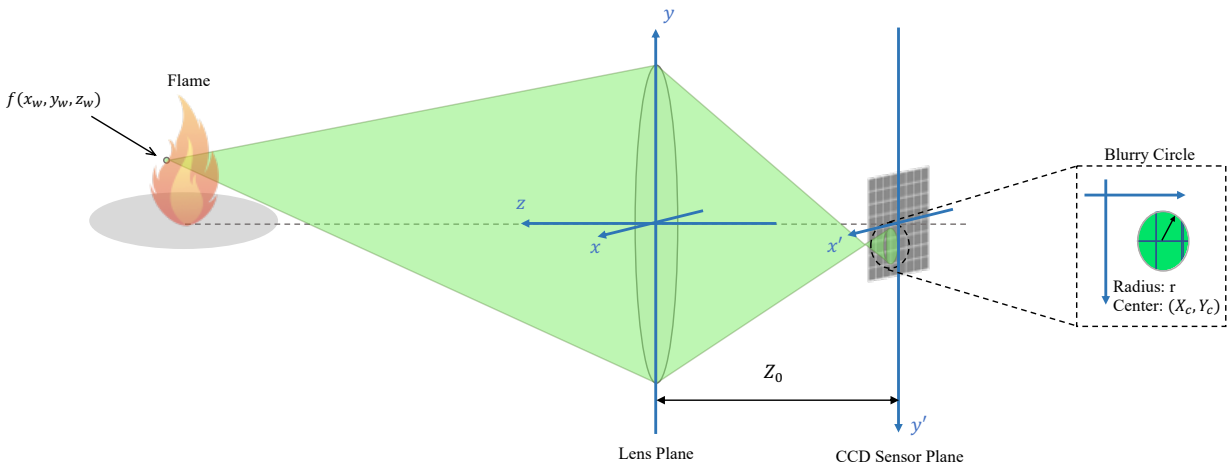

Figure 7. Coordinate system conversion with example blurry circle projected onto sensor [36].

Noting the projection process illustrated in Figure 7, a voxel located at (x_w, y_w, z_w) in the flame domain is first converted to lens coordinates (x, y, z) using equation 15, followed by a conversion to image coordinates $(x_{img}, y_{img}, z_{img})$ using equation 22. Next it follows since the focal image distance of the camera Z_0 is fixed, all points falling before and after the focal image plane appear as blurry circles on the sensor. It is then necessary to calculate the center coordinates (X_C, Y_C) and radius r of each blurry circle found on the camera sensor,

$$r = \frac{|z_{img} - Z_0|}{2z_{img}} D; \quad X_C = x_{img} \frac{Z_0}{z_{img}}; \quad Y_C = y_{img} \frac{Z_0}{z_{img}}, \tag{35}$$

With D representing the aperture of the camera. The blurry circles are so numbered on the CCD sensor plane that they overlap and intersect; this intersection area is then calculated to determine the contributions across each pixel of specified constant area on the sensor. From this analysis two distinct scenarios emerge: first (1) the diameter of the blurry circle is greater than the pixel size, or second (2) the diameter of the blurry circle is smaller. To simplify the analysis, it is assumed that the pixels located on the outside edge of the blurry circle are themselves circles with the intersection area varying linearly with the separation l of the two blurry circle centers. The area concentration ratios are determined by,

$$\frac{A_i}{A_b} = \begin{cases} \frac{A_p}{A_b} & l \le r - \frac{d_p}{2} \\ \frac{r + \frac{d_p}{2} - l}{d_p} \cdot \frac{A_p}{A_b} & r - \frac{d_p}{2} < l < r + \frac{d_p}{2} \quad for \left(r \ge \frac{d_p}{2}\right) \\ 0 & l \ge r + \frac{d_p}{2} \end{cases} \tag{36a}$$

$$\frac{A_i}{A_b} = \begin{cases} 1 & l \leq \frac{d_p}{2} - r \\ \frac{r + \frac{d_p}{2} - l}{2r} & \frac{d_p}{2} - r < l < \frac{d_p}{2} + r \quad for\ \left(r < \frac{d_p}{2}\right) \\ 0 & l \geq \frac{d_p}{2} + r \end{cases} \tag{36b}$$

where A_i is the intersection area, A_b is the blurry circle area, A_p is the area of the pixel, and d_p is the diameter (length) of the pixel. Because the intensity contributions of each voxel to the pixels are shown as $I = f(x_{wn}, y_{wn}, z_{wn}) \cdot \frac{A_i}{A_b}$, it is concluded that the weight ratio values are given by $w = \frac{A_i}{A_b}$. This process is repeated for every single voxel, for every single pixel, on every single camera, resulting in solved weight factors for the entire tomography system domain.

Once all weight factors for all known variables are acquired, the MART multiplicative algorithm (equation 10) can be implemented. All weight ratio values were concatenated and combined into a single large matrix w_{pq}, while intensity values for all pixels at each camera location were combined into a single variable I_{pq}. It is common to employ a relaxation factor β to reduce overall reconstruction noise and improve system convergence and stability. From previous work [26, 60] it can be shown that stronger relaxation factors ($\beta << 1$) must be used when there is significant error present typically found in non-exact projection geometries. Conversely, it is possible to use higher (i.e. weaker) relaxation factors for more exact projection geometries, proving most advantageous when dealing with strip integrals and unavoidable projection noise. In this study, a relaxation factor of .85 was chosen for the phantom reconstruction case, given the exactness of the phantom integral projections.

To establish a viable convergence stopping criterion for the iterative reconstruction, the reconstruction iterations were performed for an initial iteration count of 1.5 million iterations and the convergence criteria (equation 14) was monitored. The criteria c, a scaled representation of

the maximum absolute difference between each successive iteration, was plotted to visualize where the criteria began to converge to a single value (Figure 8).

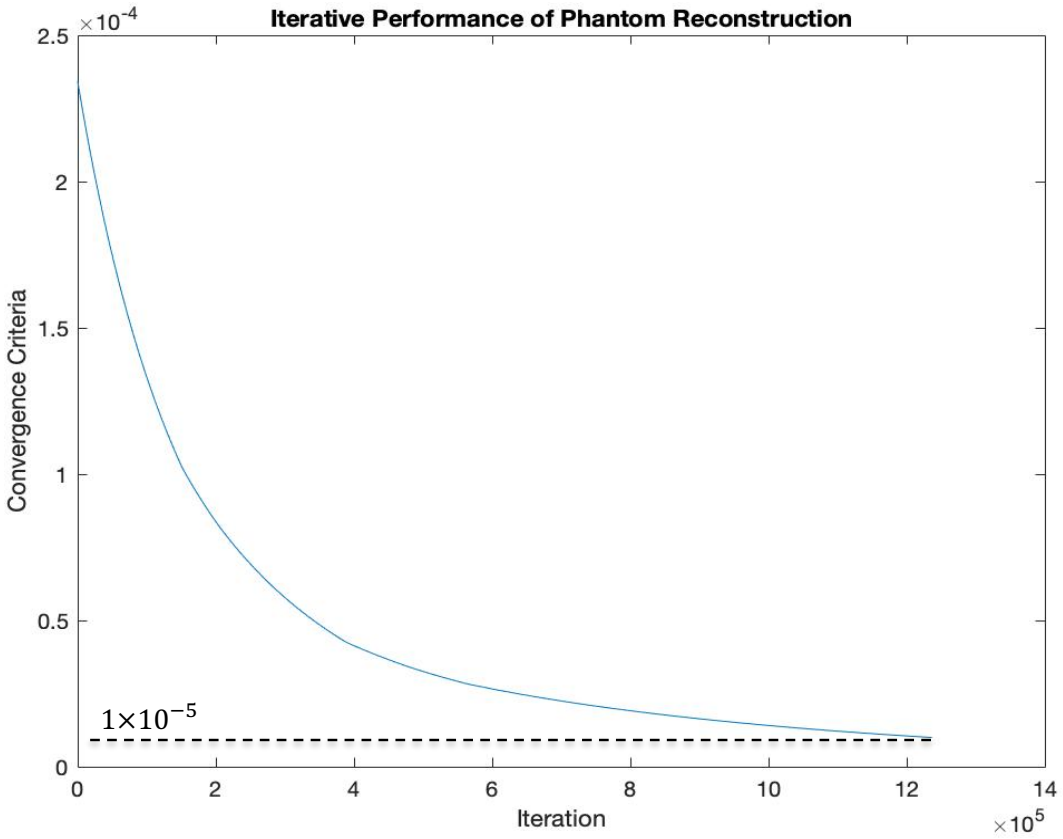

Figure 8: Convergence criteria plotted across iteration count for establishing stopping value. The convergence curve is shown to level out roughly at 1×10^{-5}.

Based upon this and evidence demonstrated in previous literature [26], a convergence criteria of $c \leq 10^{-5}$ or $.001\%$ was used to end the reconstruction. This technique allowed for the best performance in reconstructing the original phantom from the altered function, and the results are shown in Figure 9. The initial value f^0 was an altered initial guess phantom and was used to show convergence from a dissimilar structure to the original desired function.

Figure 9. Comparison of the (a) initial guess, (b) desired original phantom function, and (c) final phantom flame reconstruction.

The phantom flame was also reconstructed at four different camera viewing angle counts of 11, 9, 7, and 5 to demonstrate the understanding of effective reconstruction accuracy as a function of number of viewing angles. Results in Figure 10 qualitatively show that by decreasing the respective number of camera viewing angles, the accuracy of the reconstruction decreases significantly.

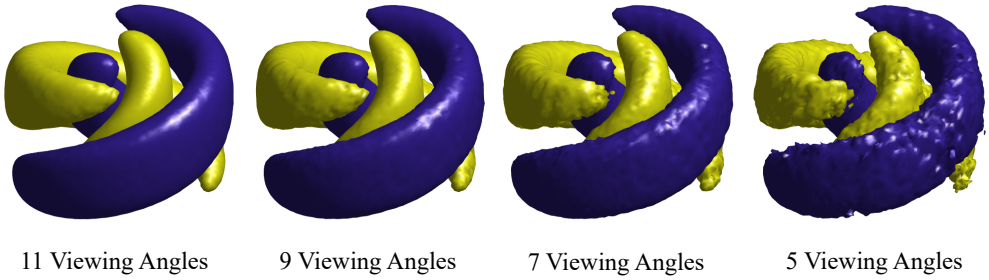

Figure 10. Reconstruction accuracy demonstrated with four different camera viewing angle counts.

This was quantitatively explored using a standard error analysis to illustrate and confirm the varying levels of convergence accuracy based on the number of camera viewing angles used. As illustrated in Figure 11, the standard error between the reconstructed case and the original phantom flame function decreases dramatically with an increase in camera viewing locations.

The standard error depicted in this work consists of applying a unity-based normalization to the reconstruction and phantom data (equation 37), followed by the spatially averaged error across all voxel reconstruction values (equation 38).

$$X' = \frac{X - X_{min}}{X_{max} - X_{min}} \tag{37}$$

$$\epsilon = \frac{\sum \left| \frac{f_{reconst} - P}{P} \right|}{V^3} \tag{38}$$

This analysis confirms the choice of 11 camera viewing angles as sufficient given a relatively low standard error of .0096 or .96%, and is further supported by the standard error analysis performed by Geraedts et al. [22].

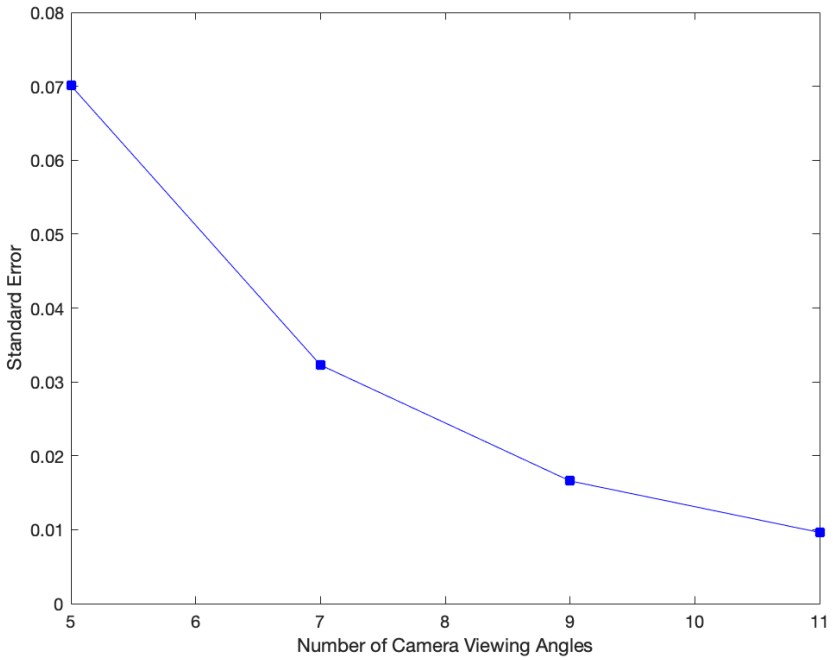

Figure 11. Standard error vs. number of viewing angles.

Once the phantom flame case was shown to be successfully reconstructed, it was time to apply the iterative reconstruction technique to a real experimental scenario.

4.3 Experimental Setup

Data collection for the experimental flame imaging was conducted in the fundamental diagnostics test cell in the Advanced Propulsion and Power Lab at Virginia Tech. Experimental measurements were taken using an atmospheric combustor capable of producing lean, partially-premixed swirl stabilized flames for analysis. A Photron FastCam SA5 Ultra High-Speed Camera was used in taking data measurements, attached to a SIL3-25HG50D Compact Image Intensifier with a 105 mm focal length lens attachment. The camera setup was configured on a two-piece mount system connected to a 60 in. piece of 80-20 Aluminum bar protruding from the combustor test section. The bar was attached to a free moving brace connected to the atmospheric combustor rig, which allowed the camera to be strategically maneuvered into each desired camera location. An angle marker was attached to the brace to properly align the camera setup to the desired angle. The camera was aimed directly at the base of the dump plane (Figure 12) and was manually adjusted to capture the entirety of the flame within the quartz cylinder.

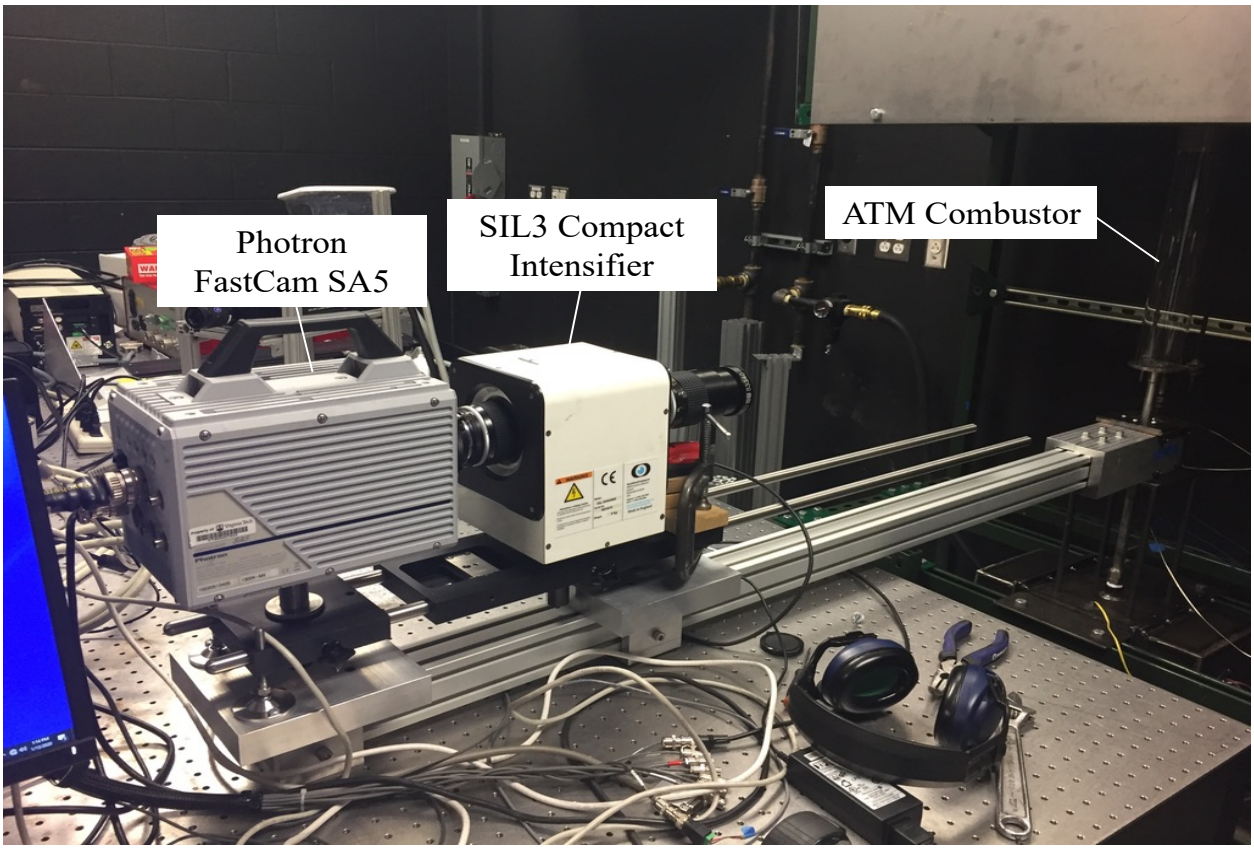

Figure 12. Atmospheric rig setup consisting of high-speed camera and intensifier attached to swivel arm, circling atmospheric combustor.

The combustion system consisted of two speaker box housings connected to a central air plenum containing the air-fuel mixing tube running to the top of the dump plane. At the end of the tube, a flame swirler of 18 mm diameter served to mix the air and gas flows before entering the dump plane. Methane was used as fuel for the lean, partially-premixed turbulent flame, coupled with supplied oxygen through the air compressor in the lab to institute combustion. Once ready for testing, a torch ignitor was used to ignite the air-gas mixture at the top of the quartz, burning off any excess fuel in the quartz and supplying a constant turbulent flame at the base of the dump plane.

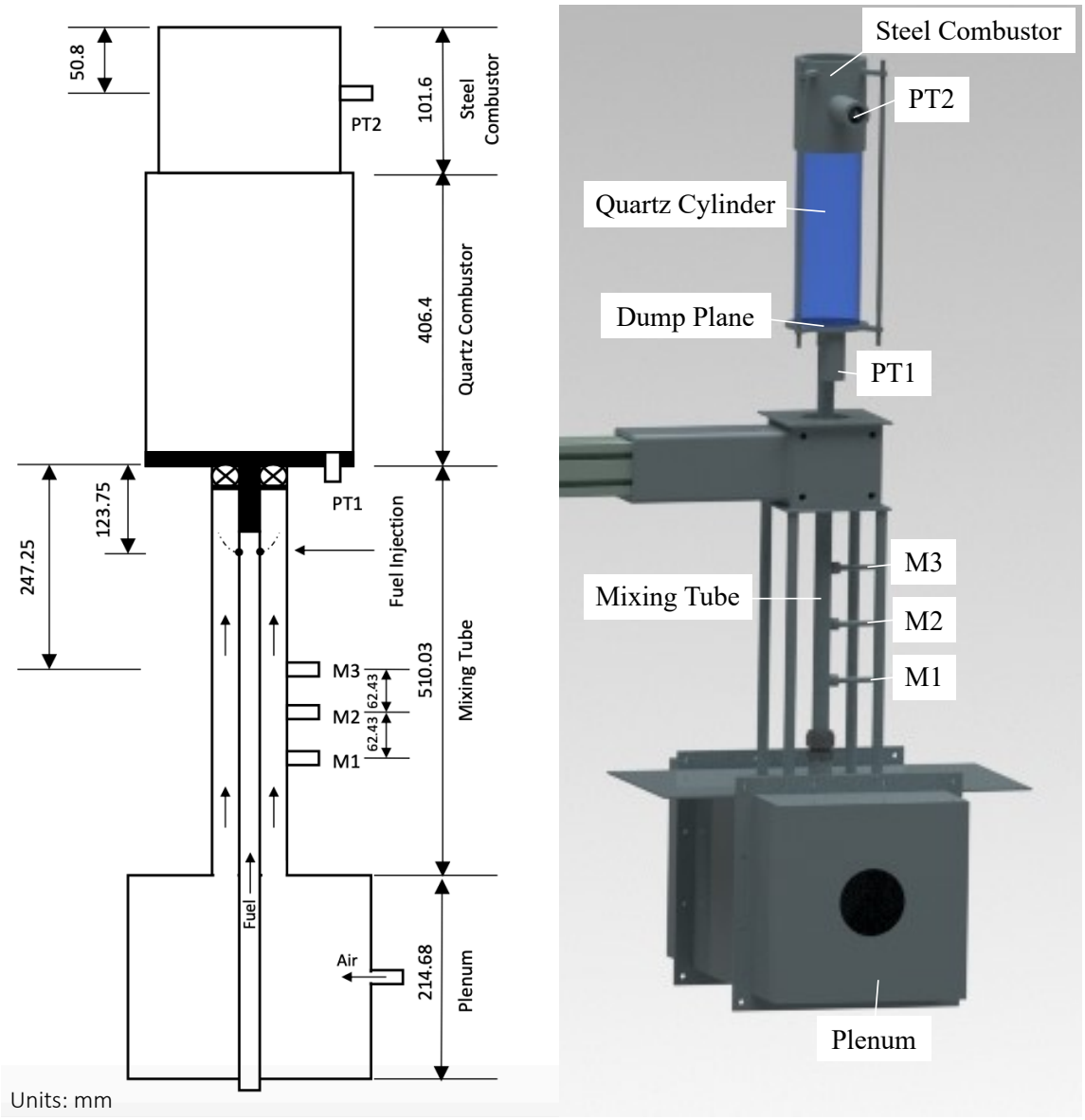

Figure 13. Schematic of scaled atmospheric combustor rig.

Three microphones (PCB ¼″ ICP microphone system, model number: 377C10) were attached to the vertical mixing tube, along with two dynamic pressure transducers (Kistler 6025A) at the top of the steel combustion holder and at the base of the dump plane to provide ample pressure data capture. The microphones maintained a sensitivity of 2 mV/Pa, while the dynamic pressure transducers maintained a sensitivity of 103 pC/bar and could operate up to 700° C with signals amplified by a charge amplifier with a 200 mV/pC gain. An inflow K-type

thermocouple was placed inside the air plenum to monitor the inlet air temperature, and all data apparatus connected to the rig were controlled and monitored using an integrated LabView dashboard user interface. The mass flow rate, temperature, and pressure transducers/microphones were respectively sampled at 1 Hz, 90 Hz, and 100 kHz for this study.

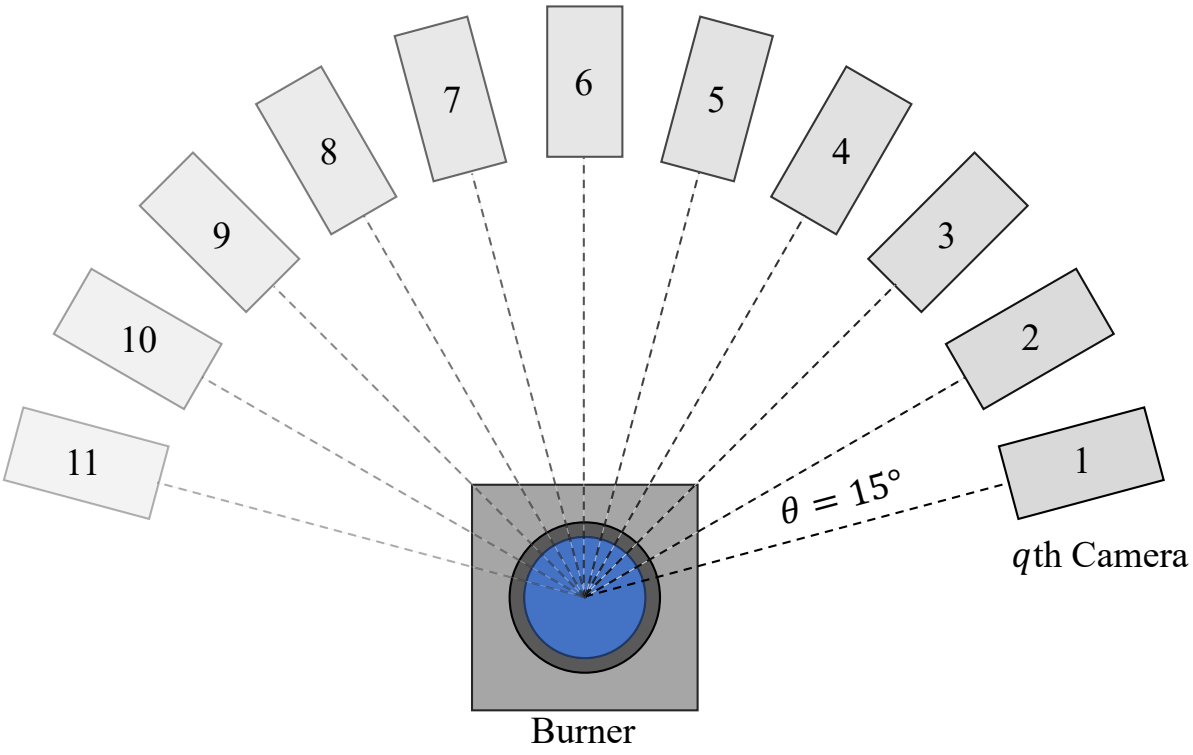

Figure 14. Designated camera locations placed at 15° increments around the flame.

A total of 22 measurements were taken, a measurement for both CH* and OH* radicals at each of the 11 camera locations. Chemiluminescence intensities were captured using monochromatic filters of 430 nm with a FWHM of 10 nm for CH*, and 310 nm with a FWHM of 10 nm for OH* respectively. All measurements were taken at an acoustically forced excited state, whereby a set of Axxera Mid-Range Speakers attached to a Crown XLS Amplifier were powered to a 250 Hz sine wave. This allowed the capturing of the chemiluminescence fields at acoustically forced conditions. The camera specifications were adjusted to the parameters

outlined in Table 2 and maintained a maximum resolution of 1024 x 1024 pixels on the imaging sensor.

Camera Specifications	
Gain	10
Exposure Time	150 μs
Delay	55 ns
Framerate	5000 fps
Resolution	1024 x 1024

Table 2. Camera specifications chart.

Fluid flow characteristics through the atmospheric combustor were set using a LabView integrated data acquisition system, with all system connections going through a centralized DAQ terminal block chassis powered via an external power supply. A series of mass flow controllers (Alicat MCR-50SLPM-D-DB15/CM and MCR-500SLPM-D/CM) monitored the flow rates of both the incoming fuel and air, respectively, with air and fuel flow capabilities of 10.34 g/s and .546 g/s, and a measurement uncertainty of ±0.8% for both controllers correlating to 82.6 mg/s and 4.37 mg/s, respectively. Air flow was established at 150 standard L/min and a global equivalence ratio of .75 was instituted for the flow to provide ample conditions for peak acoustic excitement. This coupled with the introduction of a 250 Hz frequency sine wave created a sustained acoustic instability in the system, providing the desired forced excitation conditions for the intended study.

Chapter 5: Results & Discussion

5.1 Phase Average Image Processing

Upon the collection of adequate flame imaging data, a necessary method of phase averaging across the instability was introduced to acquire sufficient images for reconstruction. The technique of phase averaging involves acquiring the mean of a wave characteristic across one full cycle; this typically requires the wave be divided into interval sections, or phases, with the phases being respectively averaged across all cycles.

The data recordings were stored as 1 second video files with the camera recording at 5,000 fps, each data file thus containing a total of 5,000 frames. An arbitrary number of 100 cycles was chosen for extraction from the recorded data, with each cycle representing a single wavelength or one period of the forced instability. When dividing into cycles, the max number of cycles is dependent on the camera frame rate and thus the number of images stored on the data recording file. Given the nature of the wave-like properties of the acoustic instability, it was not feasible to sync the recording start with the beginning of the instability wave. The pressure data therefore had to be plotted to determine the starting frame at which the instability peaked (Figure 15).

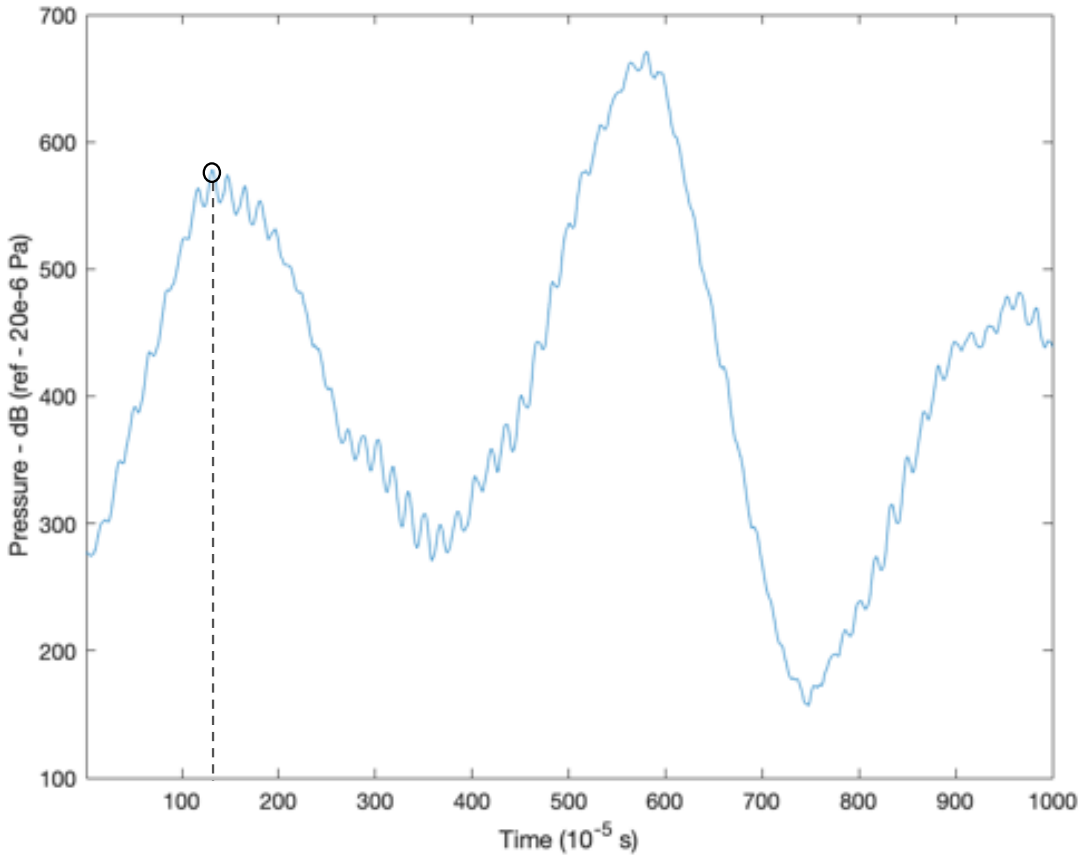

Figure 15. Pressure from PT1 at dump plane plotted to determine the starting frame. In this example, the instability peaks roughly at 120 · 10^{-5} s, leading to a start at frame 6.

The pressure transducer was set to collect data at 100,000 Hz, while the camera collected frame data at a frequency of 5,000 fps; it can be deduced that 20 pressure data points were present for every 1 frame. In order to acquire the starting frame value, the first occurring pressure peak value was subsequently divided by 20 in order to obtain the first frame showing the instability.

At a 250 Hz instability, there maintained 20 frames per cycle, and with the gathered number of cycles, a total of 2,000 frames were extracted from each data recording sample. Figure 17 shows the instability frequency spikes across a discrete frequency range for all data collecting apparatus, with clear instabilities arising at every 250 Hz mark. Each cycle was then split into 10 phases, with each respective phase being averaged across all 100 instability cycles.

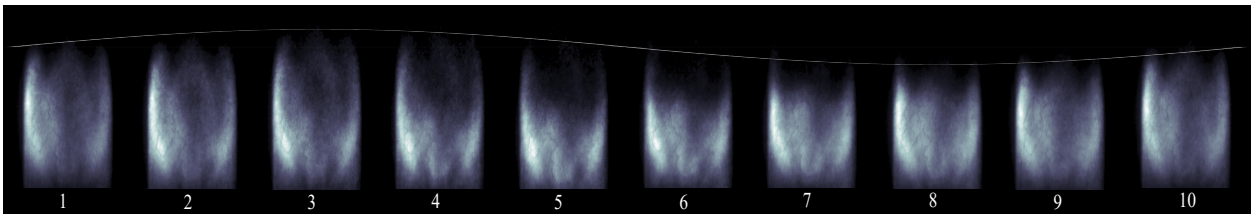

Figure 16. Acoustic instability wave visually shown in the flame across all 10 phases at 15 ° location.

Low-level pixel intensity noise was filtered out to avoid added inadvertent noise in the reconstructions, and the final phase averaged intensities were normalized and compiled by phase for all 11 camera locations for both CH* and OH*, resulting in a total of 220 images for reconstruction.

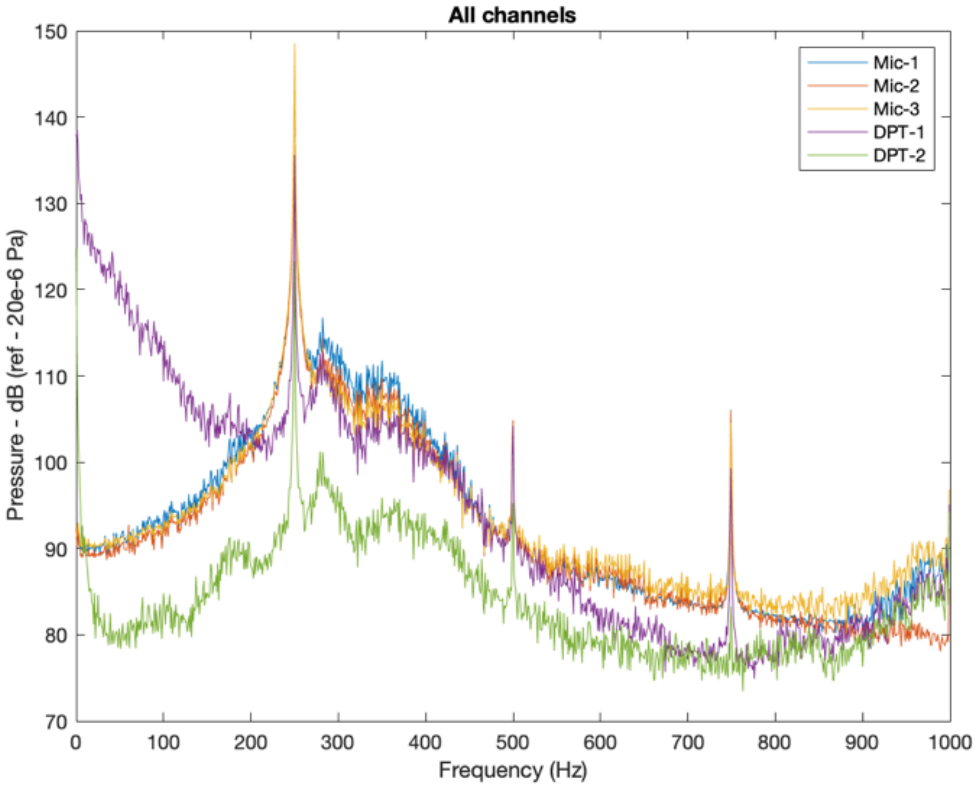

Figure 17. Instability frequencies shown for all pressure data collecting apparatus.

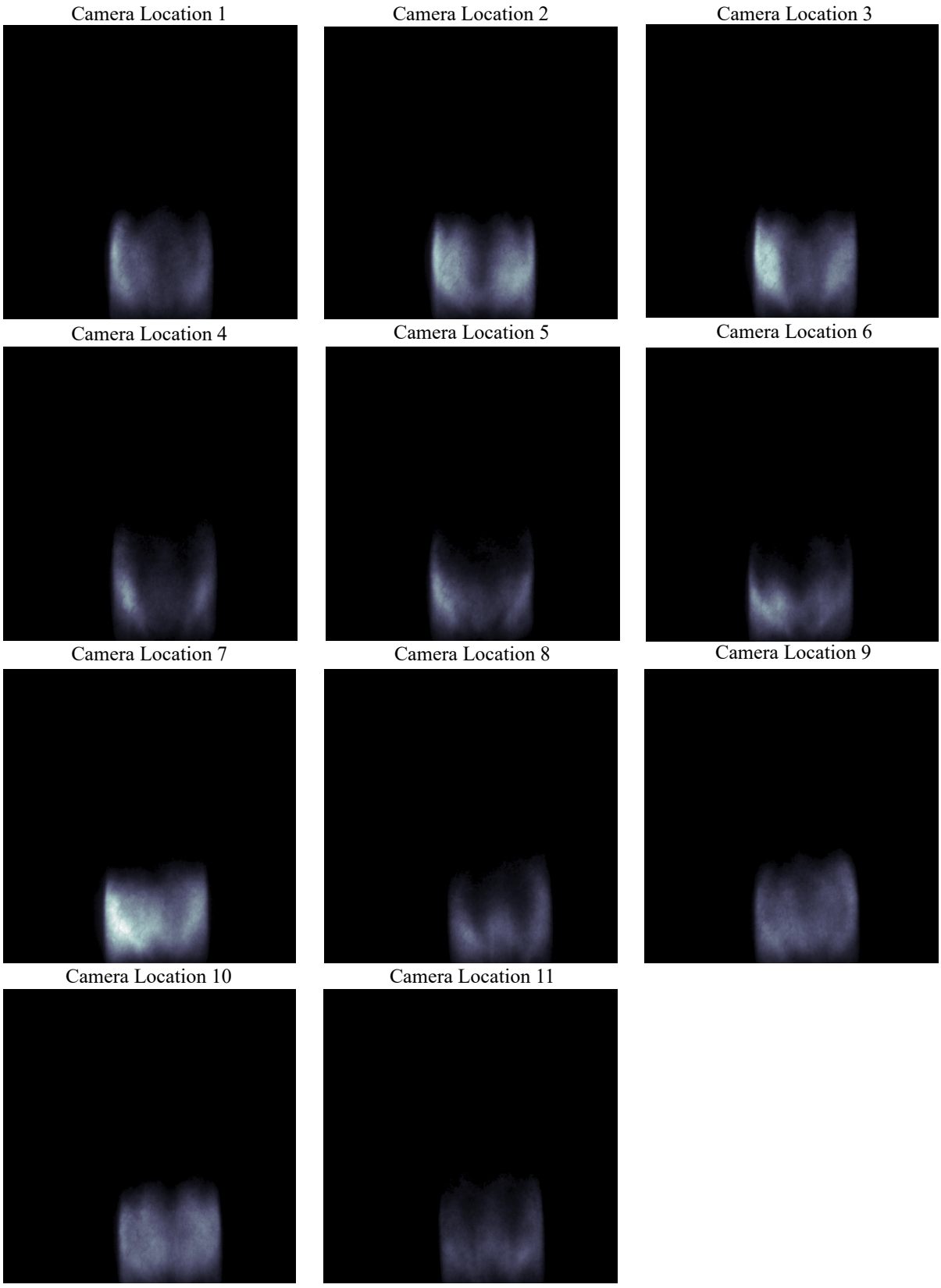

Figure 18. Phase 1 averaged intensity images for CH at all 11 camera angle locations.*

5.2 Inverted Abel Transform

When initializing the iterative reconstruction process, an initial volumetric guess value for the flame structure was used to instigate and commence the iterations towards a solution. In this study, the method of inverse Abel transformation was used to convert a 2D cross-sectional projection of the phase averaged images into a 3D volumetric object for initialization. The process consisted for each individual phase averaging all 11 camera location images into a single image to allow for an optimum 3D guess volume representation. The image was processed using the Basis Set Expansion (BASEX) Abel transform method developed by Dribinski et al. [61] creating a perfectly symmetric 2D cross section, then being revolved around its central axis to create a axisymmetric three-dimensional object.

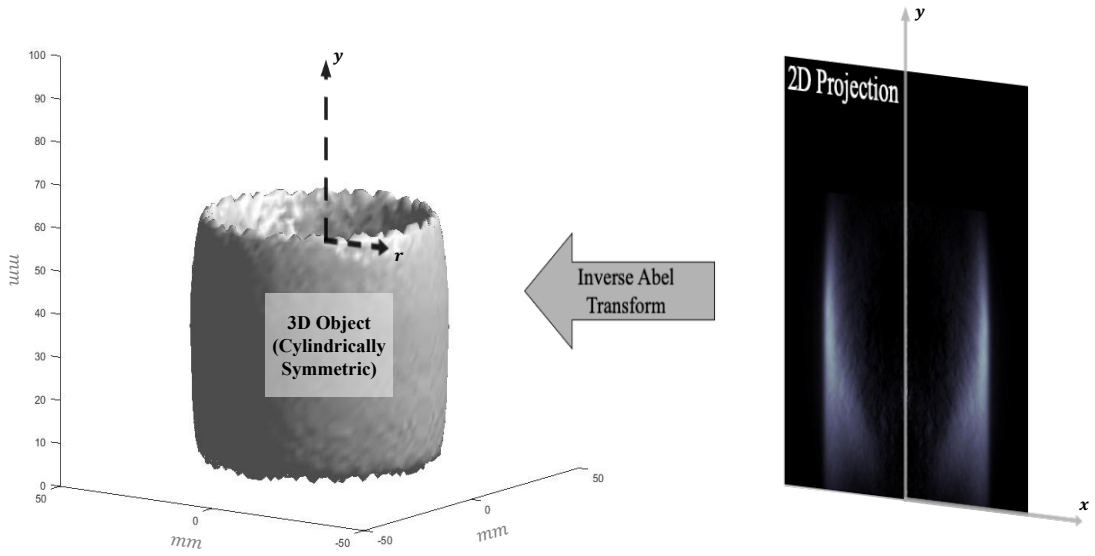

Figure 19. The inverse Abel transform mathematically obtains the 2D cross-section projection (right) and revolving it about the central symmetric axis obtains the 3D object (left).

This symmetric object would serve to uniformly initialize the iterative processing of the flame volumetric data and proved acceptable as an initial guess input in the iterative reconstruction solver.

5.3 CH* & OH* Field Reconstructions

Species chemiluminescence fields were reconstructed using the developed MART algorithm program shown in Appendix A, while the weight ratio values utilized in the reconstruction process were separately computed prior to the iterative algorithm submission using the code shown in Appendix B. Flame fields are shown in Figures 20-27 to illustrate the species field structure, while a cross-section planar view of the flame species gradient depicts the general U-shape formation of the flame interior. The flame wall is visibly outlined near -40 and 40 mm, matching the location of the combustor quartz inner wall with values beyond this deemed exterior noise. Only values located inside the known quartz region were used in the spatial equivalence ratio analysis, with the presence of exterior noise surrounding the quartz region discussed further in section 5.4. The reconstructed flame shows an internal flame cavity down the central axis of the reconstruction similar to the initial inverse Abel guess function, suggesting the Abel transform method is an accurate initial estimation to start the iteration process. The maximum volumetric flame values can also be shown to fluctuate alongside the general height of the flame field with the progression of phase, as expected given the oscillatory nature of the imposed acoustic excitation.

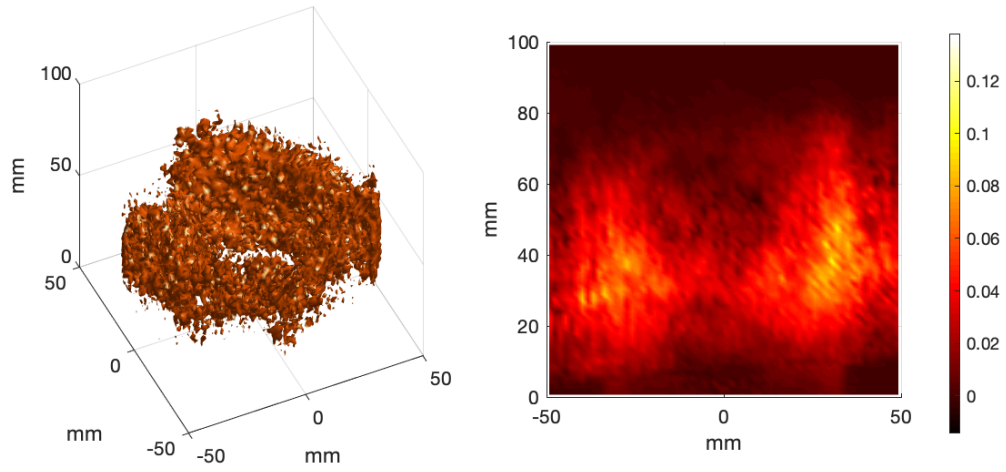

Phase 1

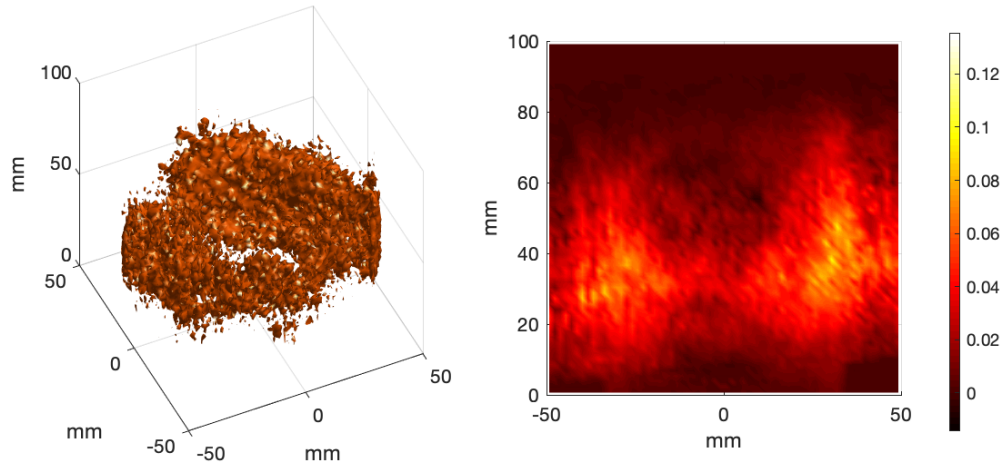

Phase 2

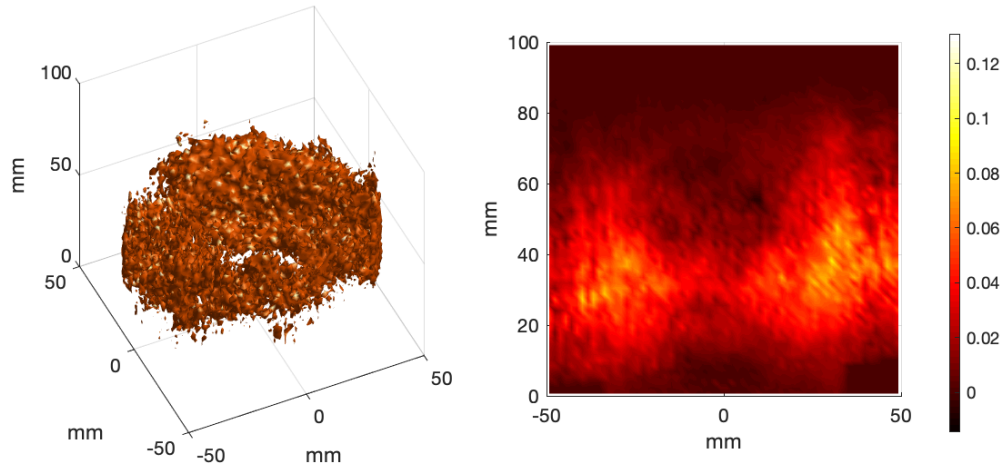

Phase 3

Figure 20. 3D Isosurface of 40% max volumetric value (left) and XY planar contour slice (right) of CH intensities for phases 1-3.*

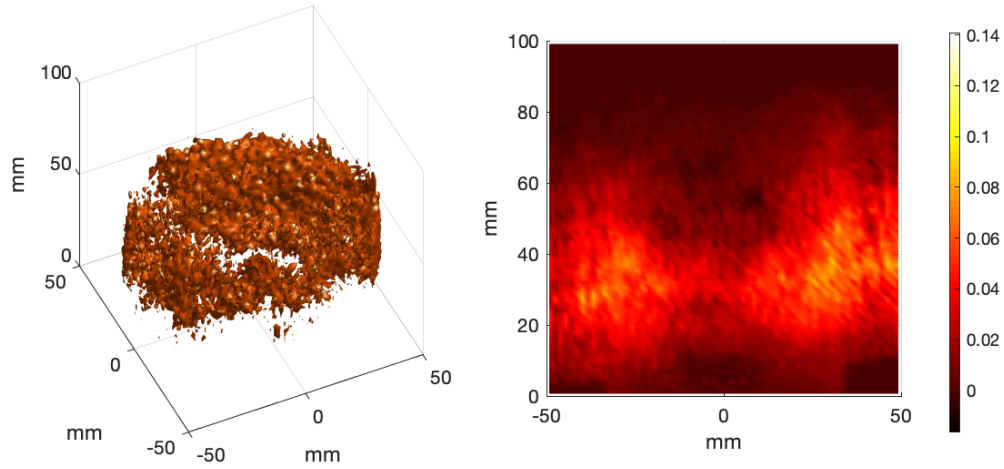

Phase 4

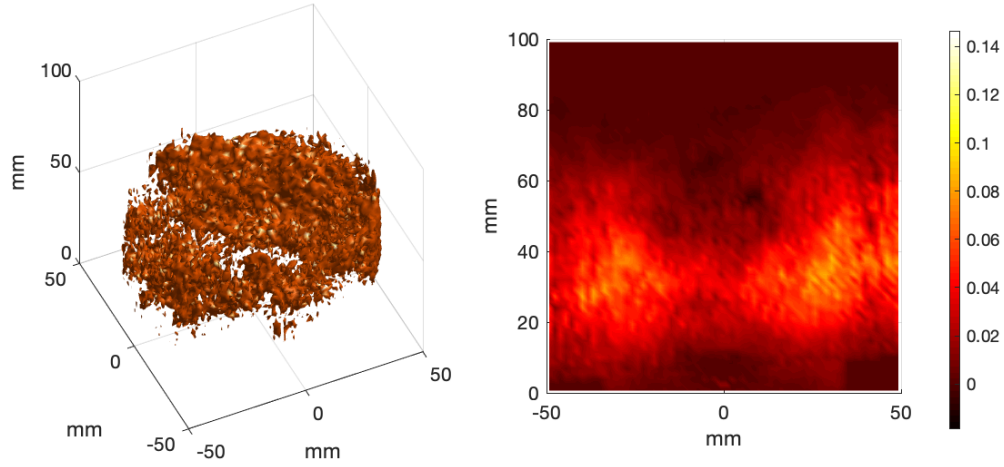

Phase 5

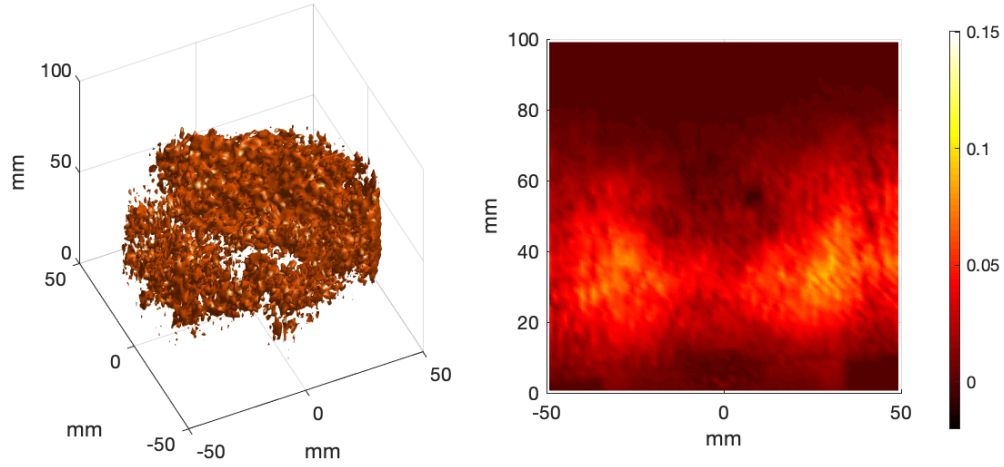

Phase 6

Figure 21. 3D Isosurface of 40% max volumetric value (left) and XY planar contour slice (right) of CH intensities for phases 4-6.*

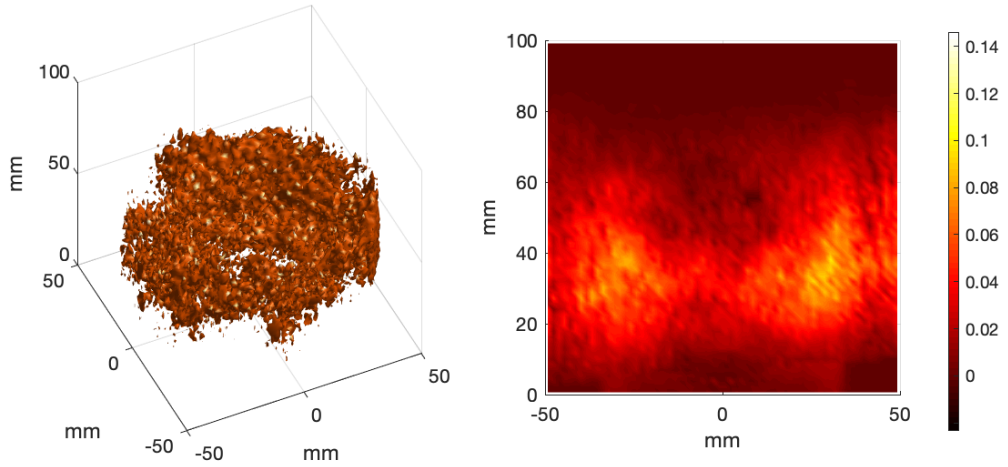

Phase 7

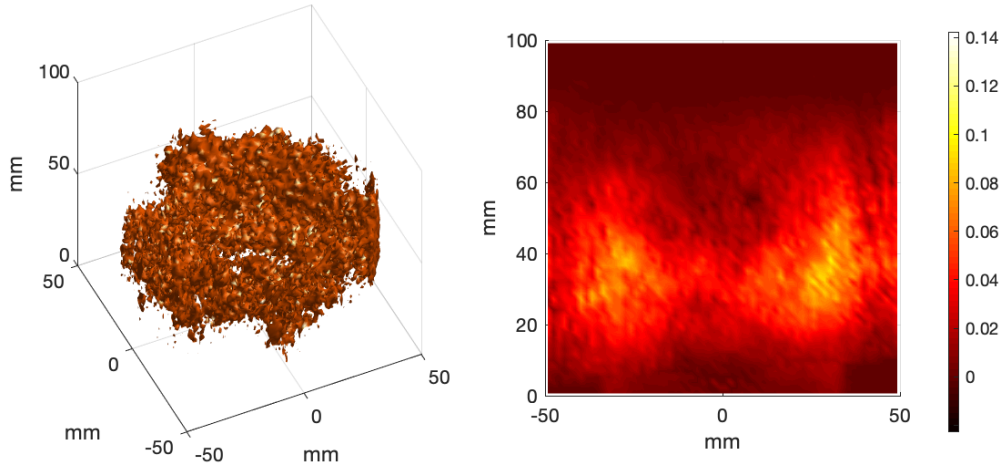

Phase 8

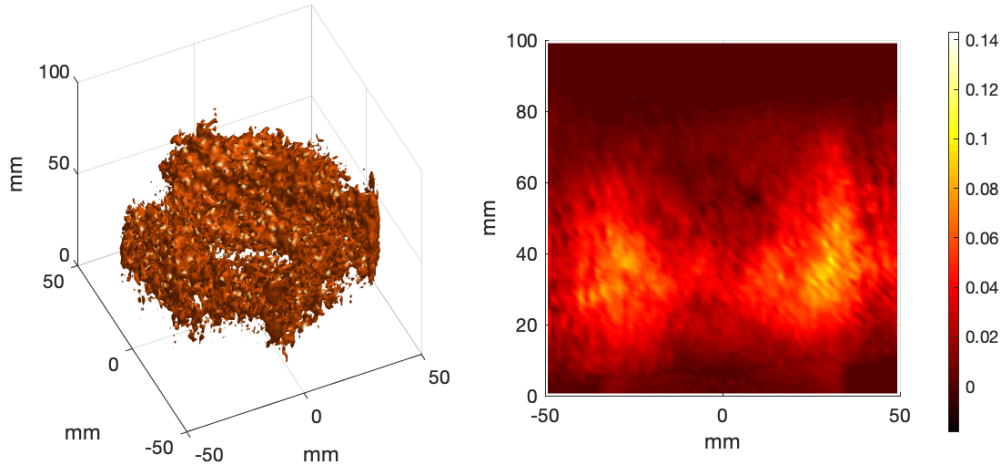

Phase 9

Figure 22. 3D Isosurface of 40% max volumetric value (left) and XY planar contour slice (right) of CH intensities for phases 7-9.*

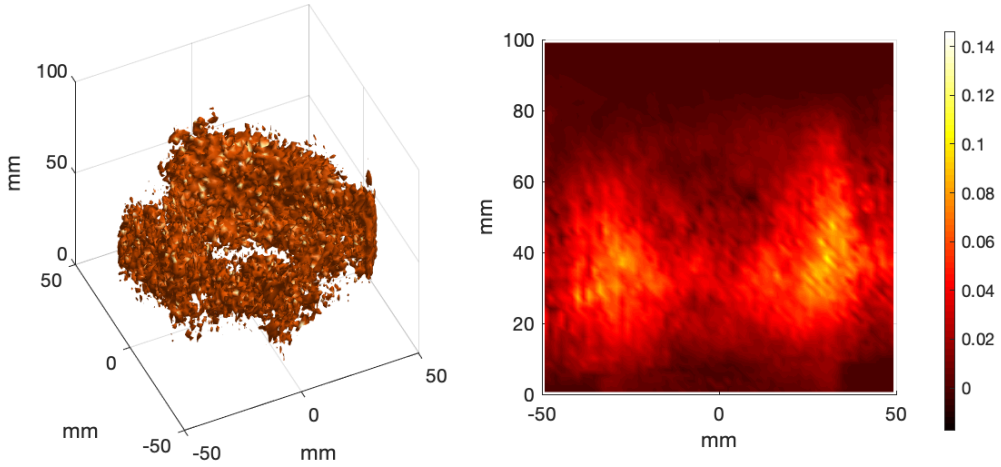

Phase 10

Figure 23. 3D Isosurface of 40% max volumetric value (left) and XY planar contour slice (right) of CH intensities for phase 10.*

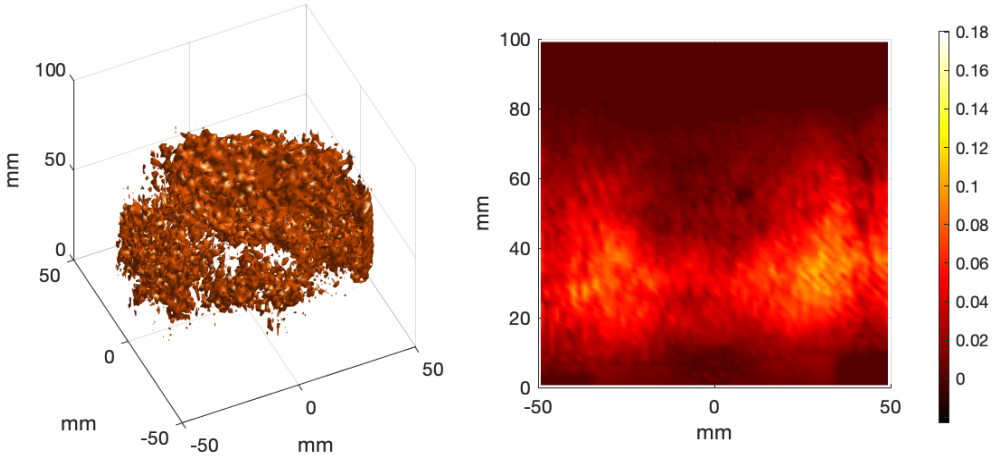

Phase 1

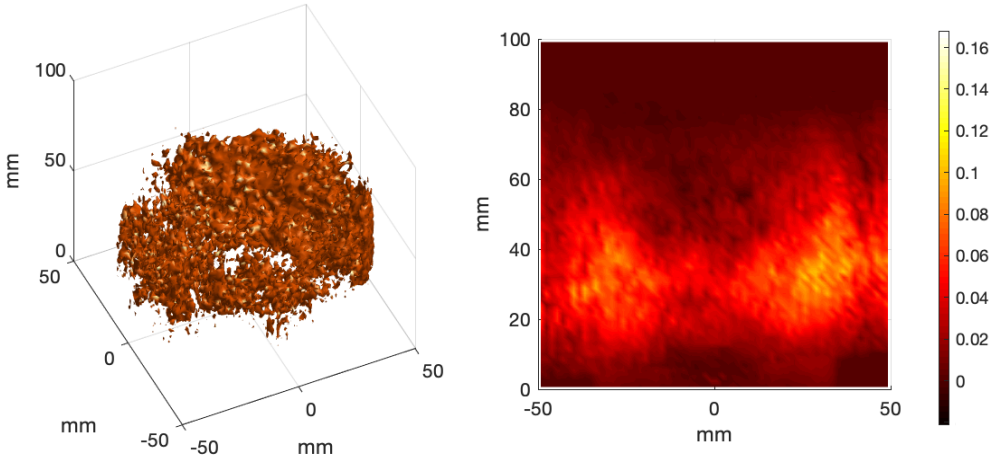

Phase 2

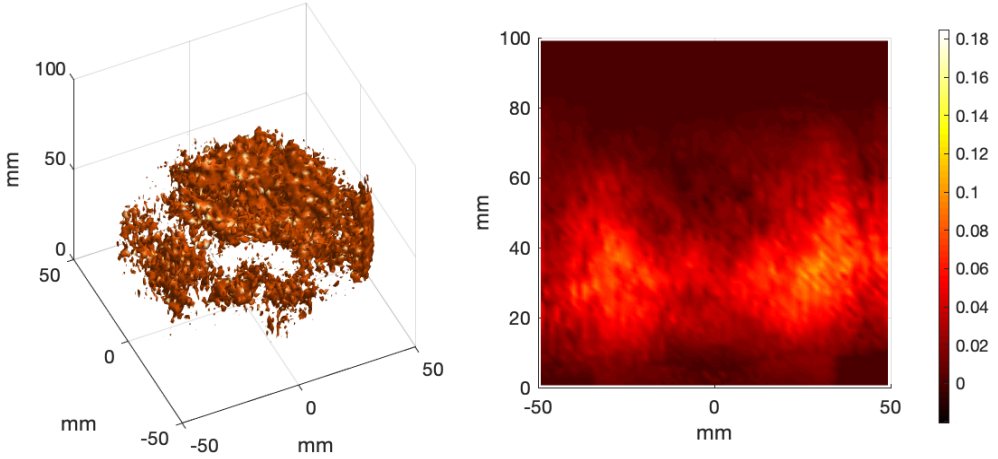

Phase 3

Figure 24. 3D Isosurface of 40% max volumetric value (left) and XY planar contour slice (right) of OH intensities for phases 1-3.*

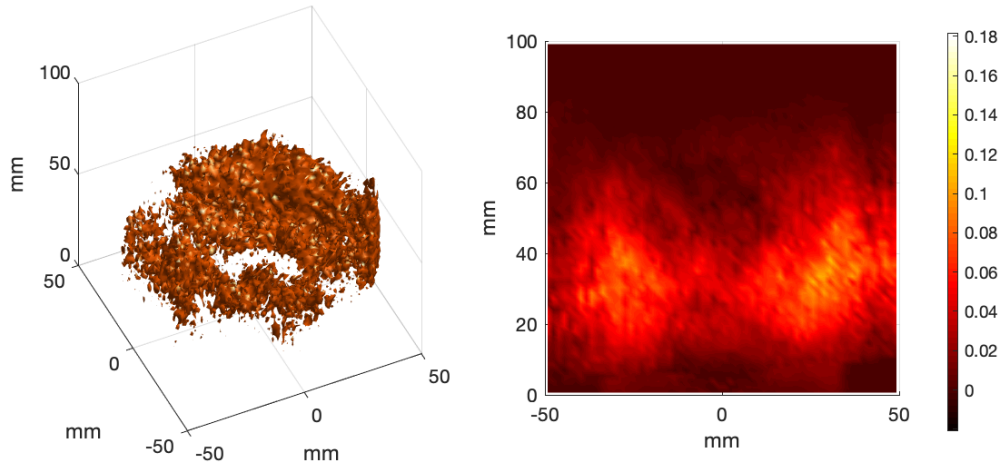

Phase 4

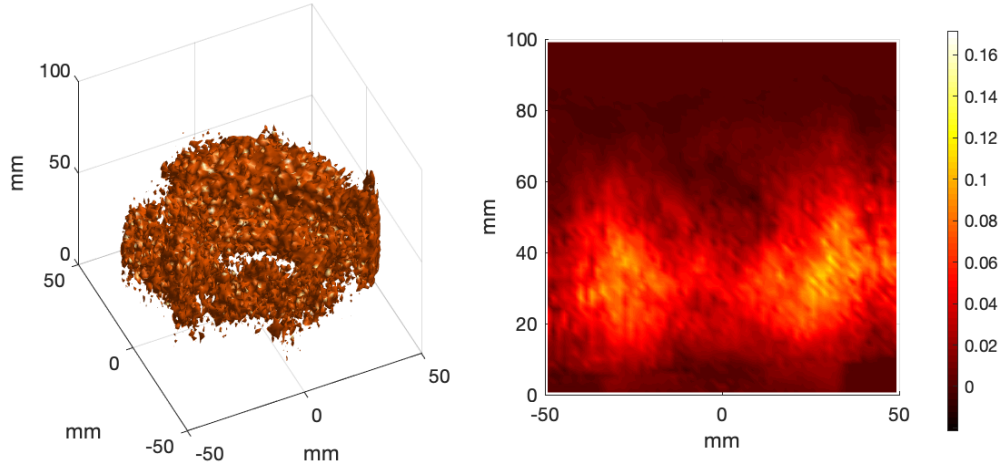

Phase 5

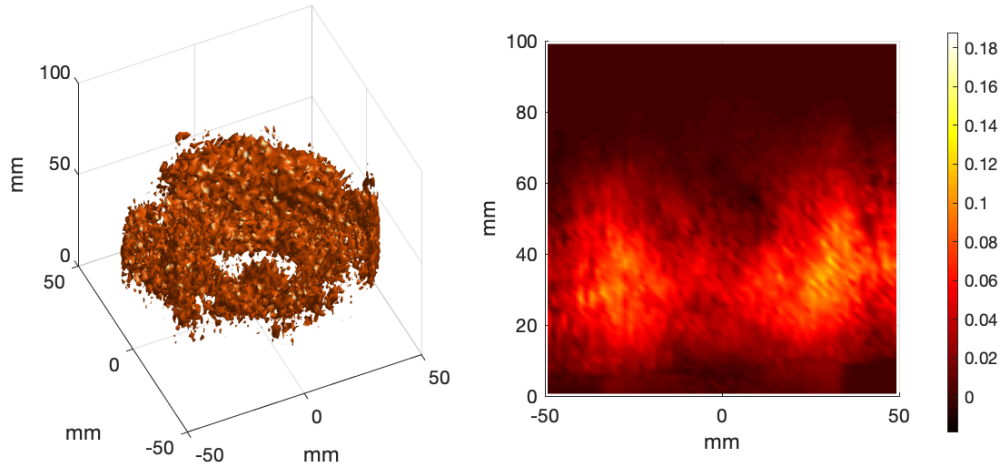

Phase 6

Figure 25. 3D Isosurface of 40% max volumetric value (left) and XY planar contour slice (right) of OH intensities for phases 4-6.*

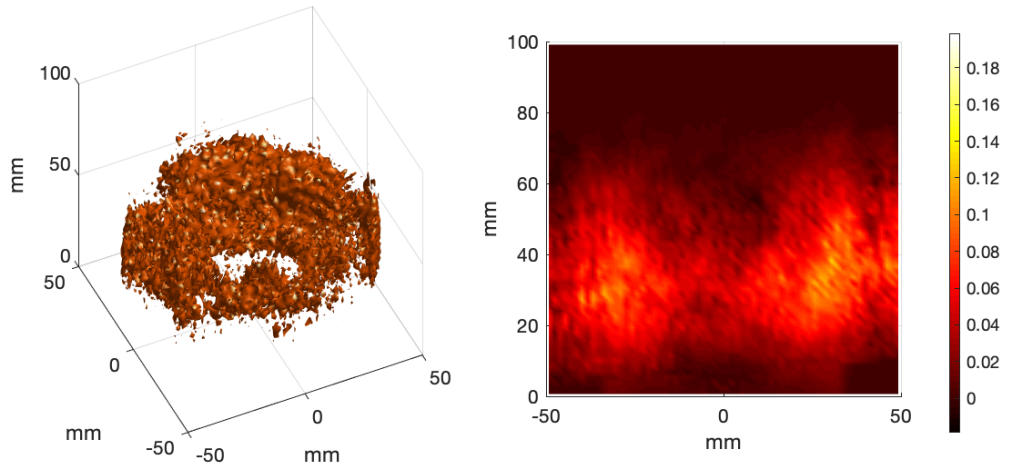

Phase 7

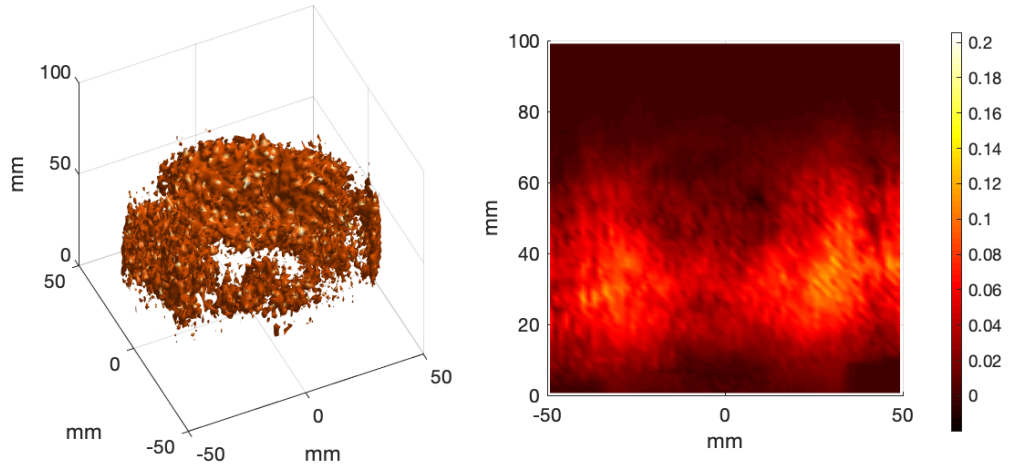

Phase 8

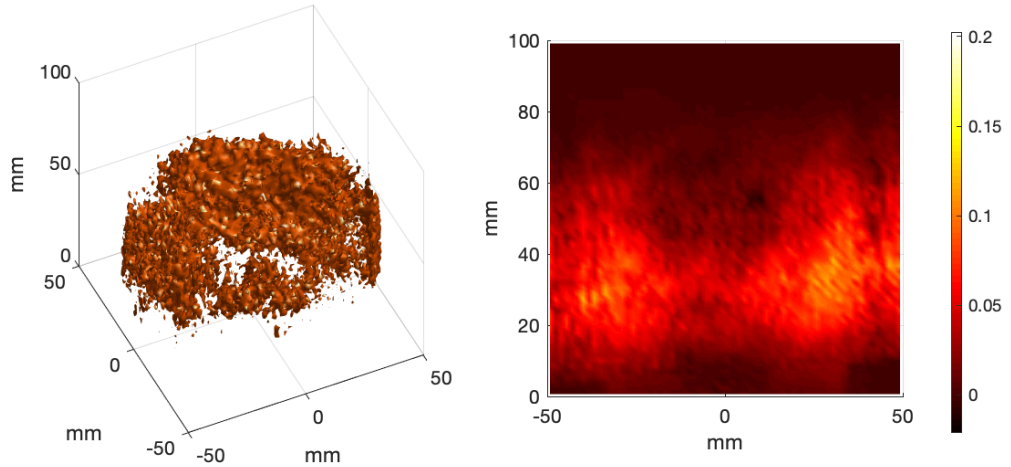

Phase 9

Figure 26. 3D Isosurface of 40% max volumetric value (left) and XY planar contour slice (right) of OH intensities for phases 7-9.*

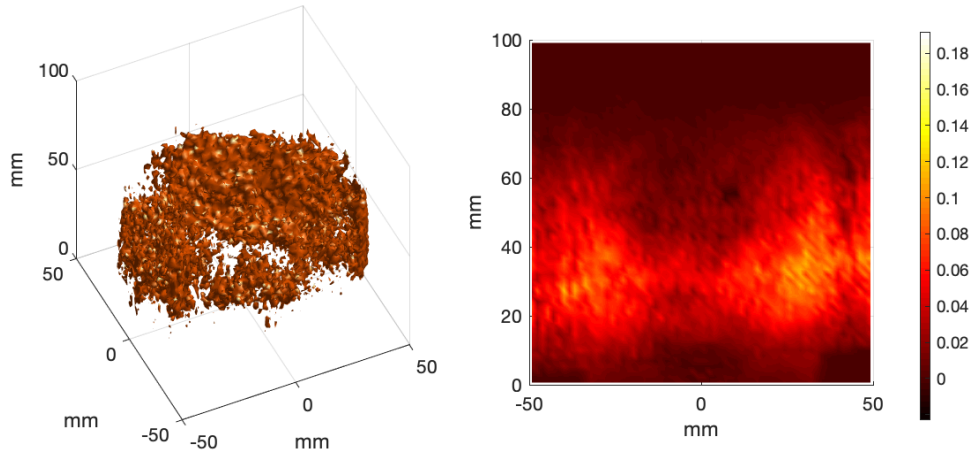

Phase 10

Figure 27. 3D Isosurface of 40% max volumetric value (left) and XY planar contour slice (right) of OH intensities for phase 10.*

The voxel count of 64^3 voxels is shown to provide sufficient resolution in the species reconstructions; a greater number of voxels would allow for higher resolution reconstructions and is recommended for further exploration in future work (Chapter 6). The intensity levels of the captured images were slightly lower than anticipated, possibly due to poor lighting in the test cell area; while not a significant issue in the reconstruction results thanks to intensity normalization, non-normalized low intensity measurements are capable of slightly affecting resolution of a reconstruction. The acoustically driven instability was forcefully excited at a frequency of 250 Hz and was shown to effectively oscillate the flame. The instability, while present, was not as strongly represented in the reconstructions as anticipated, and future work will investigate self-excited instabilities with peak pressure oscillations significantly higher than the forced instability case.

5.4 Addressing Reconstruction Noise

Upon review of the reconstruction results, there was a noticeable presence of noise found surrounding the outside of the quartz cylinder in the reconstructions (Figure 28).

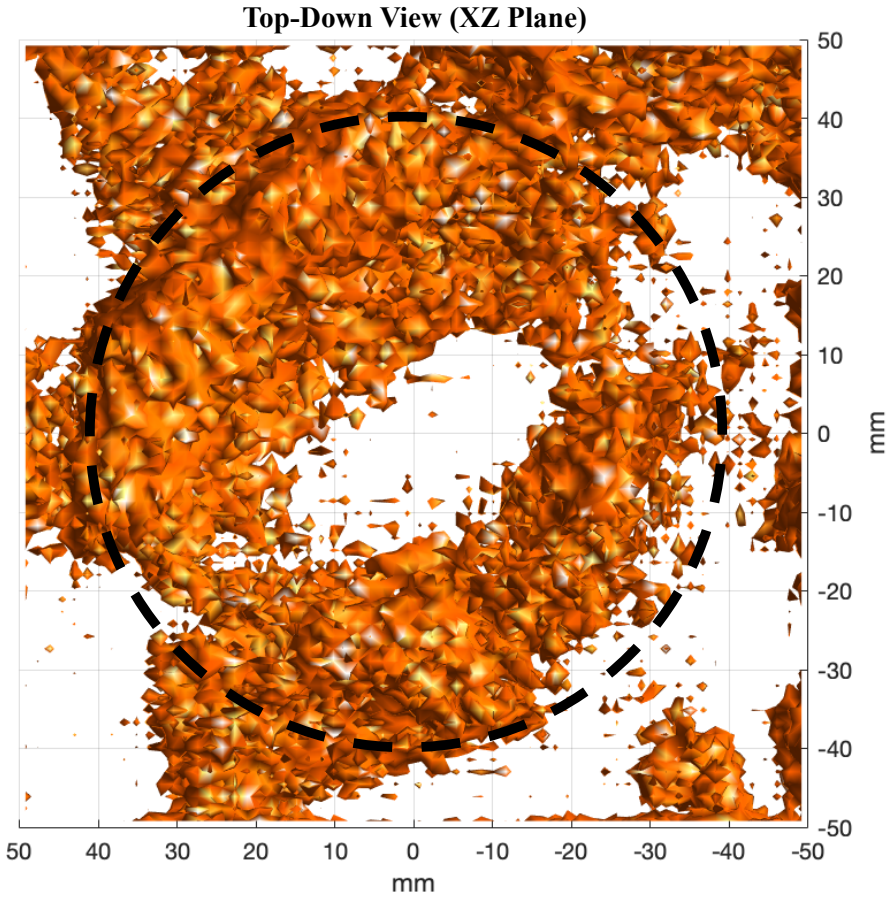

Figure 28. Top-down view of CH Phase 1 reconstruction, dotted line representing the inner quartz wall. Values lying outside of this region were considered noise in this work.*

To determine where this noise originated, an understanding of the relationship between the blurry circle center locations on the sensor and voxel locations in 3D space was first established. Because the camera is constrained to capturing a 3D spatial domain in 2D images, the blurry circles located on the sensor must account for the space in front of and behind the quartz region.

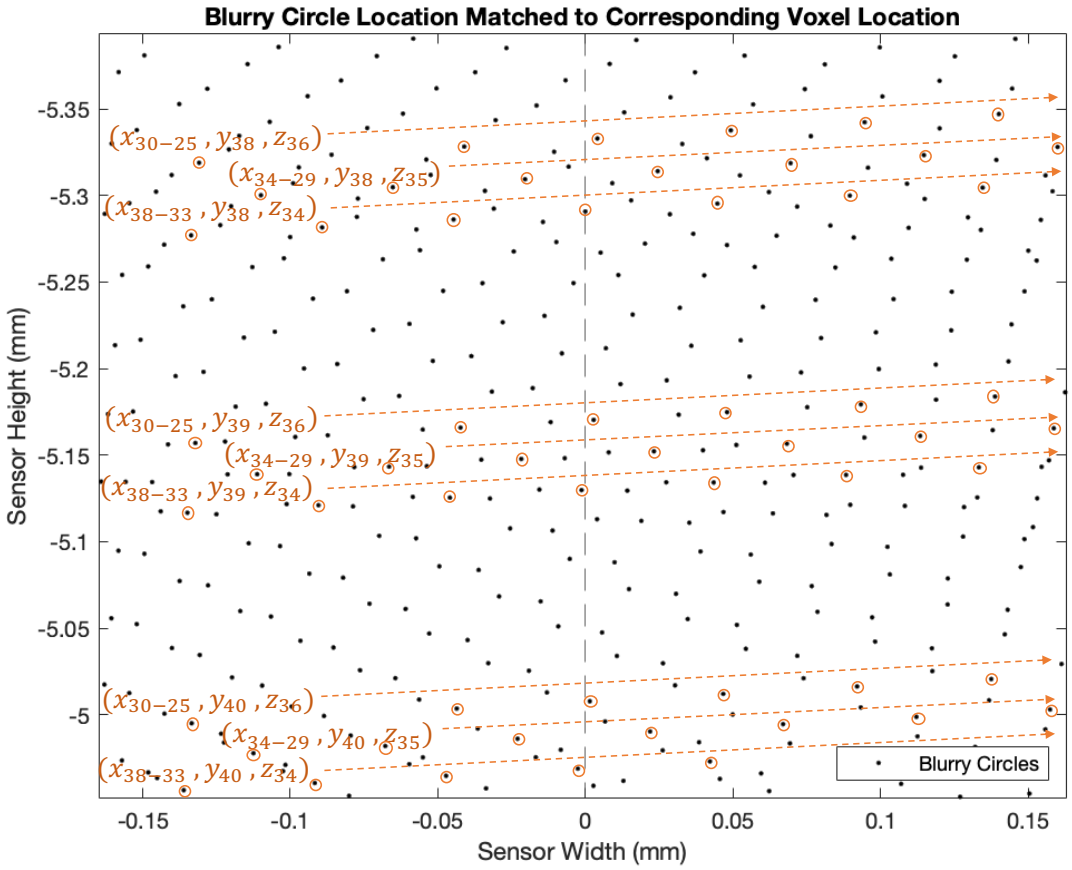

Figure 29. Voxel location coordinates (x_v, y_v, z_v) to each corresponding blurry circle center location, where v is voxel number 1-64.

As seen in Figure 29, the camera accomplishes this by cataloguing each 3D voxel point using a unique stacking pattern; x and z coordinates are shown to progress going left to right and top to bottom, respectively, while each diagonal pattern contains a single unique y coordinate. This is repeated for every single voxel coordinate location, with the diagonal patterns incrementally shifted from each other in order to fit all of the points onto the sensor. If the calibration inputs were to somewhat differ from the physically accurate camera calibration parameters, the blurry circle patterns have the potential to overlap, causing blurry circles intended for the inner quartz region to be assigned to the outside of the quartz upon reconstruction.

To confirm this, an attempt to map the locations of the blurry circles on the sensor plane was conducted using the calculated calibration parameters as inputs. The resulting blurry circles were plotted for both the areas inside and outside the quartz cylinder, and a magnified portion of the sensor's central axis is shown in Figure 30 below.

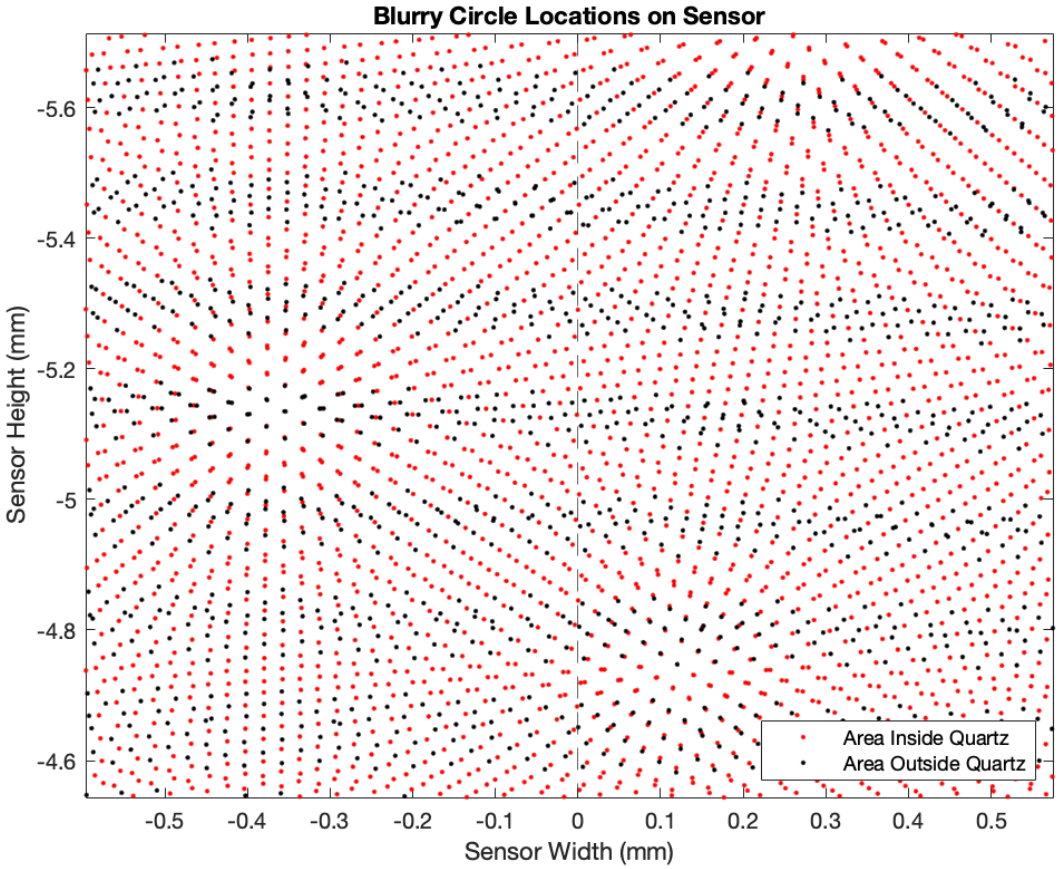

Figure 30. Sensor locations of blurry circle centers for voxels located inside and outside the quartz cylinder.

As can be shown near sensor coordinates $(-0.4, -5.2)$ and $(0.1, -4.7)$, the blurry circles for voxels located outside the quartz were found to overtake blurry circles for voxels located inside the quartz. This means that due to a slight deviation in the calibration inputs, small pockets of blurry circles throughout the sensor began to super-impose upon each other. This overlap in blurry circle patterns ultimately resulted in some of the intensities inside the flame region to be

mistaken for values outside the flame region, and values inside the quartz were reconstructed as voxel values outside the intended flame region. Under this consideration, it was concluded that the volumetric noise seen in the flame reconstructions was due to small errors in the calculated rotation and translation matrix parameters, causing unintended volumetric values to be reconstructed outside the quartz.

After conducting an extensive review of the reconstruction algorithm and calibration process, the source of these slight deviations was found to be due to three possible sources: inaccurate tolerances in the 3D printed calibration cylinder, an insufficient number of calibration points used in calculating the approximated calibration parameters, and the calibration images having been taken during a separate session in the lab prior to the actual data measurements (a potential for human error marking and relocating the camera). Future work will look to acquire calibration and experimental images together during the same session so as to avoid possible error. For the calibration process, a least squares method was used to determine the calibration parameters for the weighted ratio factors involved in the final tomographic reconstruction. When calculating a least squares solution, the more points that are utilized in calibrating the camera, the more precise the solution for the camera calibration will be. In this study, a total of 39 calibration points were designed and implemented using the custom-built calibration cylinder (Figure 6). Due to the nature of the calibration cylinder geometry, however, each camera viewing angle was only able to capture roughly 16 to 17 points from the calibration cylinder. This quantity was initially thought to be sufficient in solving for the calibration parameters; upon further analysis of the reconstruction results and the calibration technique used, it was determined that a greater number of calibration points would likely lower the presence of noise in the reconstructions along with a more accurately manufactured calibration cylinder geometry. Due to the

extenuating circumstances regarding the COVID-19 situation disallowing non-essential laboratory testing, it is the goal of future work to develop a more robust calibration plate manufactured with a greater number of calibration points and tighter tolerances. This will significantly decrease the level of noise in the resulting solution, allowing for a more accurate reconstruction to be obtained.

5.5 Spatial Equivalence Ratio Measurements

Upon extracting data values inside the quartz region, spatial equivalence ratio measurements were obtained from the ratio of the OH*/CH* reconstructed volumetric values. The dependence of the OH*/CH* intensity ratio on equivalence ratio is approximated using the curve fit relationship defined in Hardalupas et al. [12],

$$\frac{OH^*}{CH^*} = 0.497 + 2.107 * e^{-\frac{(\phi - 0.7)}{0.260}} \tag{39}$$

with ϕ representing the equivalence ratio. According to the study, this relation corresponds to a specific calibration for strain rate associated with an area-averaged gas velocity at the jet exit of $V_0 = 3\ m/s$. For a given value of equivalence ratio of $\phi \leq 1.0$, the ratio of intensities for all flow conditions was found to have an uncertainty of 5% or .05 of the value given by equation 39, while equivalence ratios ranging $\phi > 1.0$ had uncertainties of .2 up to $\phi \leq 1.3$ [12]. This relation was shown to be valid within the equivalence ratio range of $\phi > .7$ and $\phi < 1.3$ given the mixture composition approaching extinction limits at these values [12]. The technique was also shown to present smaller uncertainties for lean stoichiometric flames as opposed to rich flames [12]. In this work, collected chemiluminescence emissions for OH* and CH* provide spatial representation of the local flame fuel-air ratio, with the flame shape distinctly outlined in Figures 31-34 below.

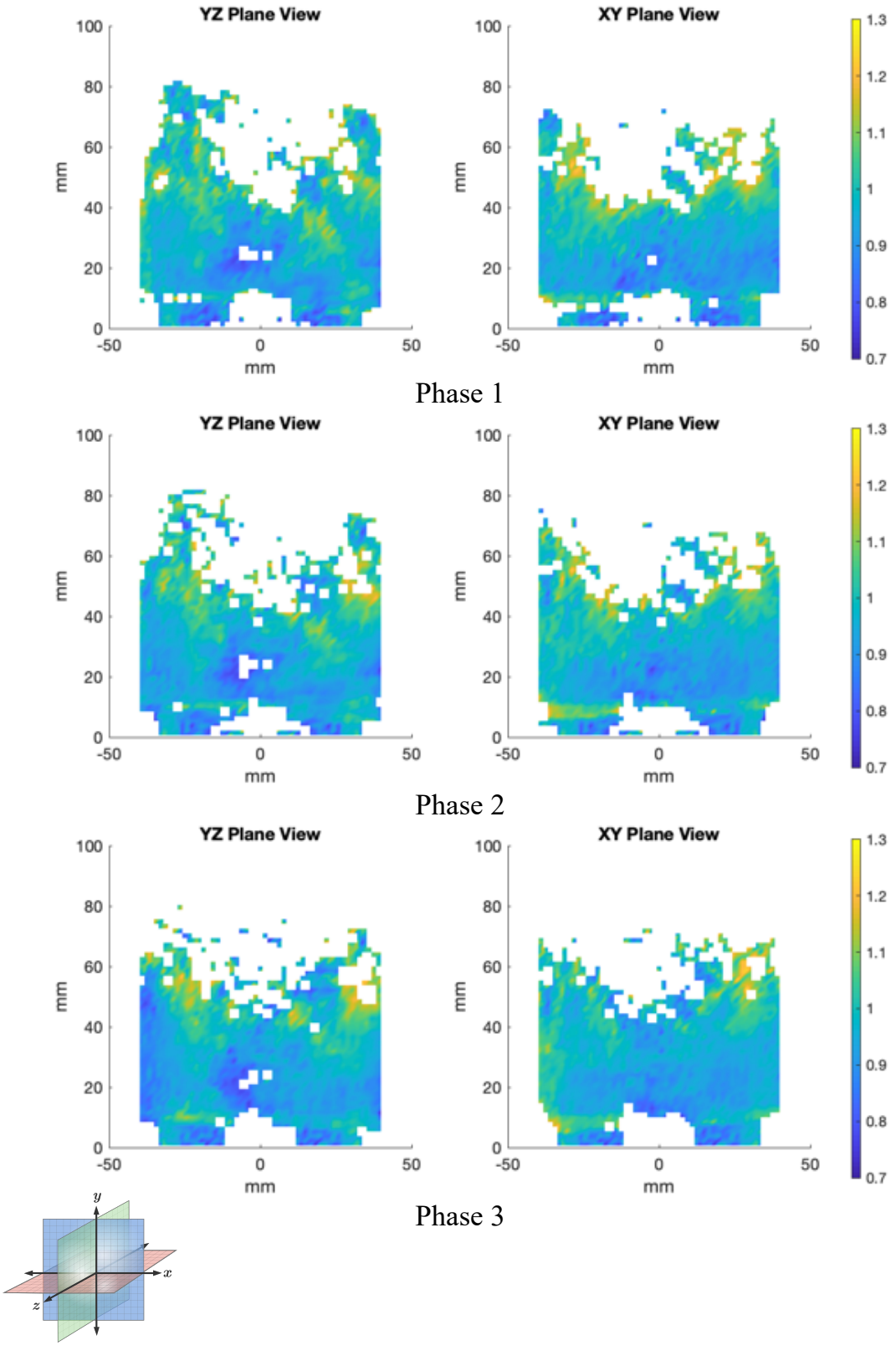

Figure 31. Equivalence ratio heat maps for Phases 1-3.

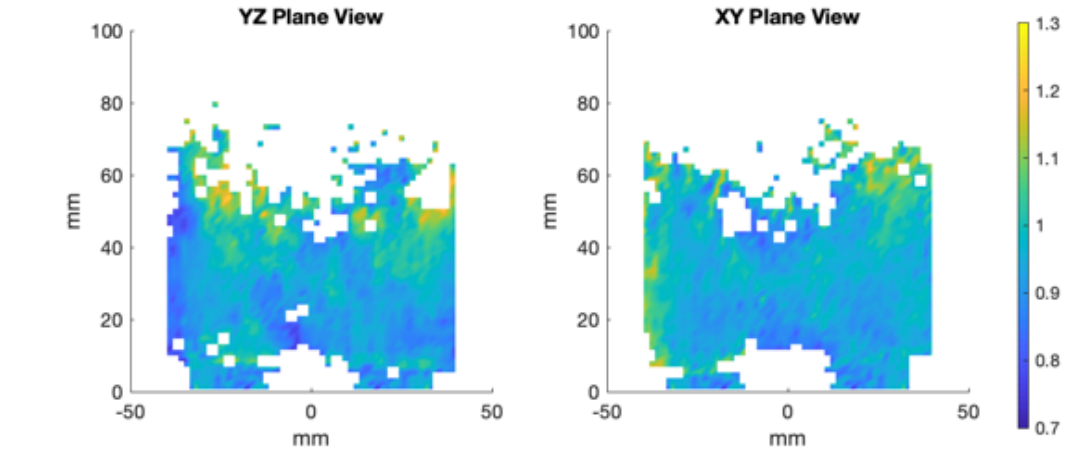

Phase 4

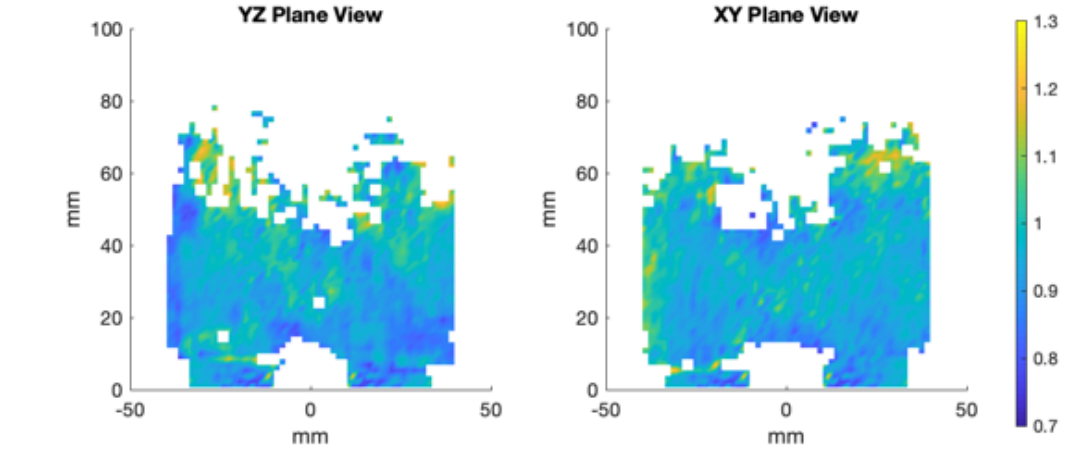

Phase 5

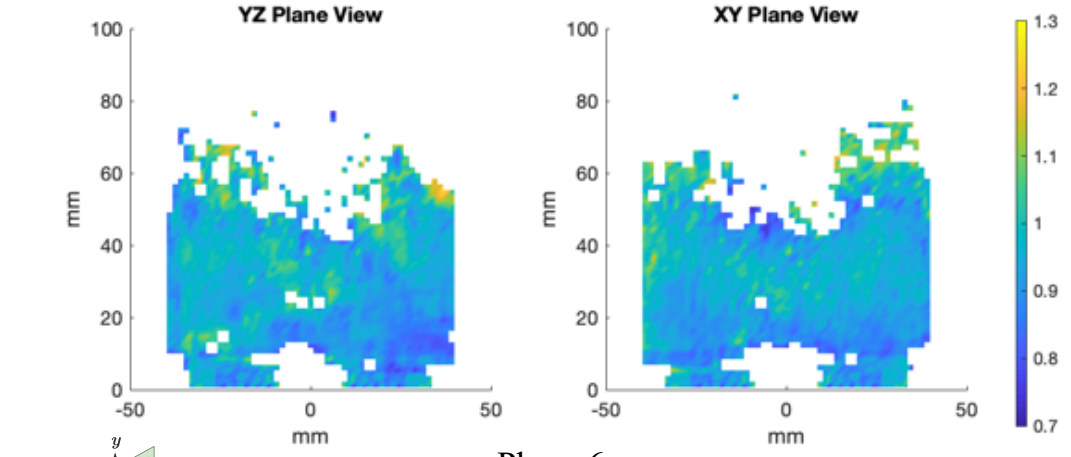

Phase 6

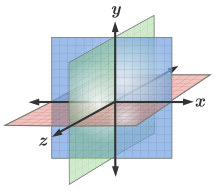

Figure 32. Equivalence ratio heat maps for Phases 4-6.

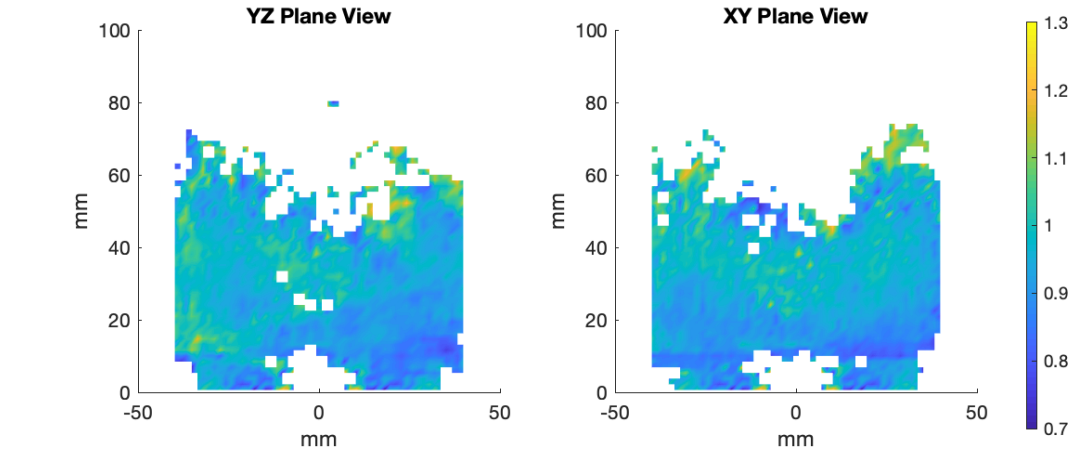

Phase 7

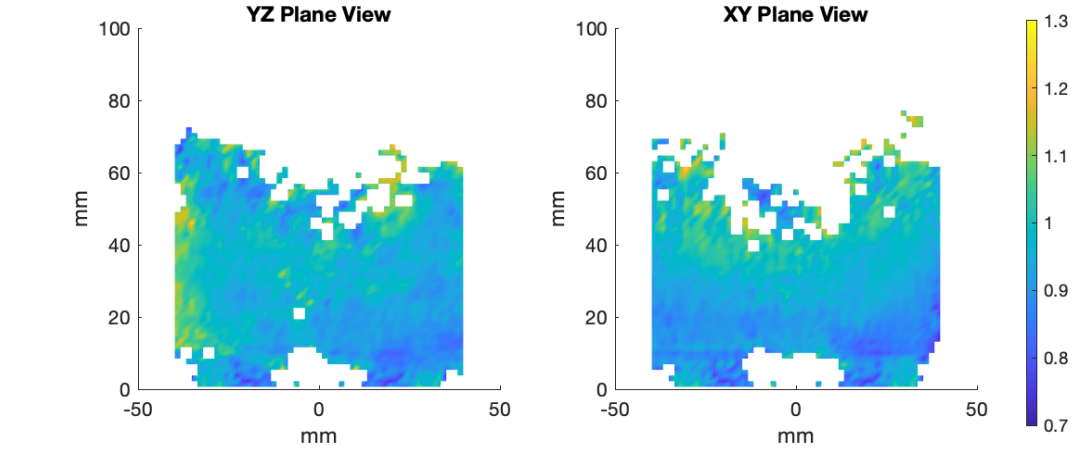

Phase 8

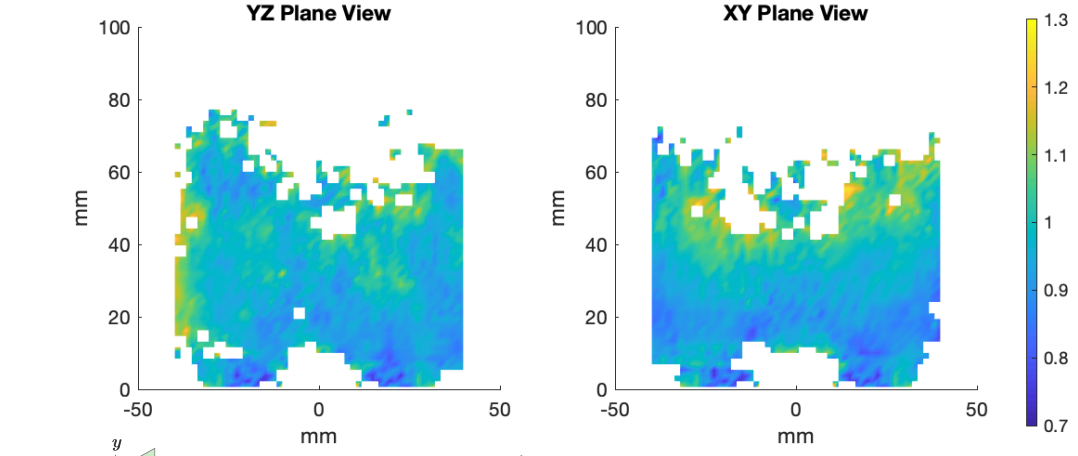

Phase 9

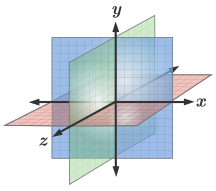

Figure 33. Equivalence ratio heat maps for Phases 7-9.

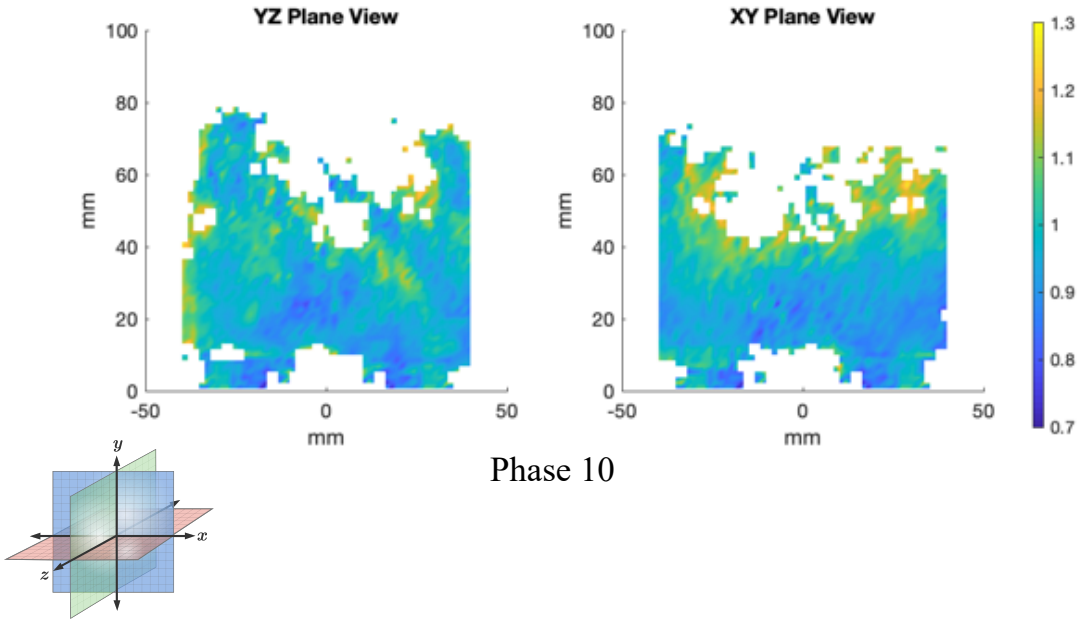

Phase 10

Figure 34. Equivalence ratio heat map for Phase 10.

For each phase, the mean equivalence ratio across all voxels in the bounds of the quartz cylinder and $y_w \leq 80\ mm$ can be shown to outline the acoustic instability wave as illustrated in Figure 35. This shows the effective oscillatory behavior caused by the forced acoustic excitation, further demonstrating the fluctuations in equivalence ratio across the turbulent flame. Also shown in Figure 35, the fluctuating equivalence ratio is found to be very close to being in phase with the phase-averaged acoustic pressure data, positioned roughly 180 μs out of phase given the location of the two wave troughs. While not perfectly in phase most likely due to pressure disturbances in the mixing tube causing fuel-air oscillations to affect the flame, the phase relationship can be clearly outlined in the oscillatory nature of both flame properties.

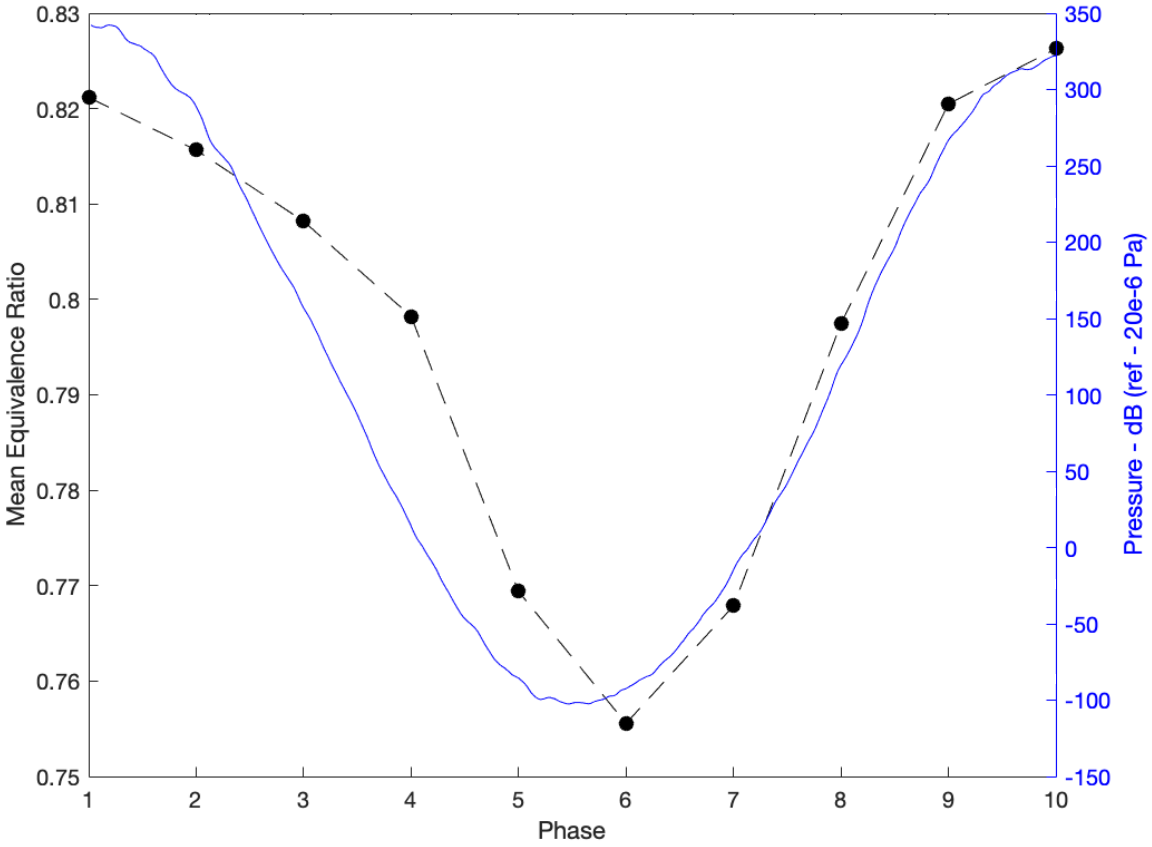

Figure 35. Acoustic instability wave shown in both spatially averaged equivalence ratio and phase-averaged pressure for phases 1-10.

Chemiluminescence intensity measurements of particular radical species have been shown as acceptable indicators of flame heat release when coupled with simultaneous flame velocity measurements [12, 13, 41, 62], and it is the goal of future studies to conduct temporal velocity and intensity measurements to acquire spatially resolved heat release rates for an acoustically excited flame.

Chapter 6: Conclusions

Computed Tomography of Chemiluminescence has seen significant utilization for mapping spatially resolved flame measurements throughout a number of different studies [16, 22, 26, 47, 53, 54, 58]. In this work, a tomographic reconstruction program was developed and tested using chemiluminescence emissions to predict and study equivalence ratio fluctuations in an acoustically excited flame. Utilizing a multiplicative algebraic algorithm along with high resolution camera images collected at various projection angles, reconstructed intensity fields were acquired for both CH* and OH* radical species and were used to map spatial equivalence ratios. Results for both equivalence ratio and pressure fluctuations were found to be very close to in phase with each other, signifying the coupled interconnection between acoustic pressure oscillations and equivalence ratio behavior in thermoacoustic phenomena. The camera positioning was calibrated using a developed method of calibration [36] and a custom built calibration cylinder to properly align and compute locations of the camera. Visible noise was noticed outside of the flame region, and it was determined that a greater number of calibration points and tighter manufacturing tolerances must be implemented to fully calibrate the camera and avoid propagating reconstruction noise outside of the flame region.

Future work will aim to improve upon the calibration cylinder design and increase the number of visible calibration points to improve overall reconstruction accuracy and eliminate unwanted noise. Further analysis will also be conducted on the presence and variation of heat release rate utilizing measurements in Particle Image Velocimetry (PIV) [63] to further expand combustion measurement capability. Further investigation might also prove insightful in increasing the number of camera angles used in acquiring projections and varying the number of voxels used in mapping the volumetric flame.

Bibliography

[1] L. Crocco and S. Cheng, *Combustion Instability in Liquid Propellant Rocket Motors*. 1956.

[2] D. Nowak, V. Bellucci, J. Cerny, and G. Engelbrecht, "Numerical Modeling of Thermoacoustic Oscillations in a Gas Turbine Combustion Chamber," presented at the Volume 1: Combustion and Fuels, Education, 2006.

[3] B. D. Mugridge, "Combustion Driven Oscillations," *Journal of Sound and Vibration,* vol. 70, no. 3, pp. 437-452, 1980.

[4] C. E. Mitchell, L. Crocco, and W. A. Sirignano, "Nonlinear Longitudinal Instability in Rocket Motors with Concentrated Combustion," *Combustion Science and Technology,* vol. 1, no. 1, pp. 35-64, 1969, doi: 10.1080/00102206908952190.

[5] J. W. S. B. Rayleigh, *The Theory of Sound* (no. v. 2). Macmillan, 1894.

[6] M. Huth and A. Heilos, "Fuel Flexibility in Gas Turbine Systems: Impact on Burner Design and Performance," *Woodhead Publishing Series in Energy,* pp. 635-684, 2013.

[7] J. J. Keller, "Thermoacoustic oscillations in combustion chambers of gas turbines," *AIAA Journal,* vol. 33, no. 12, pp. 2280-2287, 1995, doi: 10.2514/3.12980.

[8] V. Nori and J. Seitzman, "Evaluation of Chemiluminescence as a Combustion Diagnostic Under Varying Operating Conditions," presented at the 46th AIAA Aerospace Sciences Meeting and Exhibit, 2008.

[9] J. Floyd and A. M. Kempf, "Computed Tomography of Chemiluminescence (CTC): High resolution and instantaneous 3-D measurements of a Matrix burner," *Proceedings of the Combustion Institute,* vol. 33, no. 1, pp. 751-758, 2011, doi: 10.1016/j.proci.2010.06.015.

[10] M. M. Tripathi, Krishnan, Sundar R., Srinivasan, Kalyan K., "Chemiluminescence-based multivariate sensing of local equivalence ratios in premixed atmospheric methane-air flames," *Mississippi State University*.

[11] S. Kim, C. Lee, and M. Kwon, "Measurement of Equivalence Ratio Using Optical Flame Chemiluminescence Sensor of Turbulent Diffusion Flame," *International Journal of Electrical Energy,* vol. 3, no. 3, 2015, doi: 10.18178/ijoee.3.3.203-208.

[12] Y. Hardalupas and M. Orain, "Local measurements of the time-dependent heat release rate and equivalence ratio using chemiluminescent emission from a flame," *Combustion and Flame,* vol. 139, no. 3, pp. 188-207, 2004, doi: 10.1016/j.combustflame.2004.08.003.

[13] Y. Hardalupas, C. S. Panoutsos, G. Skevis, and A. M. K. P. Taylor, "Numerical Evaluation of Equivalence Ratio Measurement Using OH* and CH* Chemiluminescence in Premixed Iso-Octane/Air Flames," in *European Combustion Meeting*, 2005.

[14] Shreekrishna, V. Acharya, and T. Lieuwen, "Flame response to equivalence ratio fluctuations - relationship between chemiluminescence and heat release," *International Journal of Spray and Combustion Dynamics,* vol. 5, no. 4, 2013.

[15] J. Guen Lee, K. Kim, and D. A. Santavicca, "Measurement of equivalence ratio fluctuation and its effect on heat release during unstable combustion," *Proceedings of the Combustion Institute,* vol. 28, no. 1, pp. 415-421, 2000.

[16] B. D. Geraedts, S. Yang, M. G. Adams, C. M. Arndt, and A. M. Steinberg, "Tomographic Reconstruction of Thermoacoustic Energy Transfer Patterns in Swirl-Stabilized Flames with Helical Vortex Cores Using OH* Chemiluminescence," presented at the Mediterranean Combustion Symposium, Rhodes, Greece, 2015.

[17] J. Floyd, "Computed Tomography of Chemiluminescence: A 3D Time Resolved Sensor for Turbulent Combustion," Mechanical Engineering Department, Imperial College London, 2009.

[18] J. Floyd, P. Geipel, and A. M. Kempf, "Computed Tomography of Chemiluminescence (CTC): Instantaneous 3D measurements and Phantom studies of a turbulent opposed jet flame," *Combustion and Flame,* vol. 158, no. 2, pp. 376-391, 2011, doi: 10.1016/j.combustflame.2010.09.006.

[19] R. Gordon, R. Bender, and G. T. Herman, "Algebraic Reconstruction Techniques (ART) for Three-Dimensional Electron Microscopy and X-Ray Photography," *Journal of Theoretical Biology,* vol. 29, pp. 471-481, 1970.

[20] V. N. Nori and J. M. Seitzman, "CH* chemiluminescence modeling for combustion diagnostics," *Proceedings of the Combustion Institute,* vol. 32, no. 1, pp. 895-903, 2009, doi: 10.1016/j.proci.2008.05.050.

[21] B. D. Geraedts, "Development of Rayleigh Index Measurement Techniques for Swirl-Stabilized Lean Premixed Combustion," Doctorate, Aerospace Engineering Department, University of Toronto, 2015.

[22] B. D. Geraedts, C. M. Arndt, and A. M. Steinberg, "Rayleigh Index Fields in Helically Perturbed Swirl-Stabilized Flames Using Doubly Phase Conditioned OH* Chemiluminescence Tomography," *Flow, Turbulence and Combustion,* vol. 96, no. 4, pp. 1023-1038, 2016, doi: 10.1007/s10494-016-9727-4.

[23] J. De Rosier and A. Klug, "Reconstruction of Three Dimensional Structures from Electron Micrographs," *Nature,* vol. 217, 1968.

[24] D. Verhoeven, "Limited-data computed tomography algorithms for the physical sciences," *Applied Optics,* vol. 32, no. 20, pp. 3736-3754, 1993.

[25] C. Badea and R. Gordon, "Experiments with the nonlinear and chaotic behaviour of the multiplicative algebraic reconstruction technique (MART) algorithm for computed tomography," *Phys Med Biol,* vol. 49, no. 8, pp. 1455-74, Apr 21 2004, doi: 10.1088/0031-9155/49/8/006.

[26] D. Mishra, J. P. Longtin, R. P. Singh, and V. Prasad, "Performance Evaluation of Iterative Tomography Algorithms for Incomplete Projection Data," *Applied Optics,* vol. 43, no. 7, pp. 1522-1532, 2004.

[27] J. L. Edwards, "Proper Orthogonal Decomposition of Tomographic Analysis for Combustion and Control Applications," Cornell University, 2007.

[28] S. Matej and R. Lewitt, "Practical Considerations for 3-D Image Reconstruction using Spherically Symmetric Volume Elements," *IEEE Transactions on Medical Imaging,* vol. 15, no. 1, pp. 68-78, 1996.

[29] H. S. Ko* and K. D. Kihm, "An extended algebraic reconstruction technique (ART) for density-gradient projections: laser speckle photographic tomography," *Experiments in Fluids,* vol. 27, no. 6, pp. 542-550, 1999/11/01 1999, doi: 10.1007/s003480050378.

[30] W. van Aarle *et al.*, "The ASTRA Toolbox: A platform for advanced algorithm development in electron tomography," *Ultramicroscopy,* vol. 157, pp. 35-47, Oct 2015, doi: 10.1016/j.ultramic.2015.05.002.

[31] R. Y. Tsai, "A Versatile Camera Calibration Technique for High-Accuracy 3D Machine Vision Metrology Using Off-the Shelf TV Cameras and Lenses," *Journal of Robotics and Automation,* 1987.

[32] Z. Zhang, "A Flexible New Technique for Camera Calibration," *IEEE Transactions on Pattern Analysis and Machine Intelligence,* vol. 22, no. 11, 2000.

[33] F. Remondino and C. Fraser, "Digital Camera Calibration Methods: Considerations and Comparisons," *ISPRS Commission V Symposium 'Image Engineering and Vision Metrology',* 2006.

[34] M. Kang, Y. Wu, and L. Ma, "Fiber-based endoscopes for 3D combustion measurements: View registration and spatial resolution," *Combustion and Flame,* vol. 161, no. 12, pp. 3063-3072, 2014, doi: 10.1016/j.combustflame.2014.06.002.

[35] Q. Lei, Y. Wu, H. Xiao, and L. Ma, "Analysis of four-dimensional Mie imaging using fiber-based endoscopes," *Appl Opt,* vol. 53, no. 28, pp. 6389-98, Oct 1 2014, doi: 10.1364/AO.53.006389.

[36] J. Wang, Y. Song, Z. H. Li, A. Kempf, and A. Z. He, "Multi-directional 3D flame chemiluminescence tomography based on lens imaging," *Opt Lett,* vol. 40, no. 7, pp. 1231-4, Apr 1 2015, doi: 10.1364/OL.40.001231.

[37] J. J. Keller, "Non-Linear Self Excited Acoustic Oscillations in Cavities," *Journal of Sound and Vibration,* vol. 94, no. 3, pp. 397-409, 1984.

[38] J. J. Keller, "Nonlinear self-excited acoustic oscillations within fixed boundaries," *Journal of Fluid Mechanics,* vol. 123, pp. 267-281, 1982

, doi: 10.1017/s002211208200305x.

[39] J. J. Keller, "Thermally Induced Low-Frequency Oscillations," *Journal of Applied Mathematics and Physics (ZAMP),* vol. 36, 1985.

[40] W. Krebs, P. Flohr, B. Prade, and S. Hoffmann, "Thermoacoustic Instability Chart for High-Intensity Gas Turbine Combustion Systems," *Combustion Science and Technology,* vol. 174, no. 7, pp. 99-128, 2002, doi: 10.1080/00102200290021209.

[41] J. O'Connor, V. Acharya, and T. Lieuwen, "Transverse combustion instabilities: Acoustic, fluid mechanic, and flame processes," *Progress in Energy and Combustion Science,* vol. 49, pp. 1-39, 2015, doi: 10.1016/j.pecs.2015.01.001.

[42] X. Huang and W. Baumann, "Reduced-Order Modeling of Dynamic Heat Release for Thermoacoustic Instability Prediction," *Combustion Science and Technology,* vol. 179, no. 3, pp. 617-636, 2007.

[43] M. Murugesan, B. Singaravelu, A. K. Kushwaha, and S. Mariappan, "Onset of flame-intrinsic thermoacoustic instabilities in partially premixed turbulent combustors," *International Journal of Spray and Combustion Dynamics,* vol. 10, no. 3, pp. 171-184, 2018, doi: 10.1177/1756827718758511.

[44] M. Hoeijmakers, V. N. Kornilov, I. L. Arteaga, and P. Goey, "Intrinsic Instability of Flame-Acoustic Coupling," *Combustion and Flame,* vol. 161, no. 11, 2014.

[45] T. Emmert, S. Bomberg, and W. Polifke, "Intrinsic Thermoacoustic Instability of Premixed Flames," *Combustion and Flame,* vol. 162, no. 1, pp. 75-85, 2014.

[46] S. Sardeshmukh, M. Bedard, and W. Anderson, "The use of OH* and CH* as heat release markers in combustion dynamics," *International Journal of Spray and Combustion Dynamics,* vol. 9, no. 4, pp. 409-423, 2017, doi: 10.1177/1756827717718483.

[47] H. M. Hertz and G. W. Faris, "Emission Tomography of Flame Radicals," *Optics Letters,* vol. 13, no. 5, pp. 351-353, 1988.

[48] B. Böhm, C. Kittler, A. Nauert, and A. Dreizler, "Diagnostics at High Repetition Rates: New Insights into Transient Combustion Phenomena," in *European Combustion Meeting*, 2007: Citeseer.

[49] T. S. Cheng, C. Y. Wu, Y. H. Li, and Y. C. Chao, "Chemiluminescence Measurements of Local Equivalence Ratio in a Partially Premixed Flame," *Combustion Science and Technology,* vol. 178, no. 10-11, pp. 1821-1841, 2006, doi: 10.1080/00102200600790755.

[50] N. Docquier, F. Lacas, and S. Candel, "Closed-Loop Equivalence Ratio Control of Premixed Combustors using Spectrally Resolved Chemiluminescence Measurements," *Proceedings of the Combustion Institute,* vol. 29, pp. 139-145, 2002.

[51] C. N. Markides, G. De Paola, and E. Mastorakos, "Measurements and simulations of mixing and autoignition of an n-heptane plume in a turbulent flow of heated air," *Experimental Thermal and Fluid Science,* vol. 31, no. 5, pp. 393-401, 2007, doi: 10.1016/j.expthermflusci.2006.04.008.

[52] K. T. L. Walsh, M.B.; Tanoff, M.A.; Smooke, M.D., "Experimental and Computational Study of CH, CH*, and OH* in an Axisymmetric Laminar Diffusion Flame," presented at the Twenty-Seventh Symposium (International) on Combustion/The Combustion Institute, 1998.

[53] A. Schwarz, "Multi-Tomographic Flame Analysis with a Schlieren Apparatus," *Measurement Science and Technology,* no. 7, pp. 406-413, 1995.

[54] M. N. Asl and A. Sadremomtaz, "Analytical image reconstruction methods in emission tomography," *Journal of Biomedical Science and Engineering,* vol. 06, no. 01, pp. 100-107, 2013, doi: 10.4236/jbise.2013.61013.

[55] J. Beatty, "The Radon Transform and the Mathematics of Medical Imaging," Honors Department, Colby College, 2012.

[56] D. Verhoeven, "Multiplicative Algebraic Computed Tomographic Reconstruction Algorithms for the Reconstruction of Multidirectional Interferometric Data," *Optical Engineering,* 1993.

[57] R. Gordon, "A tutorial on art (algebraic reconstruction techniques)," *IEEE Transactions on Nuclear Science,* vol. 21, no. 3, pp. 78-93, 1974, doi: 10.1109/tns.1974.6499238.

[58] D. Mishra, M. K., and M. P., "A Robust MART Algorithm for Tomographic Applications," *Numerical Heat Transfer, Part B: Fundamentals,* vol. 35, no. 4, pp. 485-506, 1999/06/01 1999, doi: 10.1080/104077999275857.

[59] E. Weisstein. "Euler Angles." Wolfram Research. https://mathworld.wolfram.com/EulerAngles.html

[60] A. C. Kak and M. Slaney, *Principles of Computerized Tomographic Imaging*. IEEE Press, 1988.

[61] V. Dribinski, A. Ossadtchi, V. A. Mandelshtam, and H. Reisler, "Reconstruction of Abel-transformable images: The Gaussian basis-set expansion Abel transform method," *Review of Scientific Instruments,* vol. 73, no. 7, pp. 2634-2642, 2002, doi: 10.1063/1.1482156.

[62] P. G. Aleiferis, Y. Hardalupas, A. M. K. P. Taylor, K. Ishii, and Y. Urata, "Flame chemiluminescence studies of cyclic combustion variations and air-to-fuel ratio of the reacting mixture in a lean-burn stratified-charge spark-ignition engine," *Combustion and Flame,* vol. 136, no. 1-2, pp. 72-90, 2004, doi: 10.1016/j.combustflame.2003.09.004.

[63] F. Chen and H. Liu, "Particle Image Velocimetry for Combustion Measurements: Applications and Developments," *Chinese Journal of Aeronautics,* vol. 31, no. 7, pp. 1407-1427, 2018.

Appendix A: Reconstruction Algorithm

```
%Final Flame Iterative Reconstruction Code
%Created by: Joseph Giroux
%Last Updated: 5/25/2020

clear all
clc
close all

tic

%Shift Image/Volume by:
shift=1;
%Choose Image Phase to Reconstruct
P=1; %of 10
%Number of Voxels
V=64;
%Number of Pixels
X=1024;
%Relaxation Factor
B=.85;
%Size of Cube Reconstruction Area
size_cube=100; %mm

%Load Abel-Inversion Guess Data (Change CH or OH)
m=matfile('AbelInversion_InitialGuess_CH_(AllPhases_V64).mat');
Abel_guess=m.Abel_Inversion_array(P,:).*(1e2);
f_h=Abel_guess+shift;

%Load in Big Weight Ratio File (Change variable based on Voxel count)
load(['C:\Users\tjgiroux3\Desktop\Final Phases Reconstruction\Weight Ratio
Files\Uncentered_100mm_FinalAttempt_WeightRatio_Big_(V',num2str(V),'_X1024_N1
1).mat'])
W=W_Big_V64;
clear W_Big_V64
%Load in Intensity Array (Change CH or OH)
load(['C:\Users\tjgiroux3\Desktop\Final Phases Reconstruction\CH Intensity
Files\FINAL_Uncentered_Normalized&Cropped_PhaseAverage_Images_CH_(Phase',num2
str(P),').mat'])
I=(I_PhaseAvg_centered)+sum(shift.*W,1);
clear I_PhaseAvg_centered

%Load in Big Relaxation Factor Term
load(['C:\Users\tjgiroux3\Desktop\Final Phases Reconstruction\Relaxation Term
Files\Uncentered_100mm_FinalAttempt_RelaxationTerm_initial_(V',num2str(V),'_X
1024_N11).mat'])
Relax_Big_Array=B.*Relax_initial;
clear Relax_initial

%Initialize f_h1 Function Array
f_h1=zeros(1,V^3);
```

```
%Iteration Marker
x=1;

while 1
%% COMPARISON INTENSITY CALCULATION
%Display Iteration Count
disp(['Iteration: ',num2str(x)])

%Progress Marker 1
disp('Beginning I_c Calculation)')
%Intensity Comparison Calculation
I_c=f_h*W;
%Intensity Comparison
C=I./I_c;
%Replace NaN and Inf values with Real Values
C(isnan(C))=1;
%C(isinf(C))=0;

%% RECONSTRUCTION CALCULATION
%Progress Marker 2
disp('Beginning Reconstruction Calculation')
%Difference Term for Intensity Comparison
dif=1-C;
f_h1=f_h.*(1-(Relax_Big_Array*dif'))';

%Save the Function Every nth Iteration
% n=100;
% if mod(x,n)==0
% i=x/n;
% Save_f_h{i}=[f_h1;f_h];
% end

%% WHILE LOOP BREAK DETERMINANT

%Convergence Criteria
E_converge(x)=max((abs(f_h1-f_h)./f_h1)*100);
E_converge(x)

%Display Loop Error
%Max Absolute Difference Error
E1(x)=max(abs(f_h1-f_h));
%E1(x)
%RMS Error
E2(x)=(sum((f_h1-f_h).^2)./(V.^3)).^.5;
%Normalized RMS Percent Error
E3(x)=(E2(x)./(max(f_h1)-min(f_h1))).*100;
%E3(x)

%Assign new f_h value for next iteration
f_h=f_h1;
f_h1=zeros(1,V^3);

%Iteration Convergence Criteria
if E_converge(x)<(1e-5)
    break
```

```
end
%Assign Next Iteration
x=x+1;
%Max Iteration Break
if x>1500000
    break
end

end
%Scale and Shift function back for ER Analysis
n=matfile('Normalization_Scale_CH.mat');
norm_scale=n.max_norm(P,:);
f_h1=norm_scale.*(f_h-shift);
%Save Function with defined Filepath
save(['Uncentered_Normalized_Shifted_Reconstructed_Function_CH_(Phase',num2st
r(P),'_V',num2str(V),')'],'f_h1','-v7.3')

%Display Time Elapsed for Total Reconstruction
t=toc;
disp(['Time Elapsed For Reconstruction: ',num2str(t/3600),'hour(s)'])

Save_Error=[E1;E2;E3;E_converge];
save(['Uncentered_Normalized_Shifted_Saved_Error_Phase',num2str(P)],'Save_Err
or','-v7.3')

%Error Plots
figure(1)
plot(E_converge)
xlabel('Iteration Number')
ylabel('Error Value')
title('Convergence Criteria c')
%ylim([0,1e-5]);

figure(2)
plot(1:(size(E1,2)),E1)
xlabel('Iteration Number')
ylabel('Error Value')
title('Plot 1: Max Absolute Difference Error')
%ylim([0,1e-6]);

figure(3)
plot(1:(size(E2,2)),E2)
xlabel('Iteration Number')
ylabel('Error Value')
title('Plot 2: RMS Error')
%ylim([0,1e-1]);

figure(4)
plot(1:(size(E3,2)),E3)
xlabel('Iteration Number')
ylabel('Error Value')
title('Plot 3: Normalized RMS Percent Error')
%ylim([0,10e-3]);
```

```
%%%%%%%%%%%%%%%%%%%%%%%%% Flame Plots %%%%%%%%%%%%%%%%%%%%%%%%%

%Voxel Centerpoint Coordinates
M=[-(V/2),0,-(V/2)];
for i=1:V
x(i)=((size_cube/V).*[M(1,1)+(i-.5)]);
y(i)=((size_cube/V).*[M(1,2)+(i-.5)]);
z(i)=((size_cube/V).*[M(1,3)+(i-.5)]);
end

%%-----Abel-Inversion Volumetric Isosurface-----%%
%Compiling of Abel-Inversion 3D Volumetric Data
Abel_Inversion3D=reshape(Abel_guess,V,V,V);
Abel_Inversion3D=permute(Abel_Inversion3D,[1,3,2]);
figure(5)
[X_w,Z_w,Y_w]=meshgrid(x,z,y);
max_val_Abel=max(max(max(Abel_Inversion3D)));
isosurface(X_w,Z_w,Y_w,Abel_Inversion3D,max_val_Abel*0.3)
colormap(bone)
colorbar
%%----------Reconstruction Isosurface-----------%%
%f_h1(isnan(f_h1))=0;
V_fh1=reshape(f_h1,V,V,V);
V_fh1=permute(V_fh1,[1,3,2]);
figure(6)
[X_w,Z_w,Y_w]=meshgrid(x,z,y);
max_val_fh1=max(max(max(V_fh1)));
isosurface(X_w,Z_w,Y_w,V_fh1,max_val_fh1.*.4)
%axis([-50 50,0 100,-50 50])
colormap(bone)
%caxis([0,.2])
colorbar
%%-----Filtered Reconstruction Isosurface-------%%
V_fh1_filt=imgaussfilt3(V_fh1);
%V_fh1_filt(isnan(V_fh1_filt))=0;
figure(7)
[X_w,Z_w,Y_w]=meshgrid(x,z,y);
max_val_fh1_filt=max(max(max(V_fh1_filt)));
isosurface(X_w,Z_w,Y_w,V_fh1_filt,max_val_fh1_filt.*.4)
axis([-50 50,-50 50,0 100])
colormap(bone)
%caxis([0,.2])
colorbar
```

Appendix B: Weight Ratio Calculation

```
%ARC Grid Submission: Real Weight Ratio Calculator
%Created by: Joseph Giroux
%Last Updated: 2/19/2020

clear all
clc

%Job Array 1

k=int32(str2num(getenv('SLURM_ARRAY_TASK_ID')));

%Notes:
%->N,V,and X values must be positive integers
%->Change N based on which camera location is being calculated
%->Change Filepath for file save as necessary
%->Some parameters specialized for V=320, Specifically j value

%->Desired length of cube to encapsulate reconstruction area
size_cube=100; %mm

%Voxel Cube Dimension (VxVxV Voxel Cube)
V=64;
%Camera Location
N=1;

%% ------Initiate Save-Loop Function (Set to run n number of times)--------

for j=4.*(k-1)+1:4.*k
    w{j}=CombARCSaveLoopFunction(V,N,size_cube,j);
    disp('iteration')
    disp(j)
end
%%


%Save Function with defined Filepath
[filepath] =
fileparts(['/work/cascades/tjgiroux3/Real_Flame_Reconstruction/',num2str(V),'
_Voxels/JobArray_',num2str(N),'/']);
save(fullfile(filepath,sprintf('w_FinalAttempt_%d',k)),'w','-v7.3')
```

```
%ARC Grid Submission: Combined Save Cycle Function
%Created by: Joseph Giroux
%Last Updated: 2/19/2020

function w=CombARCSaveLoopFunction(V,N,size_cube,j)
%Increment Index for Desired Calculated Voxel Centerpoints
Index_i=((V.^3)./32).*(j-1)+1;
Index_o=((V.^3)./32).*j;
%Load in matrix A of Voxel Centerpoint Coordinates (Converts to mm)
A=(size_cube/V).*VoxBuild(V);
A=A(Index_i:Index_o,:); %Indexes for desired Calc. Length

%Focus Point Coordinates of 100mm x 100mm x 100mm Cube (Center of cube)
F=[0,76.2,0];
%Focal Length (mm)
f_lens=105;
%Aperture of Camera (f/stop)
D=4.5;
%Sensor Pixel Dimension
X=1024;
%Square Pixel Length
l_pixel=20e-3; %mm, 20 micrometers
%Load in matrix S of Sensor Centerpoint Coordinates (converts to mm)
S=l_pixel.*SensBuild(X);
%Load in Rotation/Translation/Image Distance for all N camera locations
m=matfile('FinalAttempt_Calibration_Parameters.mat','Writable',true);
M=m.Cal_Parameters(4.*(N-1)+1:4.*N,:);
R=M(1:3,1:3);
T=M(4,1:3)';
Z=M(4,4);

%% -----------------------Weight Ratio Calculation-------------------------
%Parallel Loop
%Number of Processors
numprocessors=32;
%Initialize Parallel Pool of N Processors
parpool(numprocessors);
%Initialize Weight Ratio Array
W=zeros(256,X^2,numprocessors);
parfor i=1:numprocessors
    W(:,:,i)=WeightRatioParallelFun(X,f_lens,l_pixel,D,S,A(256.*(i-
1)+1:256.*i,:),R,T,Z);
end

%Shut down Parallel Pool
delete(gcp('nocreate'))
%Stack all 32 W Matrices into One [8192 x 1024^2] Sparse Matrix
for i=1:numprocessors
    w(256*(i-1)+1:256*i,:)=sparse(W(:,:,i));
end



end
%Voxel World Coordinate Matrix Builder Function (VoxBuild)
```

```
%Created by: Joseph Giroux
%Last Updated:4/24/2020

%Must set in your code V=Voxel Dimension to call function
%(VxVxV Voxel Cube)

function A=VoxBuild(V)

%Iteration Origin
M=[-(V/2),0,-(V/2)];
%All possible x,y,z centerpoint values
for i=1:V
x(i)=[M(1,1)+(i-.5)];
y(i)=[M(1,2)+(i-.5)];
z(i)=[M(1,3)+(i-.5)];
end

%Finds all possible combinations of x,y,z values
%Outputs Matrix A containing all VxVxV centerpoint coordinates
A=combvec(x,y,z)';
end
```

```
%CMOS Sensor Centerpoint Coordinate Builder (SensBuild)
%Created by: Joseph Giroux
%Last Updated:11/12/18

function S=SensBuild(X)
%Iteration Origin
O=[-X/2,-X/2];
%All possible x,y centerpoint values
for i=1:X
x(i)=[O(1,1)+(i-.5)];
y(i)=[O(1,2)+(i-.5)];
end

%Finds all possible combinations of x,y values
%Outputs Matrix S containing all 1024x1024 pixel centerpoint coordinates
S=combvec(x,y)';

end
```

```
%ARC Grid Submission: Parallel Solver Function
%Created by: Joseph Giroux
%Last Updated: 5/6/19

function w=WeightRatioParallelFun(X,f_lens,l_pixel,D,S,A,R,T,Z)
%Initialize Weight Ratio Array
w=zeros(size(A,1),X^2);
for k=1:size(A,1)
%---------------------Image Coordinate Calculations-----------------------
    CamCoord(:,k)=R*A(k,:)'+T;
    x_prime(k)=Z.*(CamCoord(1,k)./CamCoord(3,k));
    y_prime(k)=Z.*(CamCoord(2,k)./CamCoord(3,k));
%-------------------------x_img, y_img, z_img-----------------------------
    z_img(k)=((1/f_lens)-(1./CamCoord(3,k))).^-1;
    y_img(k)=CamCoord(2,k).*(z_img(k)./CamCoord(3,k));
    x_img(k)=CamCoord(1,k).*(z_img(k)./CamCoord(3,k));
%----------------------Blurry Circle Centerpoints-------------------------
    r(k)=(abs(z_img(k)-Z)./(2.*z_img(k))).*D;
    X_c(k)=Z.*(x_img(k)./z_img(k));
    Y_c(k)=Z.*(y_img(k)./z_img(k));
end
clear CamCoord x_prime y_prime z_img y_img x_img
%---------------------Intersection Area Ratio----------------------------
%Area of Square Pixel
A_p=l_pixel^2; %mm^2
%Diameter of Assumed-Circular Pixel
d_p=sqrt((4*A_p)/pi); %mm
%Area of Blurriness
A_b=pi.*r.^2; %mm^2
for u=1:size(A,1)
    for v=1:X^2
%---------Distance between pixel and blurry circle center-----------------
        l=sqrt(((S(v,1)-X_c(u)).^2)+((S(v,2)-Y_c(u)).^2));
%------------------------------------------------------------------------
%Case a: Blurry Circle Dia. > Pixel Size
if r(u)>=(d_p/2)
    if l<=r(u)-(d_p/2)
        w(u,v)=A_p./A_b(u);
    elseif l>=r(u)+(d_p/2)
        w(u,v)=0;
    else
        w(u,v)=((r(u)+(d_p./2)-l)/d_p).*(A_p./A_b(u));
    end
%Case b: Blurry Circle Dia. < Pixel Size
else
    if l<=(d_p/2)-r(u)
        w(u,v)=1;
    elseif l>=r(u)+(d_p/2)
        w(u,v)=0;
    else
        w(u,v)=((r(u)+(d_p./2)-l)/(2.*r(u)));
    end
end
    end
end
end
```

Appendix C: Camera Calibration

```
%Calibration System of Equations Analysis
%Created by: Joseph Giroux
%Last Updated: 3/3/2020

clear all
clc
close all

%%%%%%%%Choose Camera Location%%%%%%%%
N=1;
%%%%%%%%%%%%%%%%%%%%%%%%%%%%%%%%%%%%%%
%Number of Pixels
X=1024;
%Degree Locations
D=15:15:165;
%Square Pixel Size (Length)
l_pixel=20e-3; %mm, 20 micrometers
%Focus Point Coordinates of 100mm x 100mm x 100mm Cube (Center of cube)
F=[0,76.2,0];
x_wf=F(1,1);
y_wf=F(1,2);
z_wf=F(1,3);
%Focal Length of Rayfact Lens (EFL since Intensifier has 1:1 Relay)
f_lens=105; %mm

%Load in Calibration Cylinder TIF Image
for n=1:size(D,2)
Cal_Cylinder{n}=imread([num2str(D(n)),'_Degrees.tif']);
end
%%%%%% Image Tool %%%%%%
% c=1;
% imtool(Cal_Cylinder{c})
% filt=imcomplement(Cal_Cylinder{c});
% filt=imreducehaze(filt);%,'method','approx','ContrastEnhancement','boost');
% filt=imcomplement(filt);
% filt=imreducehaze(filt,'method','approx','ContrastEnhancement','boost');
% filt=imcomplement(filt);
% filt=imreducehaze(filt);%,'method','approx','ContrastEnhancement','boost');
% filt=imcomplement(filt);
% imtool(filt);
%%%%%%%%%%%%%%%%%%%%%%%%

%Input Image Pixel Coordinates for Cylinder Points

%%%%%%%%%%%%%%%%%%%% INPUTS HERE %%%%%%%%%%%%%%%%%%%%
%%%NOTE: Images have been rotated 180 degrees (inverted)
%%%for ease of inputing point locations. The image is
%%%reverted back to upside down later for sign convention accuracy.
%%%inp variable are pixel coordinates gathered from Matlab
%%% image viewer (Image Tool section above)
%Cylinder Points of Choice (Inverted Image)
```

```
%Points_N=xlsread('Calibration Image Points Data.xlsx','Matlab Readout');


load(['Cylinder_Pixel_Save_',num2str(N),'.mat'])
points=Points_N(:,1)';
inp=Points_N(:,2:3);
%%%%%%%%%%%%%%%%%%%%%%%%%%%%%%%%%%%%%%%%%%%%%%%%%%%%%%%%%%%%

%%%%%% Determination if Points are NonCoplanar %%%%%%
%Load Calibration Cylinder Coordinates
load('CalibrationCylinder_Point_Coordinates.mat')
x_w=Cyl_Coord(points,1);
y_w=Cyl_Coord(points,2);
z_w=Cyl_Coord(points,3);

%Matrix Rank Comparison:
for m=1:size(points,2)-1
M_Coplane(:,m)=[x_w(m+1)-x_w(1),y_w(m+1)-y_w(1),z_w(m+1)-z_w(1)];
end

Rank=rank(M_Coplane);
if Rank<=2
    disp("Points are Coplanar")
    return
else
    disp("Points are NonCoplanar")
end
%%%%%%%%%%%%%%%%%%%%%%%%%%%%%%%%%%%%%%%%%%%%%%%%%%%%%%%%%%%%

%Convert Image Pixel Coordinate System to Centerpoint Coordinate System
x_i=(inp(:,1)-(X/2));
y_i=(inp(:,2)-(X/2));
%Coordinates are reverted back to initial sign convention (180 deg. rotation)
x_i=-1.*(x_i);
y_i=-1.*(y_i);

for i=1:size(x_i,1)

%x-coordinate if loop
if x_i(i)>0
    x_prime(i)=x_i(i)-.5;
else
    x_prime(i)=x_i(i)+.5;
end

%y-coordinate if loop
if y_i(i)>0
    y_prime(i)=y_i(i)-.5;
else
    y_prime(i)=y_i(i)+.5;
end

end
%Apply Pixel Size Scaling
x_prime=l_pixel.*x_prime;
```

```
y_prime=l_pixel.*y_prime;


%% Matrix Linear Equation LinSolve Section
for k=1:size(x_prime,2)
syms r1 r2 r3 r4 r5 r6 r7 r8 r9 T_x T_y T_z Z_0 a

vars=[r1 r2 r3 r4 r5 r6 r7 r8 r9 T_x T_y T_z Z_0 a];

B(2.*(k-1)+1:2*k,:)=[x_w(k),y_w(k),z_w(k),1,0,0,0,0,-x_prime(k).*x_w(k),-
x_prime(k).*y_w(k),-x_prime(k).*z_w(k);...
    0,0,0,0,x_w(k),y_w(k),z_w(k),1,-y_prime(k).*x_w(k),-y_prime(k).*y_w(k),-
y_prime(k).*z_w(k)];

y=[(Z_0.*r1)./T_z,(Z_0.*r2)./T_z,(Z_0.*r3)./T_z,(Z_0.*T_x)./T_z,(Z_0.*r4)./T_
z,(Z_0.*r5)./T_z,(Z_0.*r6)./T_z,...
    (Z_0.*T_y)./T_z,r7./T_z,r8./T_z,r9./T_z]';

b(:,2.*(k-1)+1:2*k)=[x_prime(k),y_prime(k)];

end
b=b';

%% Least Squares Solution
Y=(B'*B)\(B'*b);
b_leastsquares=B*((B'*B)\(B'*b));
residuals=b-b_leastsquares;

%% Solve r1-r6,T_x,T_y Section
x0=[.5,.5,.5,.5,.5];
options=optimoptions('fsolve','MaxFunEvals',5000000,'MaxIter',5000000,'TolX',
1e-20,'TolFun',1e-15);  %,'Display','iter-detailed');
sol_1=fsolve(@(x0)fsolve_a(x0,Y),x0,options);
a=sol_1(5);

r1=sol_1(1);
r2=sol_1(2);
r3=Y(3)*a;
r4=sol_1(3);
r5=sol_1(4);
r6=Y(7)*a;
T_x=Y(4)*a;
T_y=Y(8)*a;

%% Solve r7,r8,r9 Section
%Based on Orthonormal, Right-Handed Properties of Rotation Matrix

r7=r2*r6-r3*r5;
r8=r3*r4-r1*r6;
r9=r1*r5-r2*r4;

%% Image Distance Fsolve Section (x_primef,y_primef,z_f,Z_0)

x_f=r1*x_wf+r2*y_wf+r3*z_wf+T_x;
```

```
y_f=r4*x_wf+r5*y_wf+r6*z_wf+T_y;

x0=[1,5,1035,150];
sol_2=fsolve(@(x0)fsolve_Z0(x0,x_f,y_f,f_lens,a,x_wf,y_wf,z_wf,r7,r8,r9),x0,o
ptions);
x_primef=sol_2(1);
y_primef=sol_2(2);
z_f=sol_2(3);
Z_0=sol_2(4);

T_z=a*Z_0;

%% Orthogonality Test
%%%The Rotation Matrix values should obey orthogonality/orthonormality.
%%%This means that the Rotation matrix R follows (R')*R=I where R'
%%%is the transpose of Rotation Matrix R, and I is the Identity Matrix.
%%%In summary, m1,m5,m9 should equal 1 and m2,m3,m4,m6,m7,m8 should equal 0.
m1=(r1^2)+(r4^2)+(r7^2);
m2=(r2*r1)+(r5*r4)+(r8*r7);
m3=(r1*r3)+(r4*r6)+(r7*r9);
m4=(r2*r1)+(r5*r4)+(r8*r7);
m5=(r2^2)+(r5^2)+(r8^2);
m6=(r2*r3)+(r5*r6)+(r8*r9);
m7=(r1*r3)+(r4*r6)+(r7*r9);
m8=(r2*r3)+(r5*r6)+(r8*r9);
m9=(r3^2)+(r6^2)+(r9^2);



%% Save values for later concatenation
% Calibration_Loadout=[r1,r2,r3,0;r4,r5,r6,0;r7,r8,r9,0;T_x,T_y,T_z,Z_0];
% save(['Calibration_Loadout_',num2str(N),''],'Calibration_Loadout')

%% Euler Angle Calculation

x0 = [0,0,30]; %Initial guess values
dataset=[r1,r2,r3;r4,r5,r6;r7,r8,r9];
options = optimoptions('fsolve','algorithm','levenberg-marquardt','TolX',1e-
14,'TolFun',1e-6,'MaxFunEvals',1000);
A=fsolve(@(A)EulerAngleSolve(A,dataset),x0,options);
%Yaw = y-axis rotation (theta)
theta=A(2);
%Pitch = x-axis rotation (psi)
psi=A(3);
%Roll = z-axis rotation (phi)
phi=A(1);
```

```
%Coefficient "a" Fsolve Function
%Created by: Joseph Giroux
%Last Updated: 12/19/19

function F=fsolve_a(x0,Y)

r1=x0(1);
r2=x0(2);
r4=x0(3);
r5=x0(4);
a=x0(5);


F(1)=-Y(1)+(r1./a);
F(2)=-Y(2)+(r2./a);
F(3)=-Y(5)+(r4./a);
F(4)=-Y(6)+(r5./a);
F(5)=-2+sqrt(((r1+r5).^2)+((r2-r4).^2))+sqrt(((r1-r5).^2)+((r2+r4).^2));


End
```

```
%Coefficient "r7,r8,r9" Fsolve Function
%Created by: Joseph Giroux
%Last Updated: 12/19/19

function F=fsolve_r789(x0,r1,r2,r3,r4,r5,r6)

%Based on Orthonormal and Right Handed Properties of Rotation Matrix

%Variables
r7=x0(1);
r8=x0(2);
r9=x0(3);

%Equations
F(1)=-1+(r1.^2)+(r4.^2)+(r7.^2);
F(2)=-1+(r2.^2)+(r5.^2)+(r8.^2);
F(3)=-1+(r3.^2)+(r6.^2)+(r9.^2);


end
```

```
%Coefficient "Z_0" Fsolve Function
%Created by: Joseph Giroux
%Last Updated: 1/29/2020

function F=fsolve_Z0(x0,x_f,y_f,f_lens,a,x_wf,y_wf,z_wf,r7,r8,r9)

x_primef=x0(1);
y_primef=x0(2);
z_f=x0(3);
Z_0=x0(4);



% F(1)=-x_primef+y_primef.*(x_f/y_f);
% F(2)=-y_primef+Z_0.*(y_f/z_f);
% F(3)=-x_primef+Z_0.*(x_f/z_f);
% F(4)=(-1/f_lens)+(1/z_f)+(1/Z_0);

F(1)=-x_primef+y_primef.*(x_f/y_f);
F(2)=-y_primef+Z_0.*(y_f/z_f);
F(3)=(1/f_lens)-(1/z_f)-(1/Z_0);
F(4)=-z_f+r7*x_wf+r8*y_wf+r9*z_wf+a*Z_0;


end
```

```
%Euler Angle fsolve Function
%Created by: Joseph Giroux
%Last Updated: 2/12/2020

%Used in conjunction with Coordinate_Transformation_Solver.m
%to determine euler angles given unit vectors of the axes

function [F] = EulerAngleSolve(x0,V_2)

% V_2 - 3x3 Matrix of axes unit vectors

%Rx-Euler Rotation Matrix about the x-axis
%Ry-Euler Rotation Matrix about the y-axis
%Rz-Euler Rotation Matrix about the z-axis

% R = [cos(psi)*cos(phi)-cos(theta)*sin(psi)*sin(phi),-sin(psi)*cos(phi)-
cos(theta)*sin(phi)*cos(psi), sin(theta)*sin(phi);...
%      cos(psi)*sin(phi)+cos(theta)*cos(phi)*sin(psi),-
sin(phi)*sin(psi)+cos(theta)*cos(phi)*cos(psi),-sin(theta)*cos(phi);...
%      sin(theta)*sin(psi), sin(theta)*cos(psi), cos(theta)];
phi = x0(1);
theta = x0(2);
psi = x0(3);
```

```
Rx = [1 0 0 ; 0 cosd(psi) -sind(psi); 0 sind(psi) cosd(psi)];
Ry = [cosd(theta) 0 sind(theta); 0 1 0; -sind(theta) 0 cosd(theta)];
Rz = [cosd(phi) -sind(phi) 0;sind(phi) cosd(phi) 0; 0 0 1];
R = Rz*Ry*Rx;

%  xaxis = [V_2(1,1);V_2(1,2);V_2(1,3)];
%  yaxis = [V_2(2,1);V_2(2,2);V_2(2,3)];
%  zaxis = [V_2(3,1);V_2(3,2);V_2(3,3)];
%  unitX = [1;0;0];
%  unitY = [0;1;0];
%  unitZ = [0;0;1];
%
%  F(1,:) = R*(xaxis)-unitX;
%  F(2,:) = R*(yaxis)-unitY;
%  F(3,:) = R*(zaxis)-unitZ;

F(1)=R(1,1)-V_2(1,1);
F(2)=R(1,2)-V_2(1,2);
F(3)=R(1,3)-V_2(1,3);
F(4)=R(2,1)-V_2(2,1);
F(5)=R(2,2)-V_2(2,2);
F(6)=R(2,3)-V_2(2,3);
F(7)=R(3,1)-V_2(3,1);
F(8)=R(3,2)-V_2(3,2);
F(9)=R(3,3)-V_2(3,3);

end
```